12-2013

Chemical Vapor Deposition of Heteroepitaxial Boron Phosphide Thin Films

John Daniel Brasfield
University of Tennessee - Knoxville, jbrasfie@utk.edu

To the Graduate Council:

I am submitting herewith a dissertation written by John Daniel Brasfield entitled "Chemical Vapor Deposition of Heteroepitaxial Boron Phosphide Thin Films." I have examined the final electronic copy of this dissertation for form and content and recommend that it be accepted in partial fulfillment of the requirements for the degree of Doctor of Philosophy, with a major in Chemistry.

Charles S. Feigerle, Major Professor

We have read this dissertation and recommend its acceptance:

Laurence Miller, Frank Vogt, Ziling Xue

Accepted for the Council:

Carolyn R. Hodges

Vice Provost and Dean of the Graduate School

(Original signatures are on file with official student records.)

Chemical Vapor Deposition of Heteroepitaxial Boron Phosphide Thin Films

A Dissertation Presented for the

Doctor of Philosophy

Degree

The University of Tennessee, Knoxville

John Daniel Brasfield

December 2013

DEDICATION

To my Family,

Chase, Macie, and Hadley. For support and encouragement throughout this process…

ACKNOWLEDGEMENTS

This dissertation would not have been possible without a number of individuals each contributing in their own unique way. First, I would like to thank Dr. Feigerle for your patience, guidance and tutelage throughout the process. Your calm approach to problem solving has taught me that success takes time and is worth the wait. I would also like to thank Dr. Miller agreeing to serve on my committee. I would like to acknowledge the rest my committee members, Dr. Xue and Dr. Vogt for taking time to be a part of this research. Additional thanks goes to the supportive members of my research group. Thank you, Dr. Julia Abbott for toiling away in the lab and for the invaluable XRD analysis that shaped the project. Thank you to Eric Barrowclough for his work with Autocad and never ending encouragement and Stephen Gibson for his Mass Spectroscopy of weirdness of the process. Thanks to Alexis Dale for her dedication and courage to take on the this project.

I would also like to thank my project collaborators in the Materials Science and Engineering Department for their research support. Many thanks to Dr. Gerd Duscher and Guloinag Li for their spectacular TEM analysis. Without out the wonderful images, progress would not have been possible. Acknowledgements go to Dr. Joo Hyon Noh for fabrication of the heterostructures and Dr. Eric Lukosi for useful consultation.

From Y-12, thanks to Dr. Jonathan Morrell for your support and encouragement to pursue this degree. Many thanks to the rest of the members from the Compatibility and Surveillance section for their kindness and willingness to help when needed. Thanks to the Y-12 PDRD program for financial support of this project.

My family played an integral role in my willingness to pursue a Ph.D. Thanks to my wife Chase for pushing me to work hard and get this done. Without you by my side, this would not have been accomplished. Thanks to my parents Robert and Judy Brasfield for teaching me the value of hard work and fostering a lifetime love of learning, to you both I am forever grateful.

I would like to thank David Beach for his scientific guidance throughout this process. You were always there to answer the tough questions and point me in the right direction. Thanks for the support and believing that I could succeed in novel materials research.

Finally, I would like to thank the DOE office of Nonproliferation Verification and Research for funding my research at Y-12 and the University of Tennessee for the past five years.

ABSTRACT

Boron monophosphide (BP) is a group III-V compound semiconductor with a wide band gap of 2.3 eV. Its unique electrical properties make it a promising material for use as a room temperature thermal neutron detector and thermoelectric device in high temperature and radiation fields. A thin film of BP enriched in the boron- 10 isotope can yield 2.8MeV of energy, which in solid-state BP can yield ~0.5 million electron-hole pairs that would be detectable with minimal amplification in a device. The high carrier concentration, wide band gap, inertness and refractory nature make it an attractive material for use in the extreme environments of nuclear reactors. The main drawback to BP is the difficulty in synthesizing high quality thin films. The majority of the previous work on BP was performed on Si substrates. The high lattice mismatch between Si and BP incorporates strain in the BP film which causes varying defects and charge traps to be introduced, adversely affecting electrical performance. It is the purpose of this work to identify the parameters necessary to deposit highly ordered zincblende boron phosphide (BP) thin films on 4° off-axis C-face 4H-SiC(0001) substrates by chemical vapor deposition.

SiC only has a 4% lattice mismatch from BP, which could greatly reduce the inherent strain from heteroepitaxial growth. Ultra high purity diborane and phosphine are used as reactive precursors, with hydrogen as the carrier gas. Conditions necessary for high quality BP thin films will be explored. SEM, XRD, TEM and Raman spectroscopy are used to characterize the BP films and identify the temperature, phosphine to diborane flow rate ratios, SiC wafer termination and wafer surface preparation to elucidate optimum BP thin films for eventual device fabrication.

TABLE OF CONTENTS

LIST OF TABLES

LIST OF FIGURES

Abbreviations and Symbols

α	Polarizability
α_e	Relaxed lattice constant of epitaxial layer
α_s	Relaxed lattice constant of substrate
AES	Auger Electron Spectroscopy
AlP	Aluminum phosphide
amu	atomic mass unit
BP	Boron phosphide
CCD	Charge coupled device
CM	Capacitance Manometer
CVD	Chemical Vapor Deposition
E	Electromagnetic field magnitude
DSE	Defect Selective Etch
DTV	Damage Threshold Velocity
ΔE_m	Energy of the molecule
ε_o	Percent lattice mismatch
EDS	Energy Dispersive X-Ray Spectroscopy
EELS	Electron Energy Loss Spectroscopy
FCC	Face Centered Cubic
GUI	Graphical User Interface
hv_i	Energy of incident photon
hv_s	Energy of Scattered photon
IR	Infrared
$KMnO_4$	Potassium permanganate

λ	Wavelength
LPCVD	Low Pressure Chemical Vapor Deposition
MFC	Mass Flow Controller
MS	Mass Spectrometer
μ	Dipole moment
n/s	Neutrons per second
O.D.	Outer Diameter
RF	Radio Frequency
SEM	Scanning Electron Microscope(y)
sccm	Standard Cubic Centimeters per Minute
SiC	Silicon Carbide
SIMS	Secondary Ion Mass Spectrometry
SLM	Standard Liters per Minute
TEF	Thermoelectric Motive Force
TEM	Transmission Electron Microscope(y)
TEP	Thermoelectric Power
Θ	Theta
TOF	Time of Flight
VPE	Vapor Phase Epitaxy
X	Magnification
XRD	X-Ray Diffraction
Z	Atomic Number

List of Attachments

CHAPTER I
INTRODUCTION

Semiconductors

Technical curiosity into new materials and new material properties is well established in the history of science, and persists today. More often than not, newly identified material or properties become responsible for fundamental advances in technology. One example of this was the discovery of semiconducting behavior in 1833 by Michael Faraday.[1] By definition, semiconductors are materials with electrical conductivity between insulators and metals.[2] In his experiment, Faraday observed the resistance of silver sulfide changed with temperature. This spurned a more comprehensive investigation by Hittorf in 1851 that quantitatively documented the conductivity of metal sulfides as a function of temperature.[1,3] The next groundbreaking discovery for semiconductor material came in 1878 by way of Edwin Hall. Hall discovered that charge carriers in solids are deflected in magnetic fields. This, together with the similarly timed discovery of the electron, promoted electron conduction theory in solids.[4] In 1914, the modern interpretation of band theory of solids was developed by Alan Wilson and Werner Heisenberg. Wilson theorized that electrons flowed through filled and empty energy bands (Figure 1) and Heisenberg proposed the concept of an electron hole.[3-5] Band theory predominates modern semiconductor research.[2] Identification of band gaps has revolutionized the semiconductor device industry to the point that semiconductors have been broken down in to subcategories of wide gap and narrow gap semiconductors based on specific material characteristics.

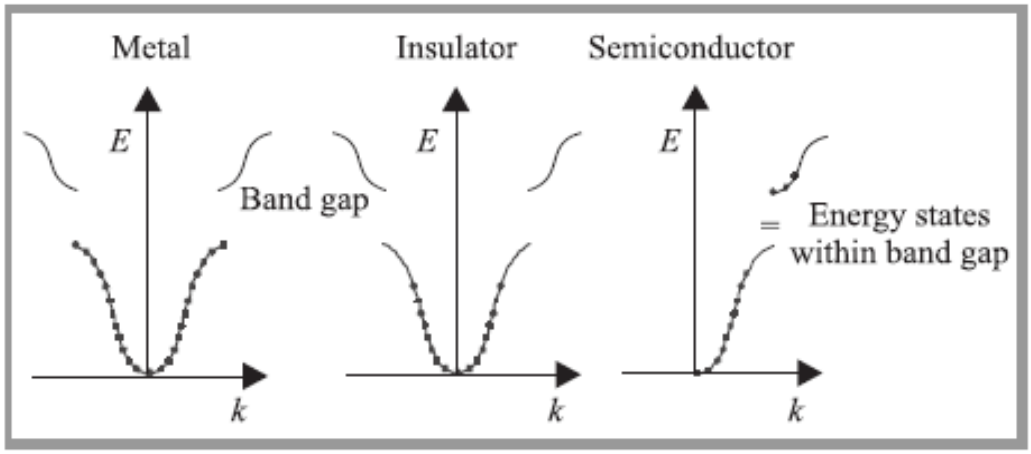

Figure 1. Early Band Theory of Solids[1]

Pure element semiconductors do exist, such as silicon and germanium, but most of the current research is focused on compound semiconductors or bonded elements that exhibit semiconducting properties.[6] The focus of this dissertation is on the subgroup III-V semiconductors. Group III-V semiconductors refer to compounds consisting of a combination of elements from groups III and V of the periodic table. More specifically, the boron group and the pnictogens. Table 1 lists the elements comprising group III-V semiconductors.

Table 1. List of Elements Comprising Group III-V

COMPOUND SEMICONDUCTORS **GROUP III (IUPAC 13)**	**GROUP V (IUPAC 15)**
Boron	Nitrogen
Aluminum	Phosphorus
Gallium	Arsenic
Indium	Antimony
Thallium	Bismuth

These compounds have unique properties that make them attractive for device fabrication and other specific applications. First, these semiconductors tend to have a zincblende structure. This structure, shown below (Figure 2), is a face centered cubic lattice type with space group F3m and

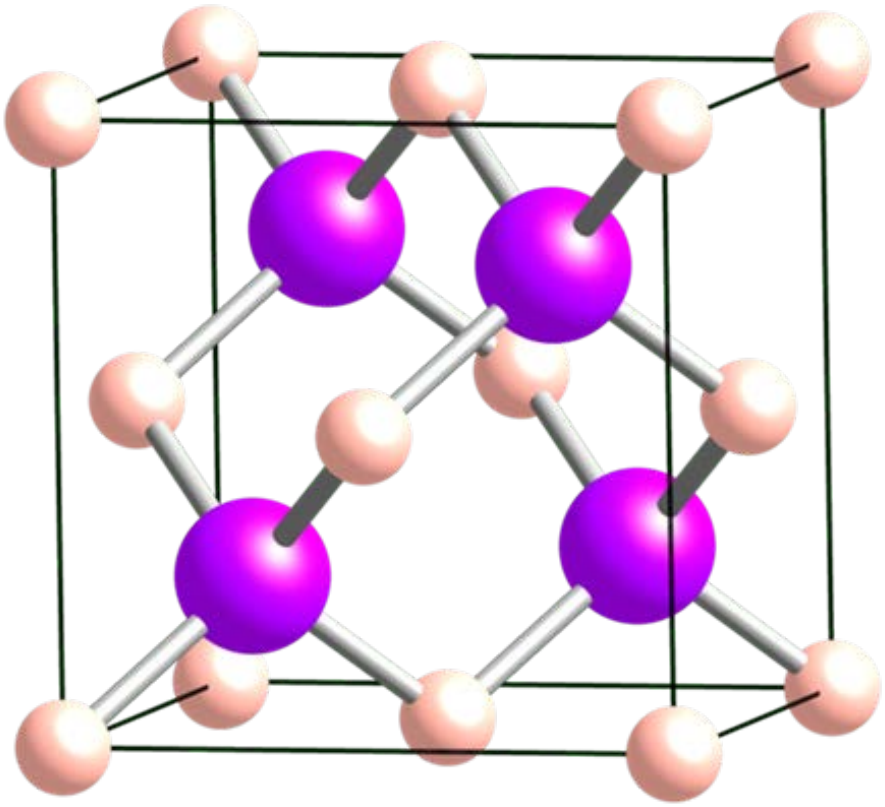

Figure 2. Crystal lattice of zinc sulfide, representing the zincblende crystal structure[69]

tetrahedral coordination of the constituent atoms.[7] The zinc blende structure is very similar to the diamond cubic lattice, but with alternating type of atoms rather than just carbons in the lattice.

In addition to having a cubic structure, group III-V semiconductors exhibit unique bonding characteristics. [6-7] Bonding in these semiconductors is a mix of both partial ionic and covalent[8]. The partial ionic and covalent bonding instills high melting temperatures, but low thermal decomposition temperatures for some III-V's. One of the most important aspects of the group III-V semiconductors is their band gap. The band gap refers to the distance between the top of the valence band of electrons and the lowest level of the conduction band, a feature predicated in the aforementioned Wilson's band theory of solids. Group III-V semiconductors typically have band gaps around 3 eV which allow room temperature operation for most processes of interest in these materials.[9]

Electronically, a group III-V semiconductor may be either a direct or indirect bandgap semiconductor. In direct semiconductors, the top of the valence band and the bottom of the conduction band occur at the same magnitude of momentum. A plot of the energy vs. the momentum shown in Figure 3 depicts the narrow region where an incoming energy, most commonly in the form of a photon can easily promote an electron to the conduction band. Examples of direct III-V semiconductors are indium phosphide and gallium arsenide. [9-11] Conversely, in indirect semiconductors, the top of the valence band and the bottom of the conduction bands are offset and occur at different momenta (Figure. 4).

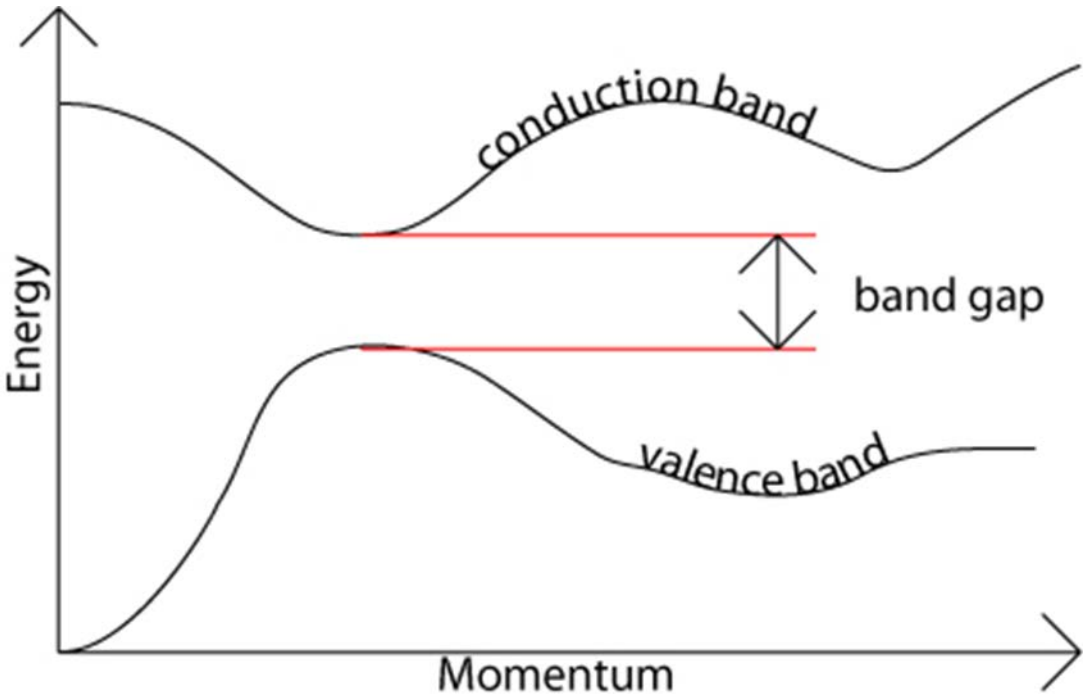

Figure 3. Plot of energy verses momentum showing the coordination of the valence and conduction bands indicative of a direct semiconductor[5]

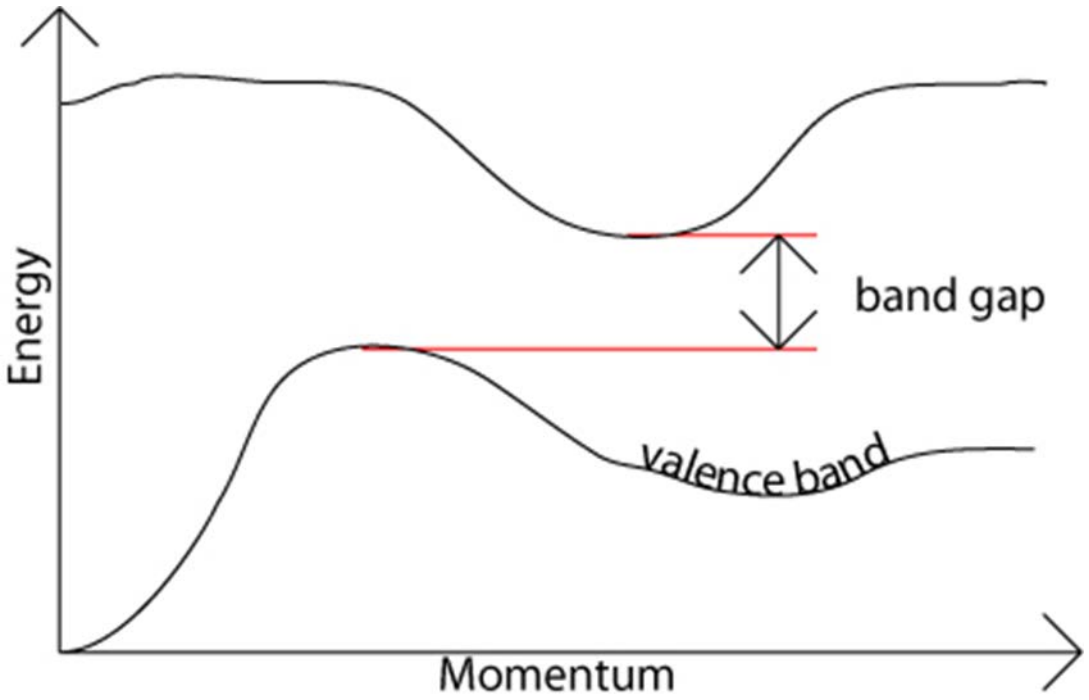

Figure 4. Plot of energy verses momentum showing the disjunction between the valence and conduction bands. Indicative of indirect semiconductors[5]

Operationally, indirect semiconductors are typically slower from the requirement, that in order for an incident photon to promote an electron to the conduction band, an additional momentum to the electron must be imparted. This typically involves electron interacting with inherent phonons.[11] Another interesting electronic property of III-V semiconductors is the mobility of the electron holes. The unique bonding character influences electron mobility in III-V's. It is thought that the partial ionic bonding found in III-V's leads to a more tightly bound lattice. This has an inverse effect on the charge carriers and the net result is a higher mobility in III-V semiconductors.[10]

Aside from their attractive electronic properties, group III-V semiconductors can be readily synthesized.[9] This comes from the tendency for these semiconductors to maintain stoichiometry even under excess reactant conditions.

The evolution of semiconductors has had a profound impact on the development of modern electronic devices. Applications thereof have expanded at a rapid pace and the usefulness of traditional semiconductors such as silicon and germanium in advanced applications like extreme environment applications are waning. The advantages of compound semiconductors such as wide bandgap, high mobility, and direct bandgap are the basis for their application in these special areas. This is why the significance of group III-V semiconductors have begun to greatly contribute to technology advancement. Their peculiar electronic and stoichiometric behavior unlocks possibilities previously not thought possible.

Boron Phosphide

Boron phosphide, a compound between the elements of boron and phosphorous, can exist in two common polymorphs, the cubic monophosphide (BP) shown in Figure 5 and the rhombohdral subphosphide ($B_{12}P_2$)[12] shown in Figure 6. Both forms have been successfully grown and characterized in the literature, but only the monophosphide has been thoroughly researched and demonstrated potential success in eventual device fabrication and will be the primary focus of this dissertation. For simplicity in nomenclature, the term "boron phosphide" will refer to the monophosphide form of BP. As previously stated, the crystal structure of BP is zincblende. X-ray diffraction reported by numerous investigators has confirmed a room temperature lattice constant of 0.45383 nm.[13-15]

Physical Characteristics

The physical appearance of boron phosphide is typically reported to be red-orange in color with the slight presence of brown overtones. This observation is consistent with the band gap of boron phosphide which has been measured and calculated to be in the range of 2.1-2.3 eV.[14 21-22] At these energies, light incident in BP is absorbed at magnitudes above the bandgap. With a medium bandgap of 2.3 eV, BP absorbs violet through green light (wavelengths 400-575 nm), yielding crystals with an appearance at the complementary colors, yellow through red.[16] Physical characteristics for BP include a density of 2.9 g/cc and a molar mass of 41.1588 g/mol. BP has a thermal decomposition temperature at atmospheric pressure of 1100 °C. At pressures approaching 100 GPa it has been reported that BP melts close to the phosphorus temperature of 3000 °C.[17]

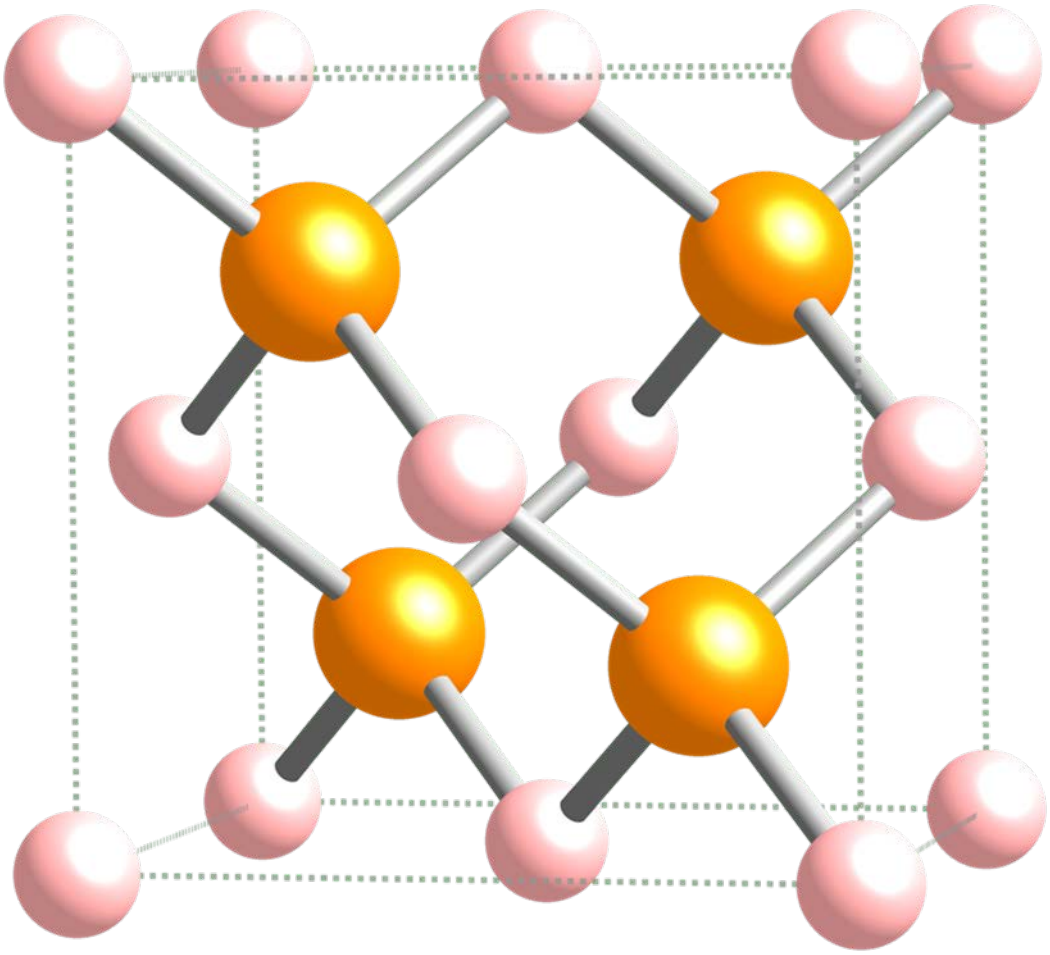

Figure 5. Boron monophosphide[71]

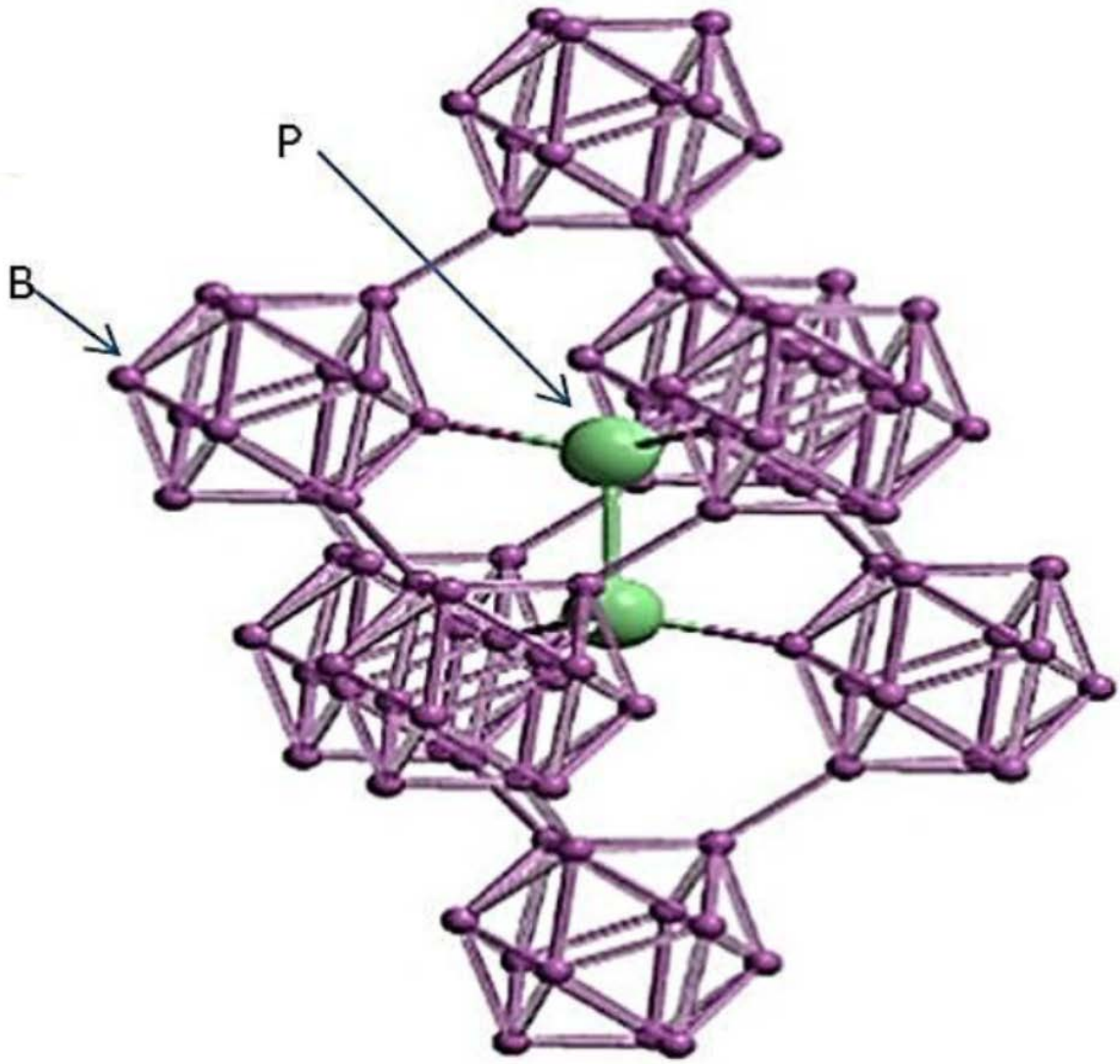

Figure 6. Graphic representation of boron subhosphide $B_{12}P_2$[12]

Chemical Characteristics

The chemical characteristics of boron phosphide have not been extensively investigated.[18] Most of the published literature focuses on the physical and electronic properties rather than the chemical characteristics of the material. It is known that BP by itself is reasonably inert; it does not readily react with most common substances.[19] Bartnitskaya[20] et al. conducted experiments to examine the reactivity of BP with ammonia and nitrogen. No observable reaction was identified at varying temperatures and concentrations. BP is a refractory material and the only known way to etch is to use molten alkali salts at temperatures above 300 °C. The hardness of BP has been noted several times in the literature and a microhardness of 32 GPa has been reported.[21]

Semiconductor Behavior

The semiconducting behavior of boron phosphide is complex; BP can be either a p-type or n-type semiconductor depending on the specific stoichiometric B/P ratios in the material.[23] Boron- rich films tend to be p-type semiconductors and phosphorus- rich BP tends to be n-type semiconductors. Takigawa[24] reported that formation of p-type and n-type BP can be controlled by growth temperature. In chemical vapor deposition experiments, he noted that substrate temperatures of 950-1050 °C resulted in growth of predominately n-type films. At higher substrate temperatures of 1050 °C and above, p-type material was preferred. This study is somewhat inconclusive as the team did not attempt to isolate the effect of flow rate and temperature on semiconductor type. The flow rate of the gaseous precursors used for BP growth, diborane and phosphine was varied in each experiment rather than kept constant. Therefore it is unclear from these experiments whether temperature is the sole controlling parameter for semiconductor type since excess phosphine was used in the n-type material and a lower ratio was used for predominately p-type BP. Shohno reported similar results to Takigawa, but once again

the temperature dependence was not clearly established since the flow rate of phosphine was altered in each of the experiments. BP is considered an indirect semiconductor, as the minimum in the conduction band and the maximum in the valence band occur at different momenta. In addition to the band gap, charge carrier mobility and lifetime are important electrical characteristics for boron phosphide; they limit the performance and types of devices that can be fabricated from this material. For semiconductors, the charge carrier concentration is simply the number of electrons per unit volume.[25] Carrier concentration is typically measured in cm^{-3} and can be measured by a variety of techniques including photoluminescence spectroscopy and Hall Effect measurements. Charge carrier concentrations for BP are on the order of 1018-1021 cm^{-3}. In experiments by Shohno et al., p-type BP had higher charge carrier concentrations at 1019 cm^{-3} than the reported n-type material. In similar thin film evaluations, Kumashiro measured an intrinsic charge carrier concentration of 4.7×10^{18} cm^{-3}, thus supporting Shohno's measurements. Carrier mobility is another important parameter in semiconductors because it allows the prediction of the temporal response of the material to a stimulus.[26] The term carrier mobility is a collective term and refers to both the hole and electron mobility. The mobility is usually given in units of $cm^2/V \cdot s$.

Early Synthesis

Two approaches have been used to produce boron phosphide: crystal synthesis and chemical vapor deposition film growth. Early attempts at BP synthesis were simple mixtures of boron and phosphorous containing compounds and the application of heat. BP was first synthesized by Moissan in 1891.[27] Moissan was reacting boron-halogen compounds with phosphorous. Boron phosphide was identified as the product of the reaction and a brief description of the physical properties, including red-brown color was noted. Following the work of Moissan, Besson[28] published a similar paper on BP the same year as Moissan. The work was similar in nature and

also included reacting boron and phosphorus containing compounds in the presence of heat. The seminal difference between Moissan's and Besson's work was Besson used the hydride of phosphorous, phosphine, in the reaction with boron triiodide whereas Moissan used phosphorous directly. Following the 1891 experiments, no other work was published on the topic until 1957. A paper by Popper and Ingels[29] in the journal Nature, outlined the first alternative synthesis of BP. Details of the experiment were few, but included the reaction of boron with red phosphorous in a sealed quartz tube at 1100 °C. The resultant powder was characterized by X-ray diffraction methods and the cubic zincblende crystal unit cell was observed. The room temperature lattice constant was determined to be 4.55 Å. Popper and Ingels were also the first to note the hardness of BP and likened this hardness to diamond and the newly identified borazon^{tm} or cubic boron nitride.

Modern Synthesis

The dawn of modern synthesis efforts of BP began in 1964 with the first report of boron monophosphide.[30] The term modern synthesis is used here to delineate a change in the approach of boron phosphide synthesis methodologies from simple elemental mixes to advanced methods that include compound chemical precursors and new heating strategies. This seminal approach influences much of the current BP work. In the mid 1970's the interest in BP shifted from understanding the fundamental properties to applications of the material. Much of the scientific focus of the time was to identify novel materials for advanced device fabrication. Efforts were placed into reviving and improving the quality of early materials synthesis in order to identify useful properties. Advances in the understanding of boron phosphide began to emerge after the advent of chemical vapor deposition technology in the early 1960's.

Vickery[31] was the first to publish an alternative to elemental synthesis of boron phosphide and the formation of a BP thin film. His 1959 article in Nature describes reacting the chlorides of boron and phosphorus mixed in specific ratios to produce a white product which when heated in a tube to 300 °C yielded films of BP. Vickery noted that the dark film floated on water when rinsed freely from the tube. Testing of the resultant film showed chemical stability in ambient air to 1000 °C.

The next year, two works on BP were published by Williams and Ruehrwein and Stone and Hill, both coming from Monsanto Chemical Company laboratories. In both works, halogens of boron and phosphorus were employed as well as reactions from the elements. The goal was to compare the halogen reaction pathway to simple elemental synthesis. Williams and Ruehrwein also explored the use of AlP as a source of phosphorus in the reaction. Table 2 lists the reactions and the results of Williams's experiments.

Table 2. Reactions of BP from Williams and Ruehrwein

Sequence	Reaction	Result of Experiment
1	$4B + P_4 \rightarrow 4BP$ (1000 °C)	Slow
2	$AlP + BCl_3 \rightarrow BP + AlCl_3$ (1000 °C)	Contaminated
3	$BCl_3 + PH_3 \rightarrow BP + 3HCl$ (1000 °C)	Usually shiny black and sometimes translucent red films

All of the reactions were conducted at temperatures of 1000 °C. Reaction 1 was noted to be slow, taking days to complete. Reaction 2 showed percent level contamination of Al_2O_3, a common product of AlP synthesis. Reaction 3 was the most successful, resulting in shiny red films in several attempts which showed a cubic structure in XRD. Williams was also the first to note the formation of the boron subphosphide obtained by heating BP in air at 1000 °C.

Stone and Hill conducted a parallel, but albeit more comprehensive study on the electrical properties of BP. BP was prepared by two methods: vapor phase reactions and slow cooling of a melt of boron and phosphorous. XRD analysis confirmed crystals formed from these processes as cubic BP. Hall Effect measurements were performed on p-type samples produced from the melt by fashioning electrical contacts from silver paint, tungsten and platinum points. This yielded carrier concentrations of 1 to 5 x 10^{18} carriers/cc. N-type material was also observed. Special attention was given to address the energy gap reported by Williams of nearly 6 eV. Williams used optical transmission techniques to measure the energy gap of BP, which with a nearly 6 eV bandgap, should be colorless; however, Stone and Hill, noted that the due to the reddish brown color of their BP samples, the forbidden energy gap was a much more accurate 2.0 eV.

One decade later, a significant development in BP synthesis was reported by Chu et al. who outlined the synthesis and characterization of crystals and epitaxial layers. Fundamentally, these papers were similar in scope to previously discussed work, but with one major difference. Chu reported the first use of hydride precursors for BP epitaxial layers. Chu noted that developments in chemical vapor deposition have made alternate syntheses attractive; furthermore, CVD offers lower reaction temperatures and composition of the reactant mixture is more adjustable. In his experiments, SiC platelets were chosen for BP deposition because of chemical inertness, crystal symmetry and lattice parameters akin to BP. A hydride system was used that included thermal

decomposition of diborane and phosphine in a hydrogen atmosphere and thermal reduction of a boron tribromide-phosphorous trichloride mixture. Temperatures were lower for the hydride system at 850 °C where as temperatures for the halogen system were 1050-1150 °C. Wafers were prepped using a molten sodium hydroxide sodium peroxide that acted to smooth the Si side of the platelet. Heating was achieved by induction of a BP coated graphite susceptor. Reaction parameters of both the hydride and halogen systems varied over a wide range and the resultant BP was studied. Active cooling was applied to the apparatus to minimize gas phase nucleation. Even with cooling, the hydride reactions were limited to below 900 °C because of gas phase nucleation, whereas the halogen reactions, which are more thermally stable, were varied from 850 to 1150 °C.

For the next decade, investigations into BP continued with moderate intensity. Researchers such as Takigawa[32] and Nishinaga[33] reported results and synthesis methodologies similar to those previously discussed. In addition to the CVD methods, several solution growth methods are reported, but with little follow up research. However, in 1983 workers at Sandia National Lab reported a method for growing BP freestanding films on metal substrates. This is the only known reference to growing BP on refractory metals.

In 1984, Yokinobu Kumashiro[34-56] authored the first of over 24 publications on boron phosphide studying all aspects of the materials including synthesis, electrical characterization, thermoelectric power, applications of, and radiation effects. The majority of Kumashiro's work is focused on the electrical properties of BP for development as an alternative semiconductor for Si in extreme environments. Although alternative methodologies are described for synthesis including high pressure flux and other solution growth approaches, the majority of his work uses the hydride precursors first used by Chu.

All of Kumashiro's CVD work with BP was performed on Si and sapphire substrates. Kumashiro acknowledged that the large lattice mismatch between BP and Si was a potential drawback, but ultimately elected to pursue BP grown on Si based on the advantage of being able to etch the Si from the BP. Kumashiro continues to work on BP growth, properties and applications, with his last work on BP published in 2011.[57]

Applications of Boron Phosphide

Despite the considerable amount of research that has been conducted on boron phosphide, commercial applications of this material remain elusive. To date, there have been three primary applications that have been proposed for development of boron phosphide: in neutron detection, as protective coatings for IR optics, and for thermoelectric devices.

Neutron Detectors

The radiation detection community has shown considerable interest in boron phosphide for quite some time. Kumashiro et al. worked on BP in the late 1980's to investigate its usefulness for neutron detection and Los Alamos National Laboratory[58] conducted a project about 15 years later to investigate BP for thermal neutron detection. The interest in BP comes from the fact that few elements on the periodic table have large probabilities of neutron absorption. The probability of neutron absorption is the fraction of the reacting nuclei consumed by the reaction per unit time per unit flux. [59] Neutron cross sections can be determined by considering a high energy particle beam, typically generated by a linear accelerator, impinging on a prepared thin neutron rich target. The generated neutrons are then used to bombard the material of interest. The neutron cross section can be determined by the time of flight method (TOF) for neutron cross section determination. Here, the known neutron flux given in neutrons per seconds (n/s) is compared to

the detected fluxes at the sample and after a specified travel distance in the flight tube (Figure 7). The resultant cross sections are given in terms of cm^2 and range from a maxima at 10^{-18} cm^2 to a minimum detectable quantity of 10^{-28} cm^2. It is convenient to express cross sections in units of barns, where a barn (b) is defined as 10^{-24} cm^2. [59]

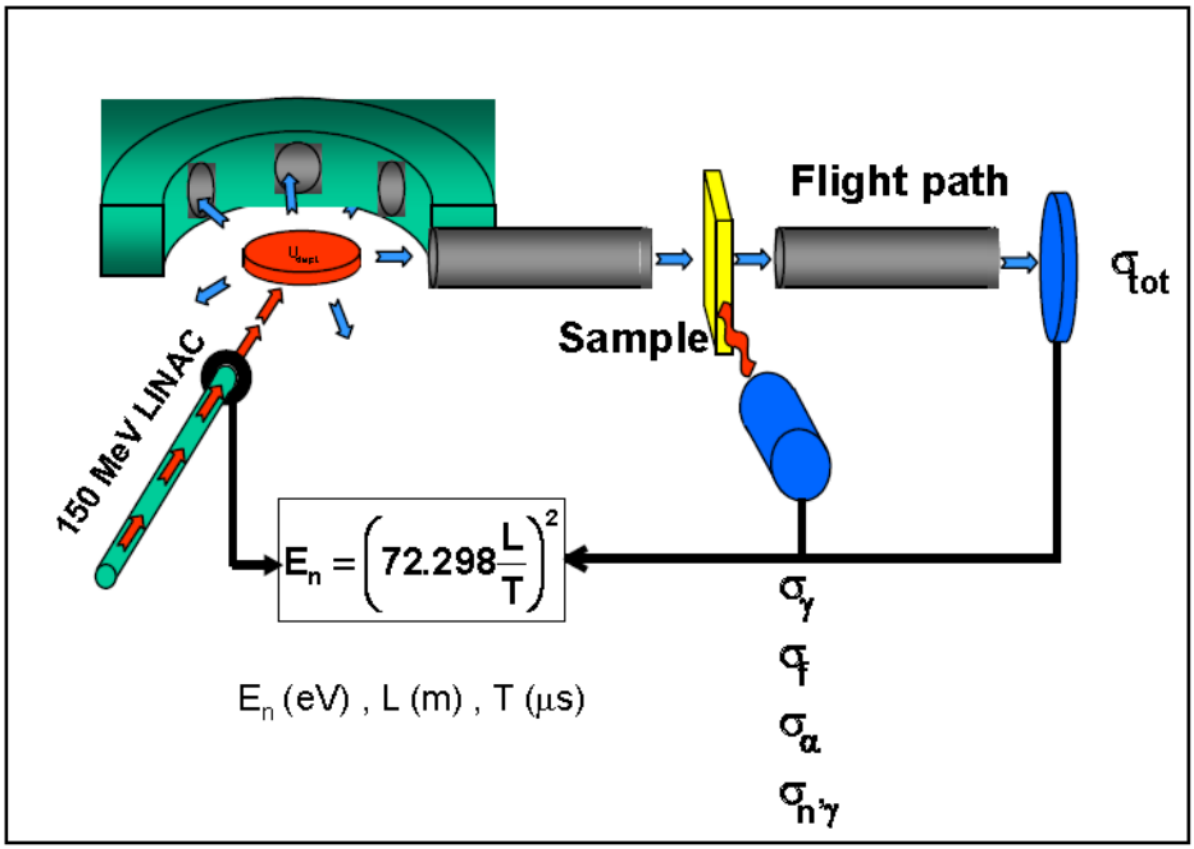

Figure 7. Image of a linear accelerator used for neutron cross section measurements

The importance of neutron cross section becomes apparent when a cursory evaluation of the elements with respect to neutron cross section is performed. Only a select few elements are amenable for neutron absorption. Furthermore, of the elements such as boron, lithium, gadolinium, and helium, that can support neutron absorption, it is the natural abundance of specific isotopes from the aforementioned elements that are the source for large neutron cross sections. Although not to be considered an all-inclusive list, Table 3 provides a number of the common isotopes, cross sections and associated Q values used in neutron detection devices. Associated natural abundances are given for reference purposes to indicate the applicable availability of each isotope. The more rare the isotope, the more resources must be used in order to separate the desired isotope. The Q values refer to the energy liberated following neutron capture.

Table 3. List of common isotopes and cross sections employed in neutron detection with associated natural abundances and Q values

Isotope	**Natural Abundance (%)**	**Neutron Cross Section (Barns)**	**Q Value (MeV)**
Boron 10	19.9	3.8×10^{3}	2.79, 2.31
Lithium 6	7.59	9.4×10^{4}	4.78
Gadolinium 157	15.65	2.5×10^{5}	7.92
Helium 3	1.4×10^{-4}	5.3×10^{3}	0.764

At 19% abundance with a cross section of nearly 4000 barns ^{10}B is at the forefront of neutron choices for cost effective neutron detection devices. A BP based device would operate on the following reactions:

$$^{10}B + n \rightarrow {}^{7}Li^{*} + {}^{4}He + 2.3\ MeV \quad (94\%)$$

$$^{7}Li + \gamma(0.48\ MeV)$$

$$^{10}B + n \rightarrow {}^{7}Li + {}^{4}He + 2.8\ MeV \quad (6\%)$$

The result of the reactions of a thermal neutron with a ^{10}B enriched nucleus is a ^{7}Li nucleus and 2.8 MeV of energy and an excited ^{7} Li nucleus and 2.3 MeV of energy. The resultant energy is paramount in this process, as it would be used to create electron hole pairs in the boron phosphide. The energy needed to form an electron hole pair is approximately three times the band gap. A BP detector would create 10^5 electrons hole pairs per incident neutron.[58] These events can be detected as current pulses by applying a bias voltage to the BP. A semiconductor detector would offer advantages over current neutron detectors, such as higher efficiency, room temperature operation and lower amplification. To date, utilization of boron phosphide as a neutron detector has not materialized due to specific challenges regarding overall BP quality and electrical properties that must be overcome in order to achieve success in neutron detection.

IR Coatings

The use of boron phosphide is not constrained to the field of nuclear detection. Recent experiments conducted by the British military identify boron phosphide as a potential coating material for infrared optics. Materials such as ZnS and Ge transmit in the 8-12 μm wavelength band. These materials are subject to severe corrosion from moisture and particles encountered in flight and naval applications. Boron phosphide can be used to address these problems due to its minimal absorption in the band of interest, high hardness and extreme abrasion resistance.

Experiments were conducted by Gibson[60] et al. and that demonstrated BP coatings on ZnS and Ge optics greatly reduced or completely eliminated the effects of moisture corrosion and particle erosion. Tests of BP films with a 0.8mm water jets at velocities from 150- 400m/s to simulate water droplets encountered in flight showed high resistance to damage in normalized tests of the damage threshold velocity (DTV). The DTV is the maximum velocity a water droplet can impact a given material without causing noticeable damage. Similar experiments of DTV were carried out on BP films with sand jets to measure particle erosion resistance. Again results were exceedingly positive. The conclusion of the set of experiments was similar to the conclusion in the neutron detector application ; that although BP provides significant advantages to existing technology for delicate optical coatings, current process difficulties make it a less attractive option than other less advantageous materials.

Thermoelectric Devices

In addition to identified applications of neutron detecting devices and coverings for delicate IR optics, BP has one more well documented potential application; placing electronic devices in extreme environments. The quest for energy and the increased reliance on electronic devices has created a need to quantify nearly all measurable characteristics processes. One of the most pertinent examples of this is measuring temperature or radiation inside of an operating reactor. Modern demands for reactor safety necessitate the need for sensors and measuring devices inside the reactor core to feed data to operators in real time. The problem is that few materials are applicable to this problem. Traditional electronic devices operating in nuclear reactors fail prematurely from high temperatures or very high ionizing radiation fields. Si based devices suffer from nonlinearity in high dose environments and can lead to abnormal readings if active compensation is not employed.[61]

New materials are constantly being synthesized and evaluated to eliminate these problems. Boron phosphide has shown promise as a thermoelectric device for several reasons. Like in neutron detectors, the wide band gap of BP at > 2.0 eV is positive for operation at high temperature as fewer electrons will be thermally promoted to the conduction band at high temperatures. Secondly, BP is stable at temperatures to 1200 K. Finally, BP is regarded to be chemically inert, thus eliminating the possibility of undesirable reactions taking place at high temperature. BP is naturally resistant to gamma and X-ray fields due to its low mass. As electromagnetic interaction probability scales with Z, BP is expected be transparent in fields approaching 1 R/hr.[17]

Thus far, the thermoelectric attributes of BP have been purely intrinsic; however, the fabrication of BP can induce attractive properties for thermoelectric properties. Consider the hydride decomposition process of synthesizing BP. This will be addressed in detail later. In this process hydride precursors are thermally decomposed in a hydrogen atmosphere. From previous treatment, the resultant BP films can be either p-type or n-type semiconductors depending on the excess of boron or phosphorus in the films. Yugo[62] and Kumashiro published numerous works on the thermoelectric properties of BP crystals and films. In particular, Kumashiro's study of the high temperature electric properties of boron phosphide and the thermoelectric properties of BP as a function of synthesis type span two decades. BP grown via low-pressure chemical vapor deposition (LPCVD) was directly compared to BP grown via photo-assisted thermal CVD methods. The results are shown in Figure 8. It is clear from the graph that BP grown with different methodologies show stark similarities in charge carrier concentration and mobility. For LPCVD grown materials, at the initial temperature of 700 °C, the carrier concentration from both LPCVD and photo assisted materials is in the 10^{15} cm^{-3} range. Increasing the temperature to a maximum of 950 °C shows a decrease in the number of charge carriers to the 10^{13} cm^{-3} range. This is expected behavior, for band theory predicts that as the temperature increases, the number

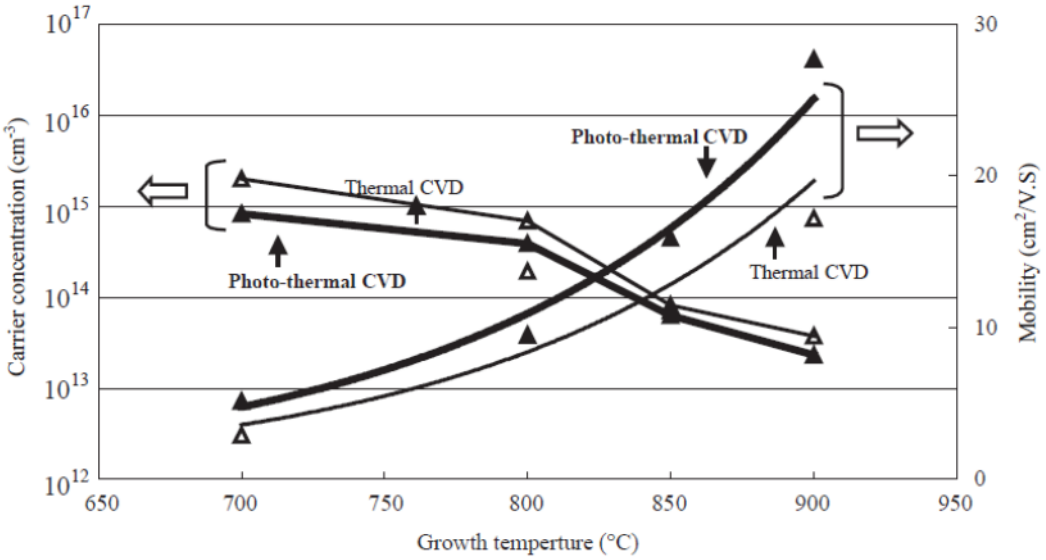

Figure 8. Direct comparison of electric properties as a function of temperature of BP samples.

of electrons in the valence band which are available to carry charge decrease as more and more are prompted to the conduction band. The opposite is true for mobility and BP is no exception. Initial measurements at 700 °C show a minimum at a couple of $cm^2/V•s$ with an exponential increase to a maximum of 30 $cm^2/V•s$ at 900 °C.

Yugo took a slightly different approach to his thermoelectric experiment. Rather than comparing method verses temperature, Yugo chose to analyze p-type or n-type BP as a function of temperature. The thermal decomposition of hydride precursor was once again used to make both p-type and n-type materials. To do this, Yugo varied the flow rates of the boron and phosphorous precursors in addition to elevating or lowering the temperature to elucidate p-type or n-type characteristics. A head to head comparison of the samples shows remarkable differences in thermoelectric behavior. A graph of thermoelectric power verses temperature for n-type BP can be seen in Figure 9. The thermoelectric power (TEP) was determined by measuring the thermoelectric motive force (TEF) in voltage as a function of increasing temperature read by strategic placement of thermocouples. N-type BP shows a steady increase in TEP to 600 °C then saturation tracked to 1200 K. In contrast, p-type BP shows a maximum at room temperature and sharp decline at 500 K to a minimum in TEP of 150 μV/K.

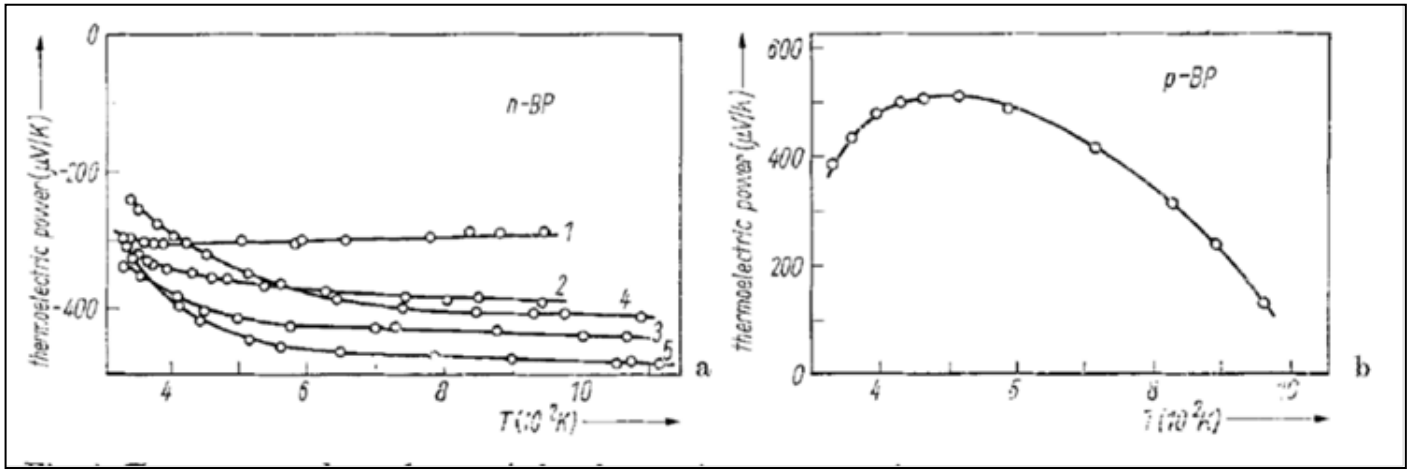

Figure 9. Thermoelectric comparison of p-type and n-type BP

The body of work encompassing boron phosphide varies widely. From early synthesis attempts t included a simple mixing of the elements to more modern synthesis using high purity precursors majority of the science of boron phosphide has yet to be discovered. The fundamental pieces of the puzzle are present: cubic structure, chemical inertness and wide band gap. The unique ability to be both p-type and n-type semiconductors without external dopants creates the possibility of a vast array of options for applications. To date, only three viable applications exist. And only one of this has shown overwhelming success. The science of BP needs to catch up with the material in order for the potential to be realized.

Substrate Selection

One of the most important aspects of semiconductor deposition and growth is the reduction or elimination of growth induced defects. Defects are inherent to all materials and each specific material has its own unique set of characteristic defects. For clarity, it is important to note, that it is impossible to grow a material in an epitaxial arrangement devoid of defects.[63] There are two common types of vapor phase epitaxy (VPE): homo and hetero. Homoepitaxy is the growth of identical polytypes materials on top of each other. An example would be the growth of 3C SiC on a 3C SiC substrate. The more common type of VPE, heteroepitaxy, refers to growing one material on top of another differing material, or growth of a different polytype on the same material. An example of this would be gallium arsenide (GaAs) deposited on Si or 3C SiC growth on 4H SiC.

Due to the lack of suitable BP substrates, heteroepitaxy is the only suitable method to grow BP from the vapor phase. One of the primary problems caused from heteroepitaxial growth is induced strain[64] from crystal lattice mismatch. The resulting strain relief processes often induce

defects in the grown materials which can lead to deleterious device performance. Heteroepitaxial induced strain evolves in the grown films from two origins.[65] The first, lattice mismatch has already been briefly discussed. An additional source of strain comes from differences in thermal expansion coefficients of the two materials. For most materials, strain resulting from differences in thermal expansion is secondary from those derived from lattice mismatch.[63] It is helpful in evaluations of strain to quantify percent lattice mismatch. This can be achieved by considering the unrestrained room temperature lattice constants of the two materials according to the equation:

$$\varepsilon_o = \frac{a_e - a_s}{a_s}$$

The sign of ε_o defines whether the strain is compressive (ae > as) or tensile (ae < as). The above equation is meant as a guide to understanding the formidable technical challenges associated with heteroepitaxial deposition. There is not a set limit on the limitations of percent lattice mismatch and there can be epitaxial growth on material that exceeds 14%. Epitaxy is a complex process affecting specific material characteristics as well as process parameters. Other factors that must be considered along with lattice mismatch in heteroepitaxial deposition include chemical compatibility, electrical characteristics if a device is being fabricated and coefficient of thermal expansion.

Silicon

BP has been grown on a few substrates with the most predominate being Si. Kumashiro conducted depositions primarily on Si substrates, believing that chemical compatibility surpassed lattice mismatch in growth of BP.[17] Silicon is element 14 on the periodic table with a mass of 28.09 grams/mol, density of 2.32 g/cc. and melting temperature of 1414 °C. Si forms a cubic

diamond lattice shown in Figure 10, is tetravalent in the ground state and is an intrinsic semiconductor with a band gap of 1.12 eV. The room temperature lattice constant of Si is 5.43 Å. Comparison of the lattice constants between BP and Si is considered using the equation shown above. Given the lattice constant of BP as 4.54 Å, the computed percent lattice mismatch between Si and BP is -16.4% with the negative sign indicating tensile strain. Using the lattice mismatch minimization approach to heteroepitaxy, Si very quickly becomes a less than ideal candidate for BP deposition. A more closely matched crystal lattice to BP is required. One material that satisfies this requirement is silicon carbide.

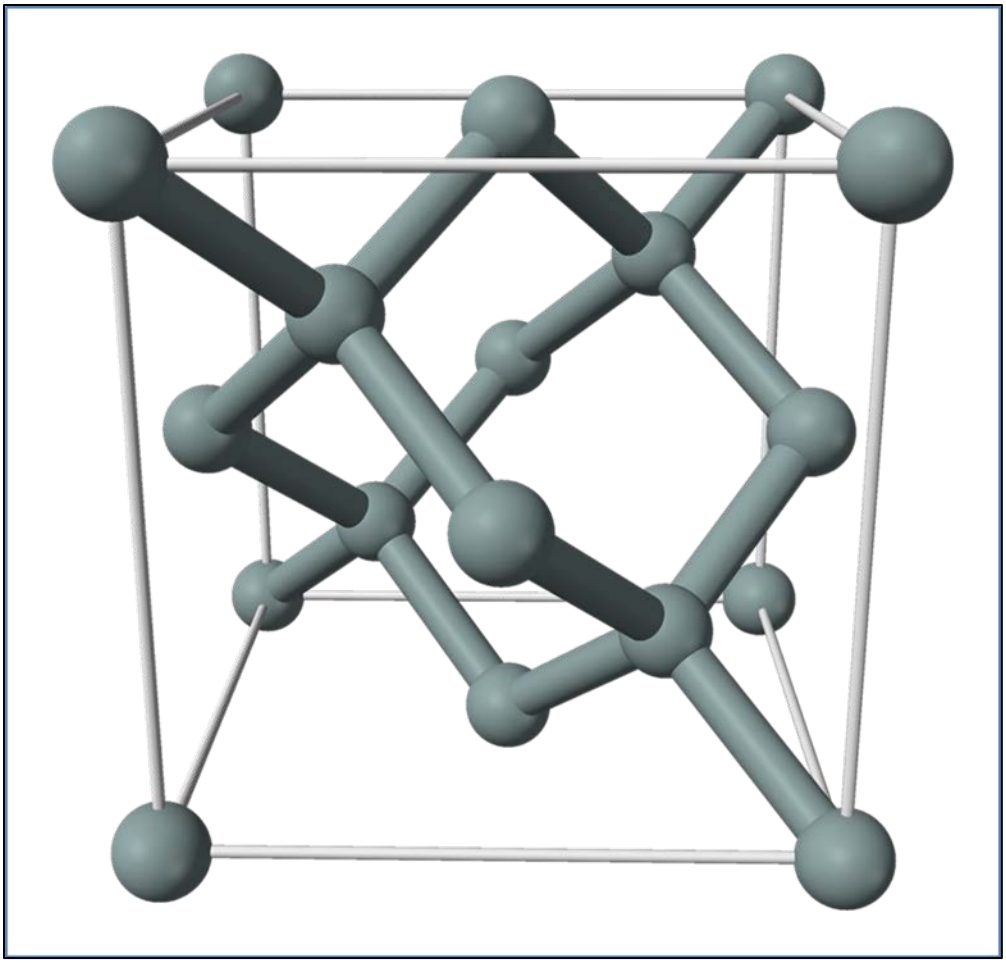

Figure 10. Silicon crystal structure

.

Silicon Carbide

Silicon carbide is a binary refractory semiconductor comprised of silicon and carbon. SiC has a density of 3.21 g/cc, a molar mass of 40.11 g/mol and a melting point of 2,730 C. SiC is one of the hardest compounds second only to diamond with a hardness of 9.5 on the Mohs scale. The crystalline structure of SiC is complex as it forms numerous polytypes. The most predominate crystal representations of SiC are the cubic SiC often called β –SiC and hexagonal SiC commonly referred to as α-SiC in classical notation. Figures 11-13 depict common SiC polytypes . The problem with this classical notation, is that it does not distinguish between the hexagonal polytypes of SiC. In order to do this, another convention must be used. The Ramsdell notation is a system developed to accurately describe the polytypes of SiC. It consists of a number followed by a letter (3C). The number refers to the number of atomic planes stacked before a repeat is formed and the letter designates the crystal structure. Therefore, the 3C example would be three repeating layers and cubic structure. Although there are approximately 250 known polytypes of SiC only a few are common. The most common for research and industrial applications are 4H and 6H with 3C relegated to research settings. Other polytypes include 2H, 8H, 9R (rhombohederal), 10H, 14H, 15R, 19R, 20H, 21H and 24R.

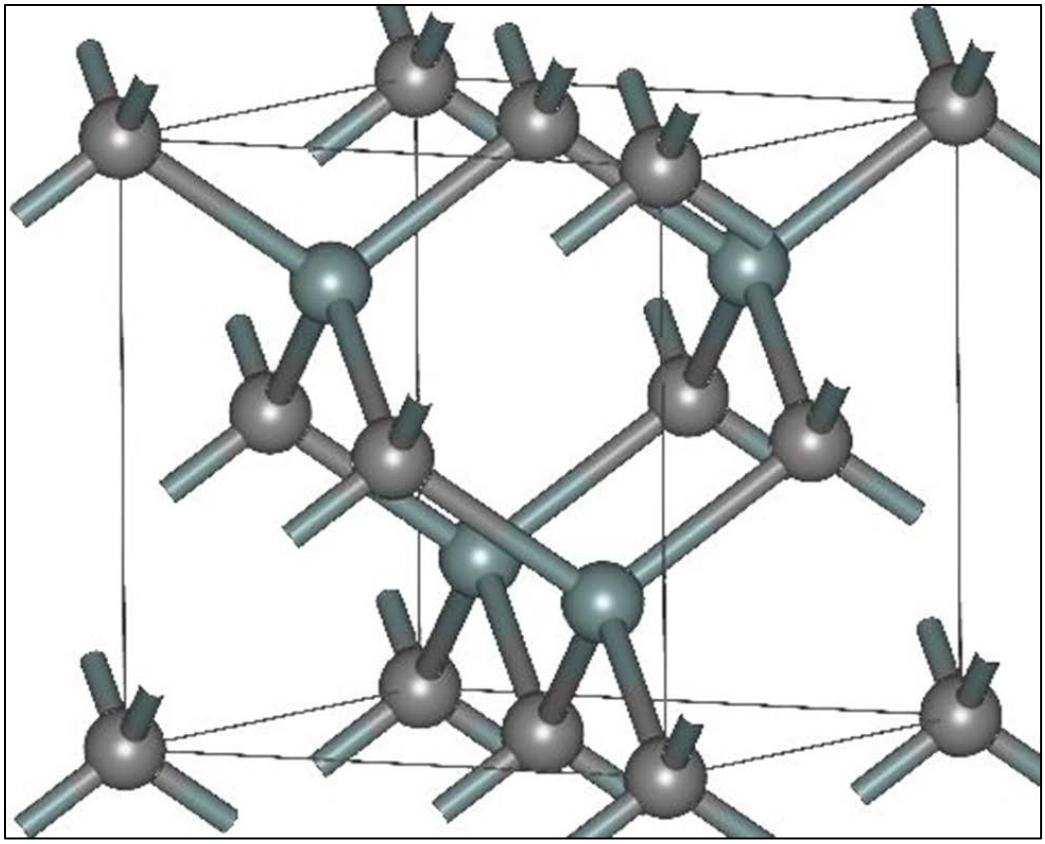

Figure 11. Crystal structure of 3C (β) SiC[73]

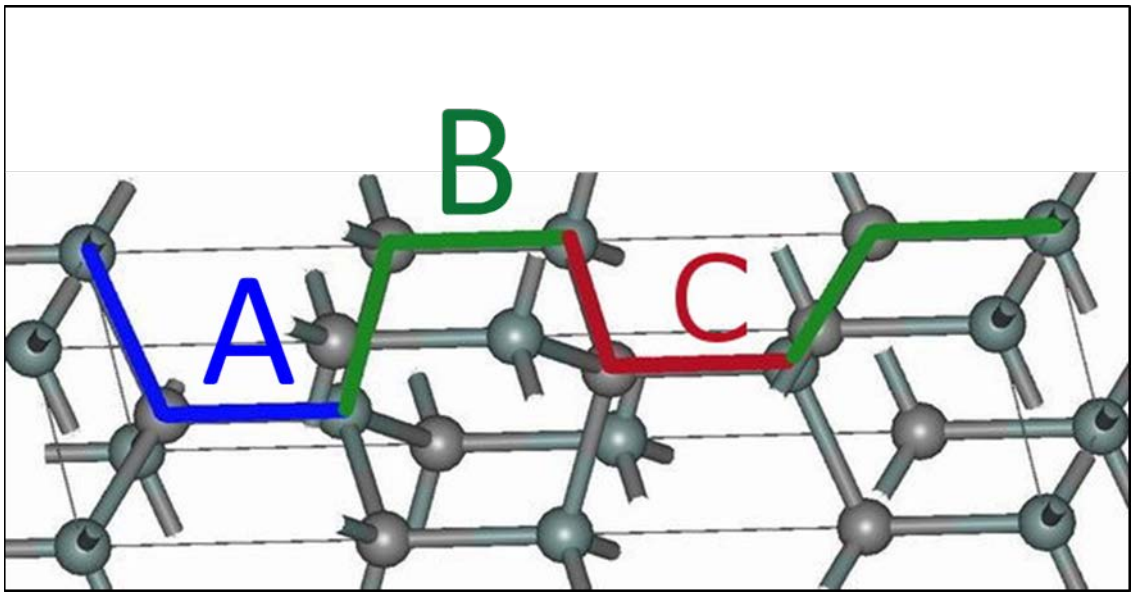

Figure 12. Structure of 4H SiC with stacking sequence

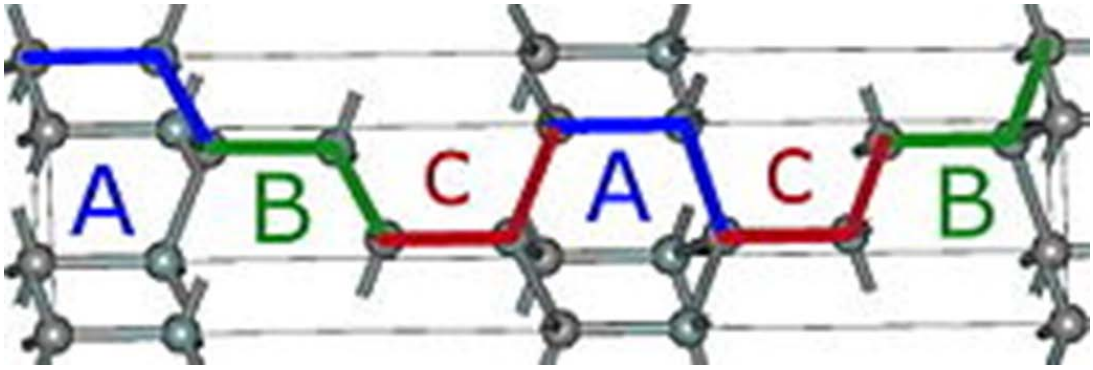

Figure 13. Structure of 6H SiC showing stacking sequence

Crystallographic orientations play an important role in defining the success of high quality growth. Consider the hexagonal systems of SiC shown in Figure 14. The three most commonly referenced planes and directions are shown for reference. The hexagonal system is comprised of four primary axes designated a1, a2, a3 and a perpendicular axis called c. The a axes are exactly 120° apart. The (0001) plane or commonly called the basal plane of the SiC system is the focus of this discussion. The (1100) plane and direction as well as the (1120) and direction are shown for informational purposes only.

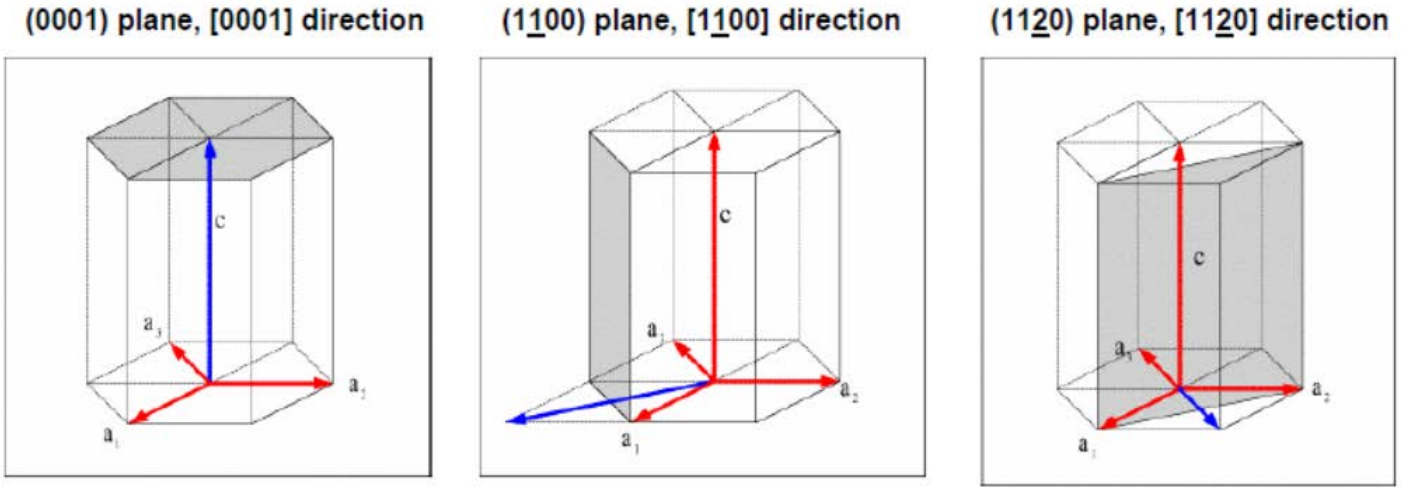

Figure 14. Hexagonal crystal structure of SiC. Showing the most commonly referenced planes and directions[73]

The room temperature lattice consent for 3C SiC is 4.3596 Å. Using the equation for percent lattice mismatch previously presented, the percent lattice mismatch between zincblende BP and cubic 3C SiC is therefore 4.1%. Despite having a cubic polytype, and seemingly a good match for BP deposition, 3C SiC is difficult to obtain in quality suitable for device fabrication. Most often, the 3C SiC that is available is grown heteroepitaxially on other SiC polytypes, and on Si substrates. Lattice mismatch minimization is not limited to identical crystal lattice types. For some systems, it is possible to create alignment with a small lattice mismatch between hexagonal and cubic systems. One example of this is distance between the atoms of hexagonal SiC (4H or 6H) and 3C SiC. Using the unit cell length of 3C SiC of 4.3596 Å, multiplied by $\frac{\sqrt{2}}{2}$ to gives a distance of 3.0827 Å. Comparing this with the A lattice constant of 4H SiC of 3.073 Å, which is the atom separation in the basal plane, gives a percent lattice mismatch between 3C and 4H SiC based on equation 1 as 0.315%. Indeed, 3C SiC can be grown by CVD methods on the basal plane of 4H or 6H SiC surfaces. The basal plane of SiC similarly corresponds well with the (111) direction of BP. This is shown in Figure 15. Applying the same logic and using the same equation yields the percent lattice mismatch between 4H SiC and BP as 3.4%. Figure 16 shows the (111) direction in a cubic system for clarification.

Wafers

Si and SiC wafers, obtained from commercial suppliers, were used as substrates in this project. Silicon substrates, which are relatively cheap and easily cleaved, were used initially to test the CVD system and establish process parameters for BP growth. Si and SiC wafers are commonly employed in the semiconductor industry and are available in a variety of orientations, doping and quality.

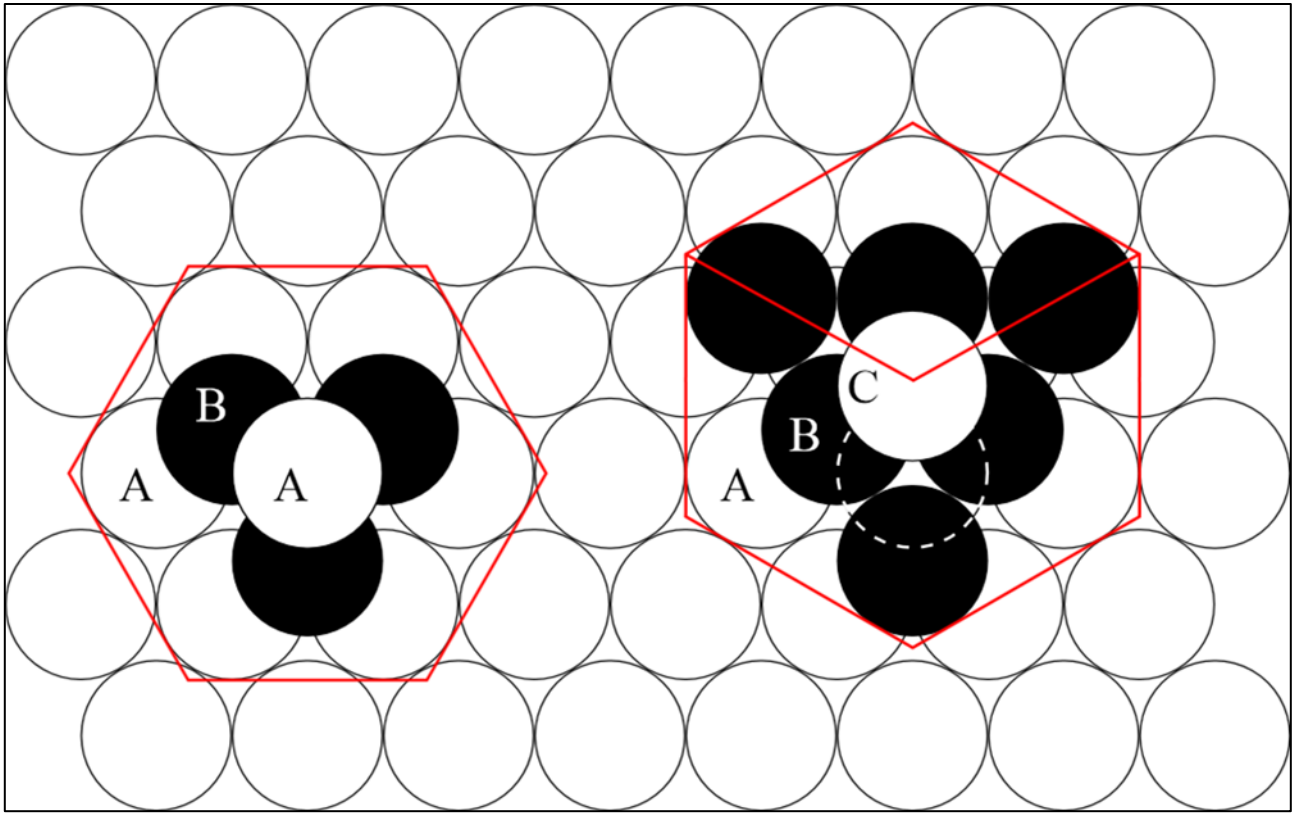

Figure 15. Image depicting the basal plane of 4H SiC. With atom arrangement of a cubic crystal lattice

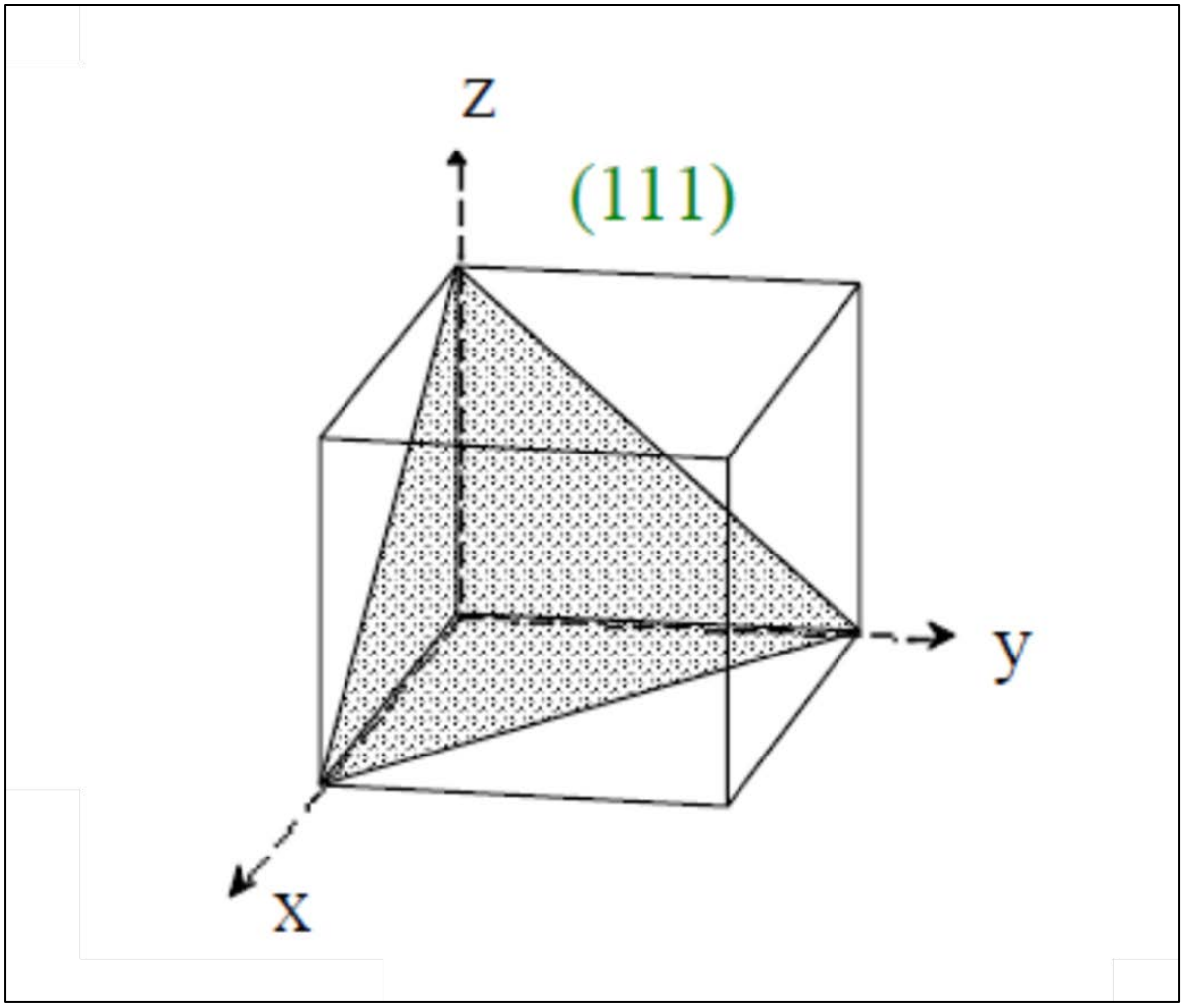

Figure 16. Cartoon Depicting the (111) direction in a cubic system

The majority of the growths on silicon were done on (100) substrates cleaved from 4'' diameter wafers from Wacker Siltronic Corporation, with a resistivity is .009-.020 Ω-cm and doped with boron. Some growths were also performed on (100) Si subtrates, to prepare BP films on higher electrical resistivity substrates for electrical measurements. Thickness of the wafers ranged from 375-425 μm. High quality SiC wafers were used supplied from Cree Inc. and Aymont Technologies. The Cree Inc. wafers were all 3'' nitrogen doped 4H wafers with resistivity between 0.024 Ω-cm and thickness of 348-372 μm. Both sides of the wafer were polished; one side, the epi-ready side, was chemically and mechanically polished to reduce the roughness The SiC wafers have one side carbon terminated and the other side is silicon terminated. SiC wafers, epi-ready on the Si terminated side and others epi-ready on carbon terminated side, were obtained to explore the effects of surface roughness and termination on growth. The Aymont wafers used were 6H on axis wafers Si terminated epi-ready. Resistivity was not specified for the 6H wafers. Wafer crystallographic orientation is an important aspect to consider and varying orientation can allow one to tailor the epitaxial growth. In addition to on axis (0001) orientation, intentional offcuts were tried. Intentional offcuts of 4° and 8° from the (0001) plane from the parallel of the [110] direction (see Figure 14) were frequently used to promote step flow growth.

Summary

The motivation of investigating BP has been presented. Materials advancements that allow operation in extreme environments are an important concept for the evolution of future technology. The physical and chemical characteristics of BP as well as a brief history of its development was presented and showed that BP, has unique challenges to overcome to succeed at high quality growth. More specific information was discussed on the planned BP deposition experiments on Si and SiC substrates. A case was made for the deposition on SiC substrates as opposed to the more traditional Si. Concepts of intrinsic strain inherent to heteroepitaxial

deposition support the idea to attempt BP on substrates with a reduced mismatch as compared to Si. Finally, metrics on the wafers to be used in the work were included to provide sufficing background to the reader for future discussion.

CHAPTER II
REACTOR DESIGN

Background

Success in CVD necessitated the proper design and construction of a CVD reactor. A well designed reactor balances precursor gas flow, temperature, pressure and sample orientation to achieve a high quality product. CVD reactors tend to be customized for the application. An example of this is the differences between CVD reactors for research and those intended for high throughput. The most obvious difference is size. Research CVD reactors are small with small sample sizes and industrial reactors are large and can hold hundreds of wafers. Research reactors tend to be much more adaptable to accommodate changes to process parameters, where industrial reactors are often optimized to perform one function. A far-reaching concept in CVD reactors that is widely used is the tube design. Since the early days of CVD process development, a tubular design has been the foundation for much of the CVD research today. The reason is simplicity. Unlike more complex designs, the gas flow dynamics associated with simple tubes is straightforward. With a few simple calculations it is possible to gain a reliable approximation of the nature and behavior of the gases in the reactor. For a more thorough treatment of the specifics in mass transport in CVD refer to Appendix A.

A custom chemical vapor deposition reactor was constructed for III-V semiconductor deposition. A conceptual drawing of the proposed reactor is shown in Figure 17, followed by a photograph of the actual system in Figure 18. Some discrepancies can be noted, but most of the major elements are present.

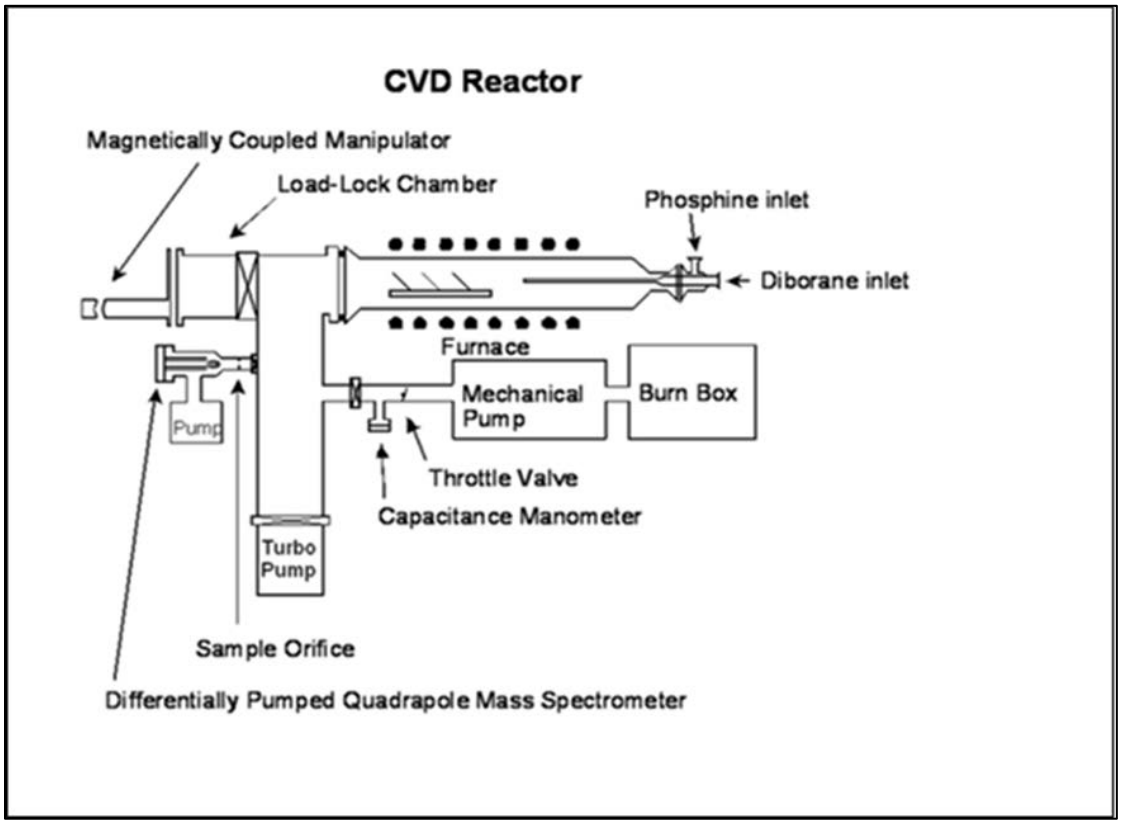

Figure 17. CVD reactor concept

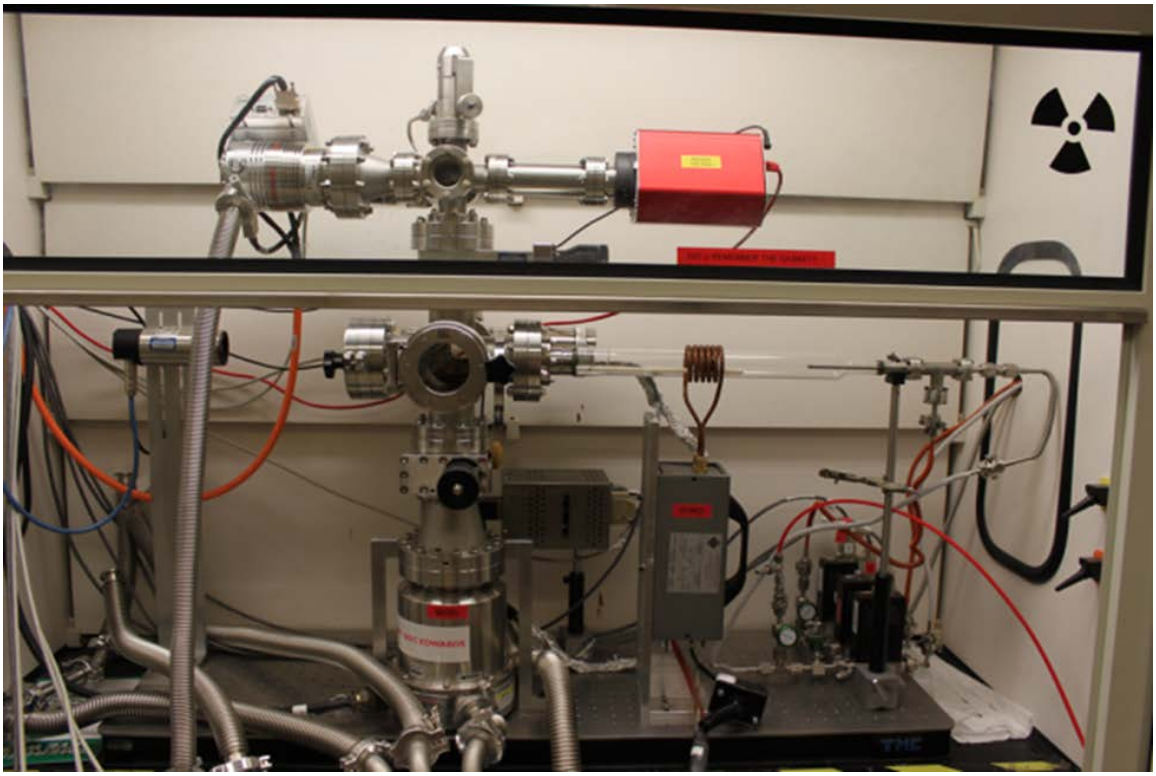

Figure 18. Photograph of entire CVD reactor

The reactor is a medium scale modified quartz tube reactor with a differentially pumped mass spectrometer. Careful consideration was paid to the following topics in CVD reactor design: gas purity, process automation and control, material compatibility and life safety. The following descriptions will detail the individual components of the CVD reactor.

CVD Reactor Components

The tube used in the BP reactor was a 21'' inch long quartz tube with high vacuum flanges on both ends. The left end of the tube terminates with a 2-¾" SS Conflat flange with a quartz to metal seal welded into the flange. The right side of the quartz tube terminates with a 1.33'' SS Conflat flange, again via a quartz to metal seal welded into the flange. The major portion of the quartz tube was constructed from 38mm (1.5") O.D. and 19 mm (0.75") O.D. tubing with a 2 mm wall thickness, which were blown together to produce a tube which narrows from a 1-½'' OD to a ¾'' ID. Typically the 38 mm section is 12" long and the 19 mm section is 4" long, to produce a tube of ~ 21" length. Please see Figure 19 for an image of the quartz tube.

The precursor gases enter from the 0.75" end of the tube and are expelled from the 1.5" end. The 1.33'' end of the tube is attached to a 1.33'' conflat tee. The diborane is supplied via a dedicated bellows from the applicable mass flow controller to the tee. The phosphine and hydrogen carrier gas lines converge upon exiting their respective mass flow controllers and are supplied to the tee as a mixed gas. All three gases converge in the tee and are injected into the reactor tube via a ¼'' diameter stainless steel tube. The tube serves to accelerate the gas velocity which aids in creating a fully developed flow profile prior to contacting the graphite susceptor, which is placed 5.25 inches from the injector tube. A special aspect of the reactor design was use of an alumina rail system to hold the RF heated graphite susceptor and substrate assembly. This arrangement

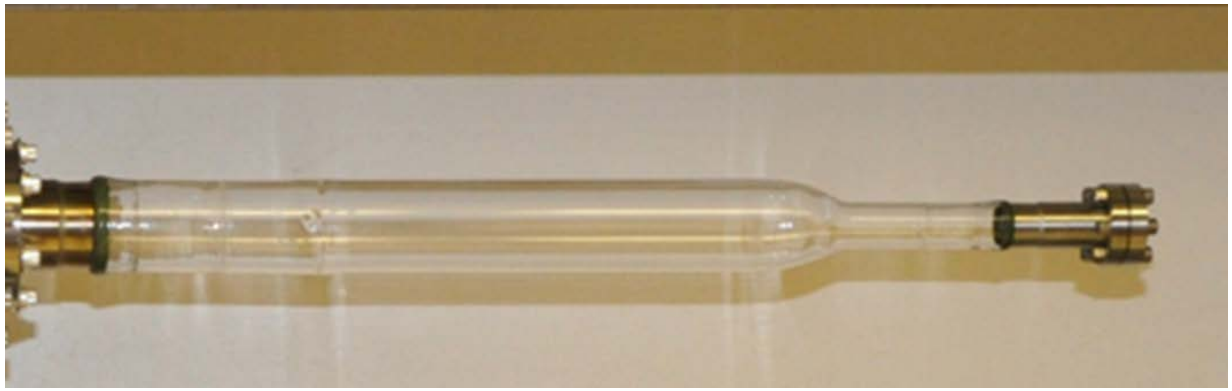

Figure 19. Photograph of quarts reactor tube.

differs from earlier designs where heater blocks rest in contact with the quartz tube. With the rail system, the graphite susceptor and substrate assembly are suspended in the gas flow. This has the important result of limiting the heat transfer from the susceptor to the quartz walls. With this design, the reactor should be considered to be a cold-walled reactor, though there is some indirect heating of the quartz walls through gas thermal transfer. Heating of the quartz walls increases gas phase nucleation and depletes the system of precursors for film growth.

Vacuum System, Components and Pumping

The quartz reactor tube bolts to the vacuum housing, which consists of a 4.5'' conflat six way cross that serves as the main pumping chamber (Figure 20). Two 2 ¾'' conflat 6 way crosses are directly attached to the main housing. The first 2 ¾'' cross is attached to the backside of the housing as seen in in Figure 13. This cross serves as the primary service ports. Attachments to this cross include a Huntington KF 40 manually operated all metal bellows seal valve, which acts as the primary communication between the primary housing and the throttle valve. The throttle valve will be discussed under the section on pressure control. Also attached to this secondary cross included the MKS heated capacitance manometer. This gauge is the primary pressure gauge in the feedback loop associated with pressure control.

Another 2 ¾'' six way cross (Figure 21) sits directly on top of the main pumping housing, This cross creates a small pumping chamber for a Pfeiffer Prisma plus quadrupole mass spectrometer (MS), capable of measuring masses from 0-200 amu. Gas from the main chamber can be introduced into the MS chamber via a Varian high vacuum leak.

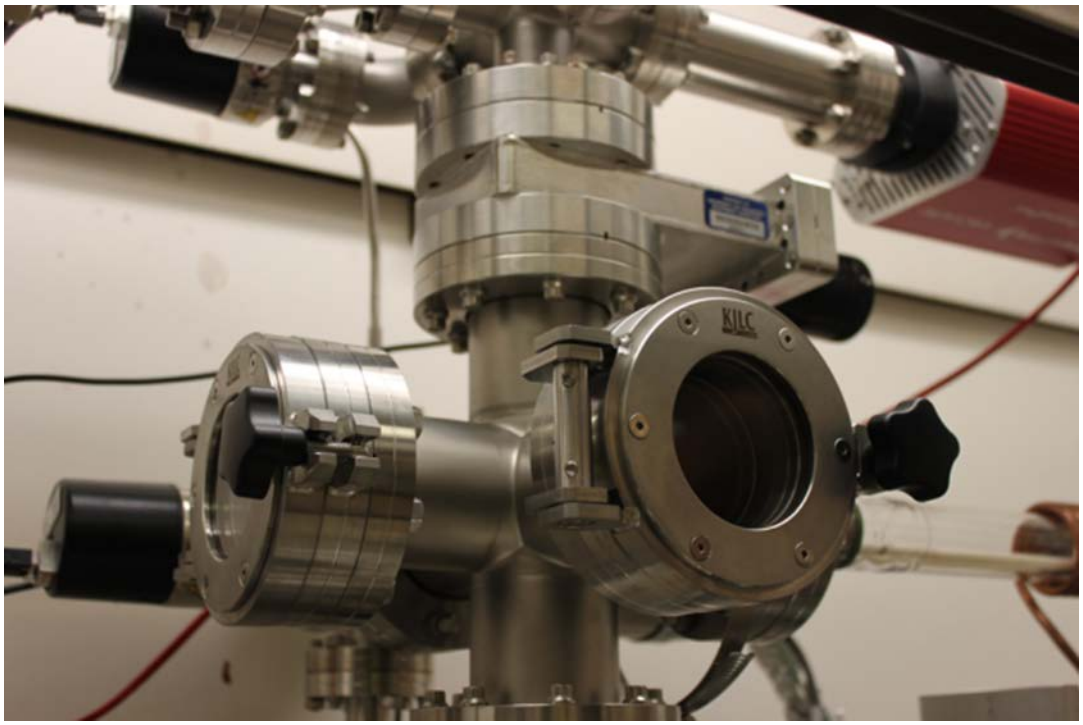

Figure 20. Zoomed in shot of the main pumping housing: note Quartz tube placement in lower left of photo

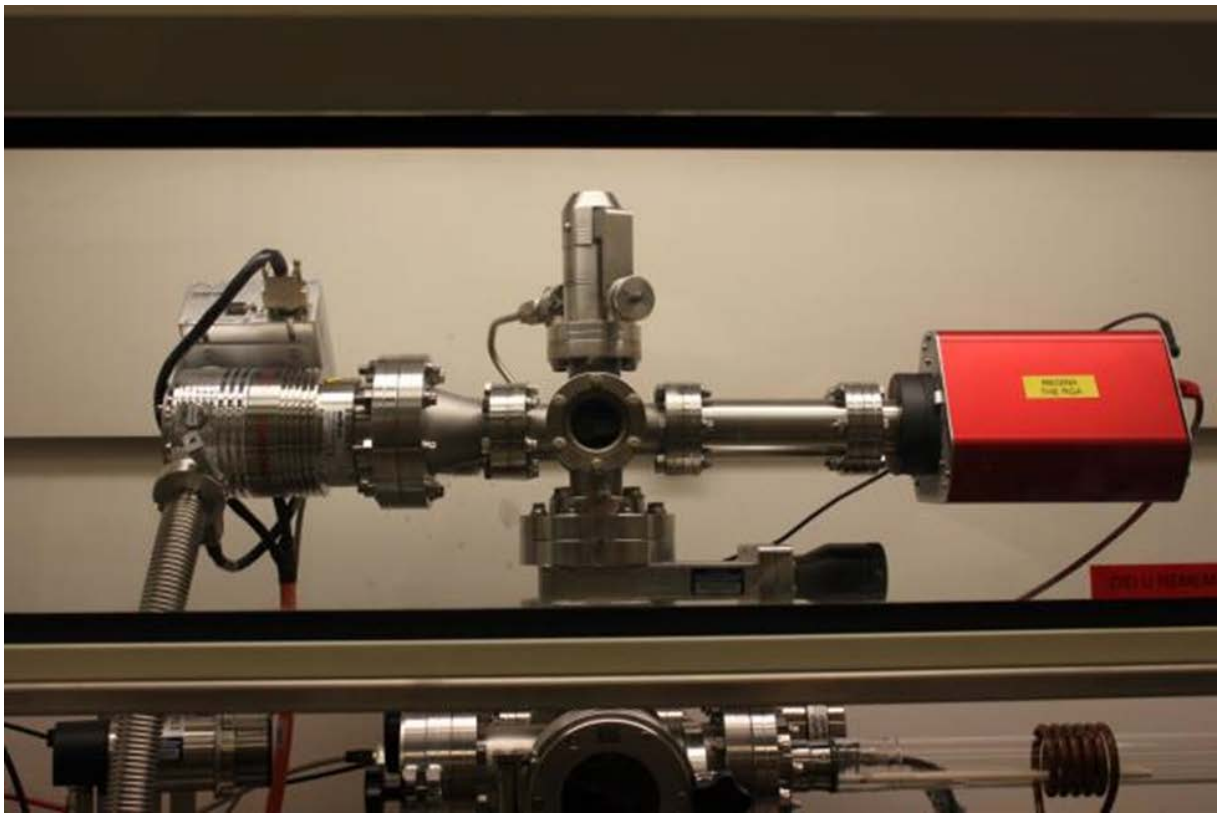

Figure 21. Photograph of differentially pumped MS chamber. Prisma plus in red on right and SL 80 Turbo pump on the left and leak valve on top

This valve is the primary pressure regulator between the main pumping chamber and the MS chamber. The small volume allows the sample gas stream to be introduced but still maintains the MS chamber pressure at approximately 10^{-6} torr. The MS chamber vacuum is supplied by an Oerlikon Leybold SL 80 turbo molecular pump and pressure in the MS chamber is measured by a Leybold Penningvac PTR 90. The PTR 90 is a wide range gauge capable of measuring pressure from atmospheric pressure to 3.75×10^{-9} torr. Nominal vacuum in the MS chamber without the introduction of a sample gas stream is 3×10^{-8} torr.

Maintaining purity is a major challenge in CVD processes. Most often atmospheric constituents such as moisture and oxygen are deleterious to CVD in that these products will react with the precursor gas and form unwanted oxide layers on the substrates. In order to effectively eliminate these species, an effective vacuum pumping system must be established. The main chamber and associated sub- chambers are all constructed from vacuum tight components such as Conflat flanges and Kwik flange vacuum tight fittings. The gas tight chamber must be cleansed of its atmosphere prior to the introduction of the reactive gases. This is done by a combination of scroll, roots and turbomolecular vacuum pumps. A totally oil free pumping system was used to help maintain system purity. The roughing pumps used in this work consist of Edwards XDS 35i and nXDS10i scroll pumps and an Adixen ACP 15. The Edwards XDS35i scroll pump serves as the main pump on the system and communicates directly to the main housing via a 1'' diameter SS bellows. The XDS 35i is used to evacuate the system to $<10^{-2}$ Torr and to pump away the process gases during CVD growth. It is capable of pumping speeds of 21 ft^3/min and an ultimate pressure of 8 $X10^{-3}$ torr. This pump is equipped with a gas ballast adapter which allows the introduction of an argon purge at 3 SLPM, which is needed to clear the pump of hydrogen. Growth of boron phosphide in the CVD reactor generates a considerable amount of particulates downstream from the substrate. To minimize accumulation of particulates in the XDS35i, a particulate filter was

added at the inlet. Even with this measure, the pump requires periodic disassembly and cleaning. Other than its size and bulk, the XDS35i has been extremely reliable and easy to maintain under these demanding operating conditions.

The nXDS10i is a smaller updated version of the 35i. It is capable of a maximum pumping speed of 6.7 ft^3/min and an ultimate pressure of 5 x 10^{-3} torr. This nxds pumps serves in dual capacity as the roughing pump on the MS chamber as well as the backing pump on the SL 80 turbo molecular pump serving the MS chamber. The Adixen acp 15 backs the main chamber turbo molecular pump. The acp 15 is capable of a maximum pumping speed of 8.2 ft^3/min and an ultimate pressure of 2.2 x 10^{-2} torr. Roughing pressures of approximately 10^{-3} torr are not sufficient to adequately eliminate the atmospheric contaminants from the chamber. An Edwards vacuum STP-301 magnetically levitated turbo molecular pump was selected to provide the vacuum for the main chamber and reactor tube. The pump has a 6'' diameter conflat inlet flange, a pumping speed of 300 liters/sec and can achieve ultimate pressures as low as 1 X 10^{-10} torr. This pump rotates at 48,000 rpm and maintains pressure in the chamber during idle periods at 3.X10^{-8} torr.

Gas Handling, Flow and Pressure Control

A literature search showed that the most popular reactions for BP CVD was pyrolysis of phosphine and diborane in a reducing atmosphere. Although the use of halide based precursors have the advantage of a higher decomposition temperature which would reduce effects of gas phase nucleation, hydride precursors yield hydrogen as the byproduct and have the potential for producing films of the highest purity. The decision was made to emulate this proven reaction. A 1% solution of diborane in hydrogen and a 5% phosphine solution in hydrogen was selected as the gaseous precursors. The gases were balanced with high purity hydrogen for a carrier gas. The semiconductor gases supplied form Matheson Tri-gas are 99.999% pure UF cylinders with 7.6 L

internal volume. In order to maintain high purity, all components wetted by the gases were made of cleaned 304 stainless steel. In areas where metals were not feasible such a valve seals, compatible polymers such as Kalrez and Viton were used. All fittings used in the process piping of the gaseous precursors are high purity face seal fittings. Swagelok VCR components were used to connect process lines. Connections to gas cylinders were also high purity face seal type. CGA 632 fittings were specified on the phosphine and diborane cylinders. Figure 22 shows example position of both sets of high purity fittings.

Figure 22. Precursor gas handling system. Showing high purity fittings position and components

In addition to high purity fittings additional equipment was used to ensure process cleanliness. All process gas supply lines were outfitted with cross purge assemblies; a specific configuration of valves and piping that allows atmospheric contaminants to be purged from the supply line once a connection has been made. Refer to Figure 23 for an image of a standard cross purge assembly.

An important aspect to CVD is accurate and reliable pressure control. As previously mentioned, CVD process tend to be defined by the pressure level at which processes take place. One of the primary contributing factors to total system pressure is the flow of the gaseous precursors. For this purpose, the pressure control and flow control mechanism will be treated together. In order to establish a steady deposition pressure, an equilibrium (steady state) condition must be established between the gas entering the reactor and being pumped out by the vacuum pump. This is accomplished by a feedback loop between a pressure gauge and a throttle valve. The MKS T3BI throttle gauge position is shown in Figure 24 is positioned between the main service pump and the central housing. The T3BI operates by opening and closing at high speed to maintain a set point pressure. The pressure in the main housing is measured by a MKS 628B capacitance monometer with a heated diagram to prevent unwanted condensation from interfering with pressure measuring ability (Figure 25). On the supply side, the gaseous precursors are metered in to the reaction chamber via three MKS 1479A mass flow controllers, each dedicated to a specific gas and calibrated in a specific flow range (Figure 26). The Diborane mass flow controller allows gas flow set point in a range of 1-100 sccm.

Figure 23. Photograph of Cross purge assembly with attached high purity regulator

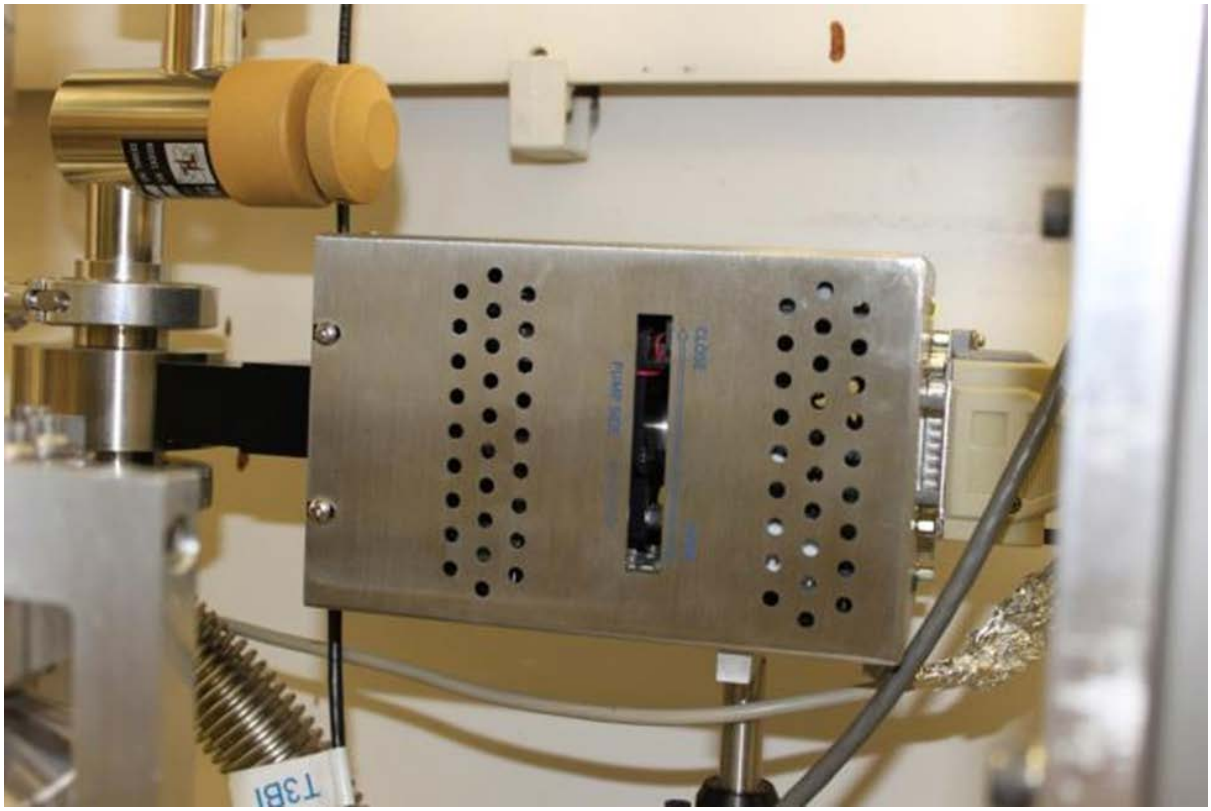

Figure 24. Photograph of MKS T3Bi Throttle valve

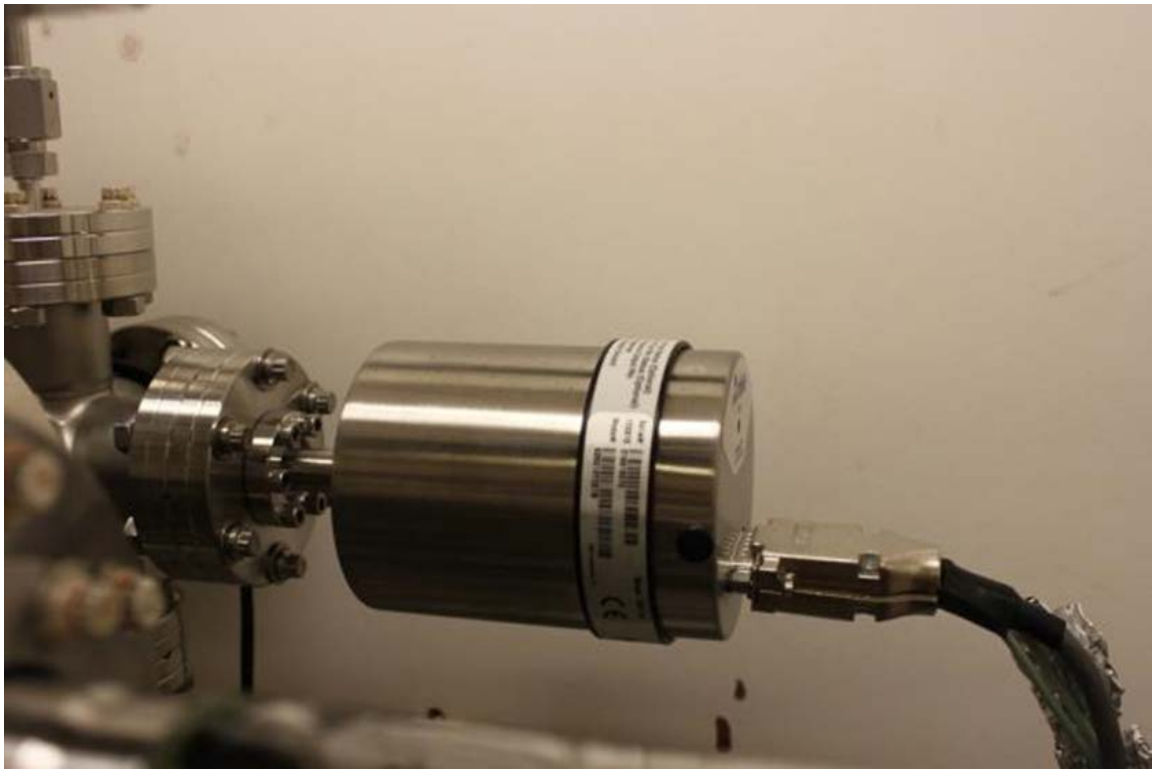

Figure 25. Photograph of MKS 628B Capicatance manometer

Figure 26. Photograph of MKS 1479A Mas flow controllers for diborane (front) Phosphine (middle) and Hydrogen (rear)

The phosphine mass flow controller allows flows from 1-1000 sccm. The third mass flow controller range is the highest with a flow range from 1-10,000 sccm. Since hydrogen is used as both balance gas and carrier gas, all mass flow controllers are calibrated with hydrogen.

The CVD is remotely controlled via a Labview Graphical User Interface (GUI). The GUI communicates via a national instruments data acquisition hub docking port that receives data from the T3BI throttle valve, 6288B capacitance manometer and MKS 247D power supply and signal conditioner which controls the 1479A mass flow controllers (Figure 27). The Labview GUI automates flow and pressure set points as well as the emergency shutdown. Refer to Figure 28 for a screenshot of the GUI.

RF Heating and Susceptor Design

In addition to pressure and flow, one of the most important aspects of CVD is the heat source. One of the most common approaches, and the one leveraged in the work is pyrolysis. In pyrolysis, the gaseous precursors are passed through a heat affected zone. As the gas enters the heat affected zone, it disassociates into individual components. Using diborane as an example, the pyrolysis equation would be

$$B_2H_6 + \Delta \rightarrow 2B + 6H$$

In order to efficiently crack hydrides, the temperature must be above 500 °C, but to remove native oxides from the surface of Si and SiC wafers, temperatures need to exceed 1000 °C. Therefore the heating method must be capable of high temperatures and be capable of maintaining a set temperature for extended periods of time. The heating method that met these criteria was radio frequency (RF) induction. Induction heating is a proven method for CVD. Here a susceptor, or material that couples well in the RF, is placed in the reactor. A chilled water cooled copper coil,

Figure 27. Photograph of MKS Type 247 Signal Conditioner and power supply

Figure 28. Screenshot of Labview GUI. Showing Control Features

which serves as the RF source is placed around the exterior of the reactor tube (Figure 29). Voltage is supplied via a power supply thus heating the susceptor (Figure 30). The RF heater is the Ameritherm Easyheat 0224. This heater has a maximum power output of 2.4 kw over a range of 150-400 hz. The susceptor material chosen for the BP deposition was graphite. The susceptor was machined to sit flush on a custom rail mount system.

Figure 31 shows the rail mount system and Figure 32 shows the custom graphite susceptors. The alumina rods are inert in the RF field and work to keep the susceptor suspended in the reactor tube. This serves a dual purpose in keeping the susceptor from having direct contact with the quartz tube and eliminates localized sources of heat. It also provides much needed gas flow around the susceptor, reducing the magnitude of gas turbulences at the susceptor surface.

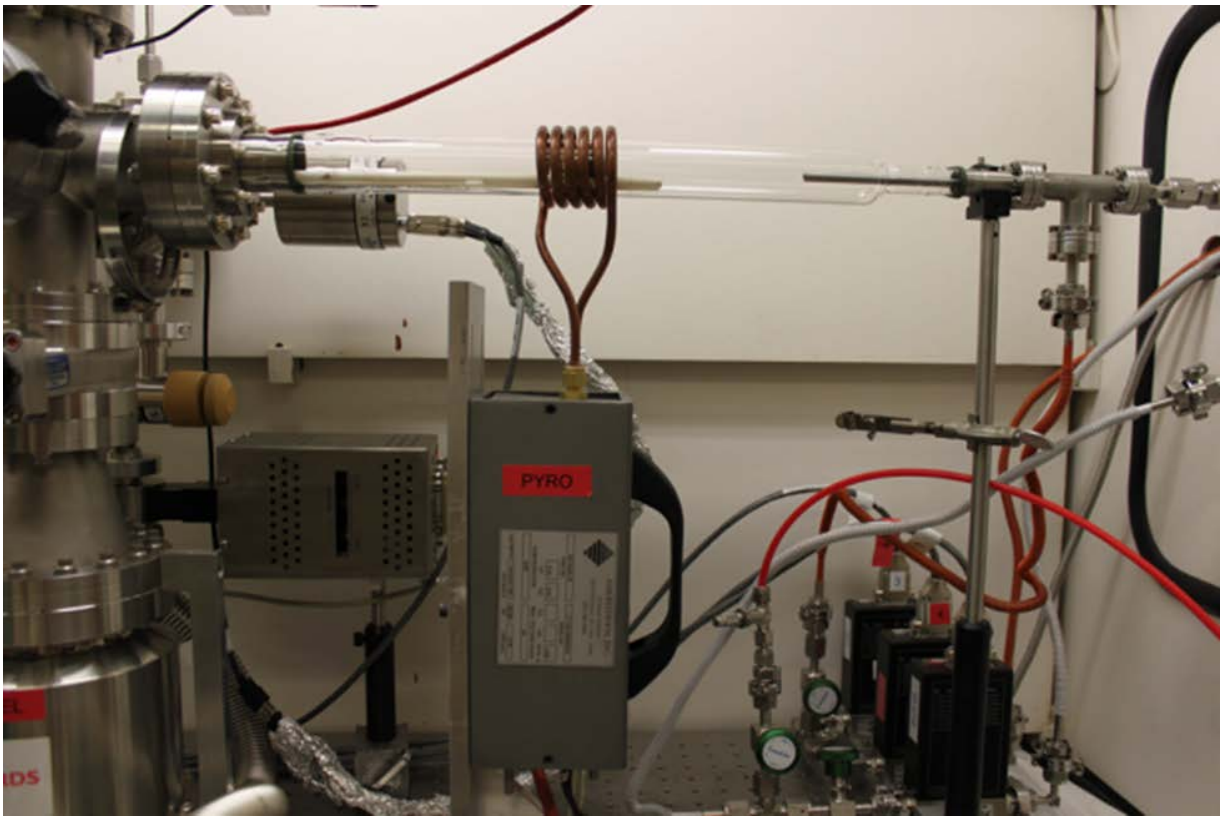

Figure 29. Photograph of RF induction heater coil around quartz reactor tube

Figure 30. Power supply form RF induction heater

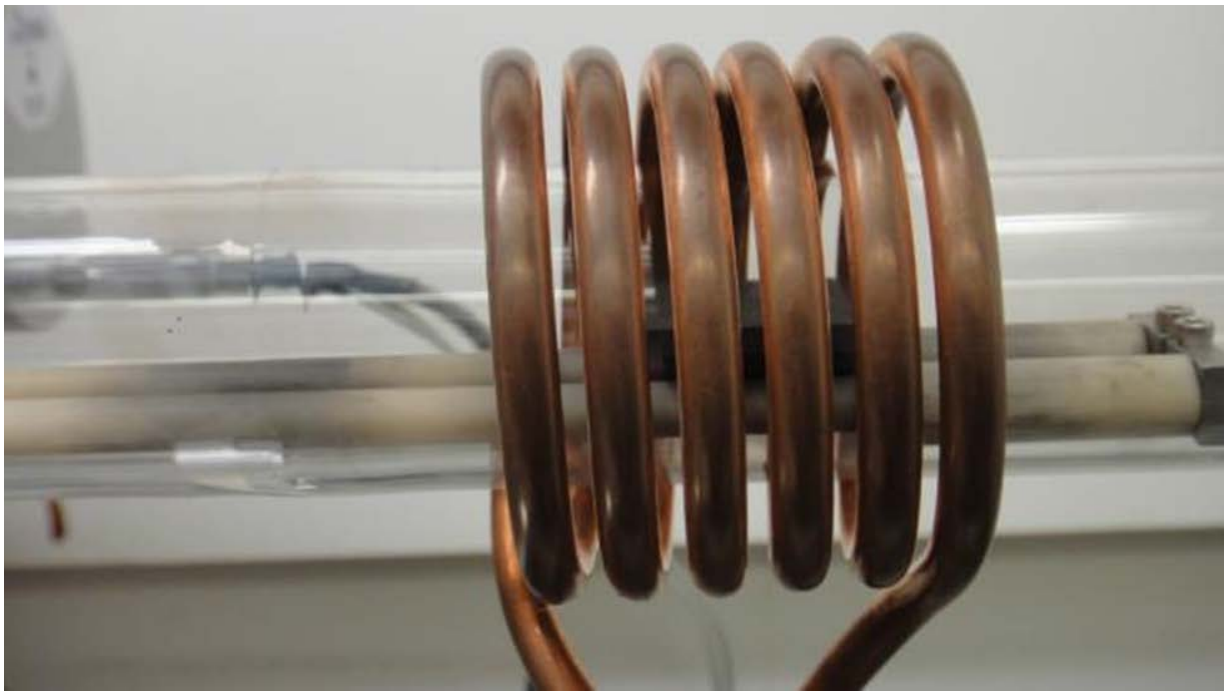

Figure 31. Photograph showing custom railmount system. Graphite susceptor is visible between copper coils

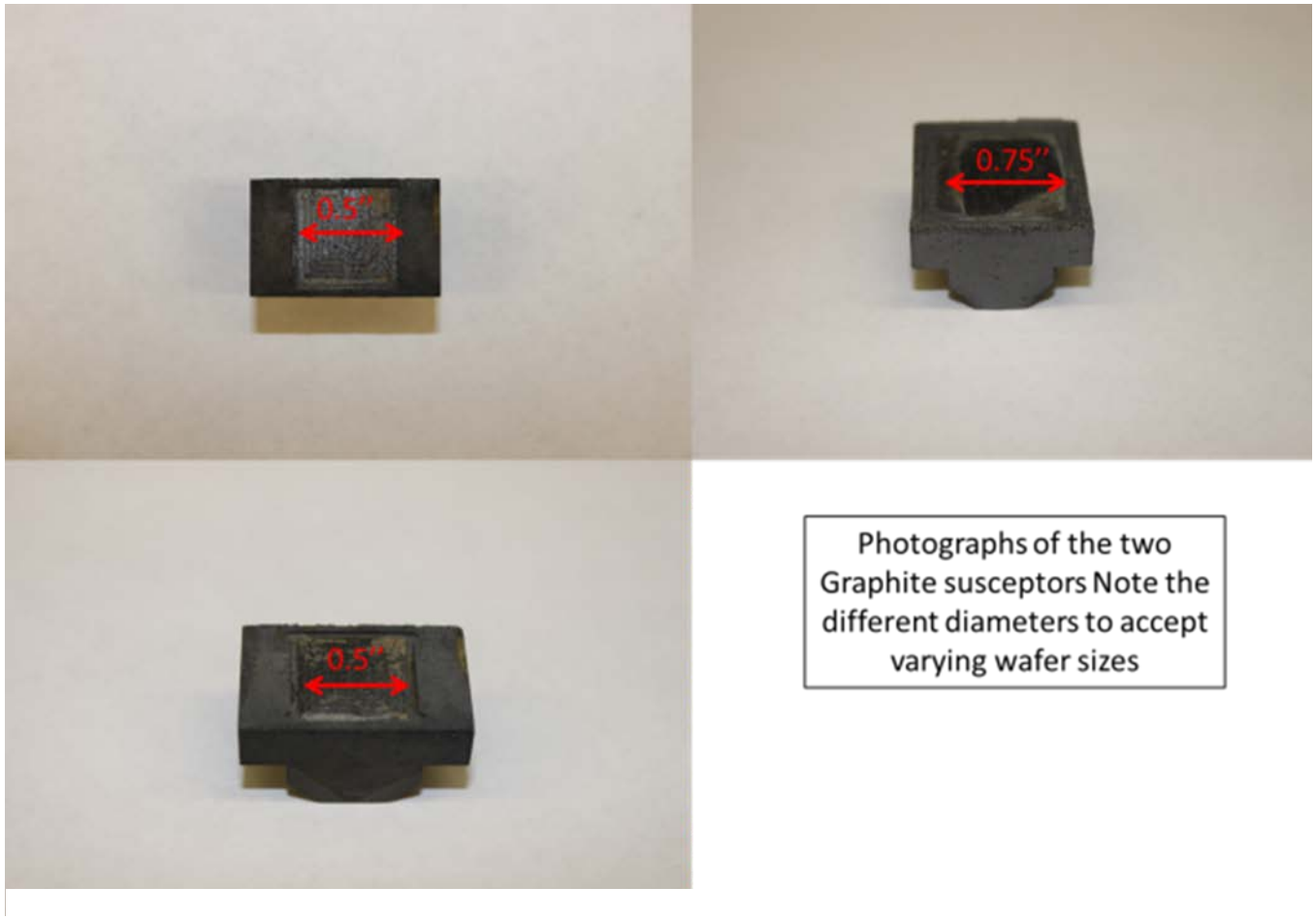

Figure 32. Photographs of Graphite Susceptors used in this work.

Susceptor Temperature Measurement

Temperature measurement in the CVD reactor is challenging. Noncontact temperature measurements were selected over standard thermocouple for a more simplicitic reactor tube design as well as gas flow dynamics. Non-contact methods of heat measurements include techniques that look at radiative heat transfer, such as optical pyrometers and IR thermometry, both of which were used in this work. The disappearing filament optical pyrometer (Figure 33) was used to measure the temperature of the graphite susceptor. Ideally, in CVD it is more advantageous to measure the substrate temperature. However, in this specific configuration, it was impossible to focus optics on the substrate due to interference from the copper coils. Also, the changing substrate materials from Si to SiC complicated noncontact measurements because one instrument was not able to measure both Si and SiC due to differences in emission wavelength. The decision was made to use the temperature of the graphite susceptor as the indication of substrate temperature. At this time there is no data to correlate the two measurements, an assumption is made that the difference in temperature of the graphite to the substrate is small enough to negate a significant variability. Therefore the temperature of the susceptor and substrate are used interchangeably in these experiments. The disappearing optical pyrometer works by the user visually comparing the color of a filament with the color being emitted from the heated object. The filament is adjusted by the user dialing a rheostat.

Figure 33. Disappearing Filament Optical Pyrometer[75]

Once the color of the filament matches the color of the heated object, the temperature can be inferred if the emissivity of the heated material is known. The other method of temperature measurement used is infrared (IR). The Raytek Marathon 2MH IR pyrometer (Figure 34) has a temperature measurement range of 450° C to 2250° C with a spectral response of 1.6 μm. The IR camera has an integrated target that allows the sensor to be accurately placed. User input consists only of material emissivity and focal length. Since this method relies less on visual comparisons, it is considered slightly more accurate. A correlation study was conducted between the disappearing filament optical pyrometer and the IR pyrometer by comparing simultaneous measurements of the graphite susceptor. Numerical agreement between both techniques was within 15 degrees Celsius.

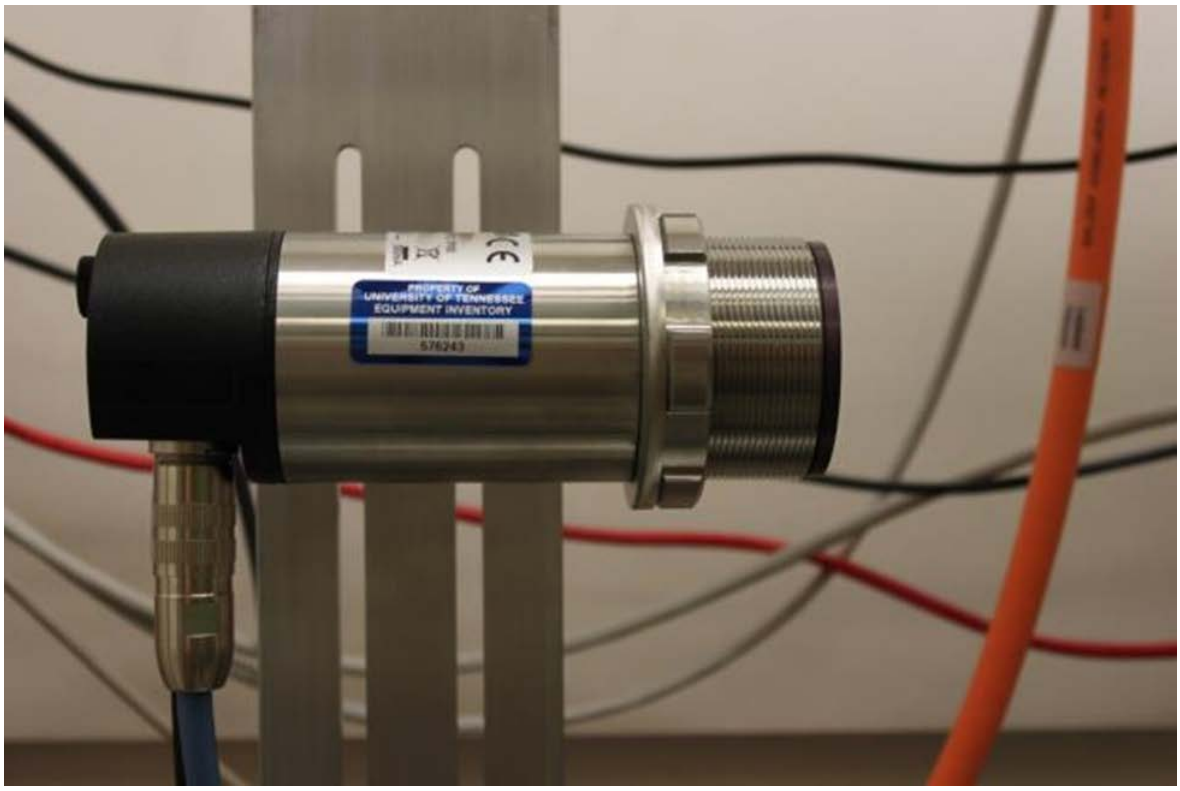

Figure 34. Photo showing Raytek IR pyrometer

Safety Measures

Similar rigor was applied to designing systems to safely abate any free gas and to properly handle system effluent. The CVD reactor was designed to fit inside a large fume hood. The hood with reactor inside for scale is shown in Figure 35. When experiments are conducted, the hood is set to emergency flow mode. This keeps the concentration of any gas that may leak from the reactor at an absolute minimum. In order to safely store the diborane and phosphine cylinders, a gas cylinder cabinet was procured to provide a local constant ventilation of the cabinet surrounding the cylinders. The cabinet shown in Figure 36 is all metal and provides cylinders straps to stores the cylinder. Mounting racks are also provided to support the gas supply panels for each gas. Equally important is the process exhaust. During pyrolysis, it is expected that the majority of precursor will be sufficiently disassociated and or reacted to inert species. However, in the unlikely event of a scenario of gas flowing through the system unreacted, a scrubber was placed to capture any unreacted precursor. The scrubber consists of a gas tight right cylinder tank filled with a 50% solution of potassium permanganate ($KMnO_4$). Being a strong oxidizer, the KMnO4 oxidizes the diborane and phosphine into borates and phosphates respectively. A photo of the scrubber is shown in Figure 37. Although less toxic that diborane and phosphine, hydrogen makes up the balance of the gas constituents in the system. Hydrogen will not react with the oxidizer and must be addressed another way. The most common way to neutralize combustible gases is to burn them in a controlled atmosphere. An example would be a burnbox. Unfortunately, the total hydrogen flow through the reactor was too high for a burnbox scalable to the laboratory.

Figure 35. Photograph of reactor in fume hood with sash closed

Figure 36. Photos of Hazardous gas cabinet Exterior (top) and Interior (bottom)

Figure 37. Photograph of potassium permanganate scrubber Showing Inlet and exhaust lines

In lieu of burning the hydrogen, the hydrogen effluent is diluted with nitrogen in a ratio of 10:1. The nitrogen is supplied via 240 L liquid nitrogen Dewar (Figure 38). A flowmeter is attached to the gas service port on the Dewar which connects to the scrubber exhaust line. Hydrogen abatement is also required for the primary scroll pump. Light gases tend to entrain in scroll pumps and need to be purged to ensure an explosive mixture is not created. In order to provide an inert environment in the pump, an argon purge line is attached to the primary scroll pump. A gas ballast adapter was acquired which allows the introduction of up to 3 SLM/min of argon inside the scrolls. This prevents any hydrogen from accumulating as well as eliminating an explosive mixture from building inside the pump and minimizes the reduction in pumping speed.

An additional layer of personnel safety is provided in the form of active detection of the hydride gases. A phosphine gas sensor is present in the vicinity where an amount of phosphine may accumulate if the system failed to function properly. The sensor is a hydride sensor and will also detector the presence of diborane. However, it is not calibrated for diborane and the response range for diborane is not predicted thus no credit for safety is taken for diborane crosstalk. The sensor inserts into the Drager Polytron 7000 detector (Figure 39). This detector is capable of continous gas monitoring and is calibrated with dual alarm set points of 1 ppm and 10 ppm. The sensor is connected to the Drager SC04135 remote alarm station. The remote alarm station shown in Figure 39 has an audio alarm and a red and amber strobe. The strobes are wired to the action levels set points from the Polytron 7000. The amber strobe activates at the 1ppm threshold. The audible alarm and red strobe activate at the 10 ppm threshold. In order to ensure proper response to alarms, an industrial hygiene plan was developed that outlines the personnel action required upon the activation of the alarm set points.

Figure 38. Photograph of 240 L liquid nitrogen Dewar used to supply dliuent gas. Shown with attached regulator and flowmeter

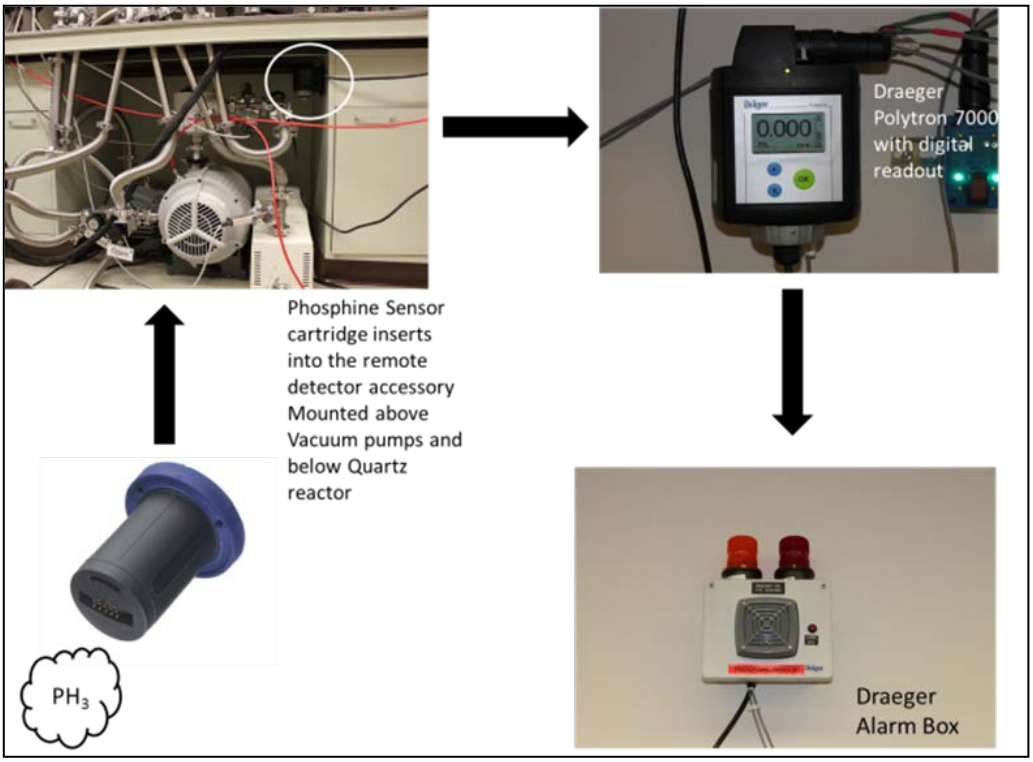

Figure 39. Figure showing components of the active gas detector system. The arrows denote signal flow

Function Testing

At the conclusion of the construction phase of the CVD reactor, experiments were conducted to verify successful operation of the reactor and establish confidence in the reactors ability to consistently perform. Initial function tests centered on the ability of the CVD system to maintain the setpoint pressure. In these tests, the mass flow controllers and throttle valve were operated across a wide range of flows and setpoint pressures readings were taken on the capacitance manometer and compared to the setpoint pressure selected in the GUI. An important note is that nitrogen was used in lieu of hydrogen for these tests as a safety precaution. Some variability could be expected in the MFC since they were calibrated for hydrogen, but this was accounted for. Setpoint pressures were unaffected by the gas substitution as the capacitance manometer is independent of gas type. Upon the successful testing of the gas supply system, function test shifted to heating. The graphite susceptor was placed in the reactor tube upon the aforementioned rail system in the middle of the copper coils that surround the tube exterior. The CVD system was evacuated to 10^{-7} torr and the RF power switched on. The power was ramped in a stepwise fashion. The temperature of the graphite susceptor was measured and recorded at each step. This data was used to gauge the heaters efficiency in vacuum. Follow on experiments with heating included repeating the process described in vacuum with nitrogen. Operating the MFC with the RF power on was a technical challenge. Due to the close proximity of the MFC's, CM and throttle valves with the RF heater, significant noise was observed in the return signal from these instruments in the GUI. As a result, the instruments were inoperable in the presence of the RF field. To remedy this, a fine copper mesh was applied on top of the quartz tube encompassing the copper coils of the RF heater (Figure 40). This mesh was grounded to the body of the system,

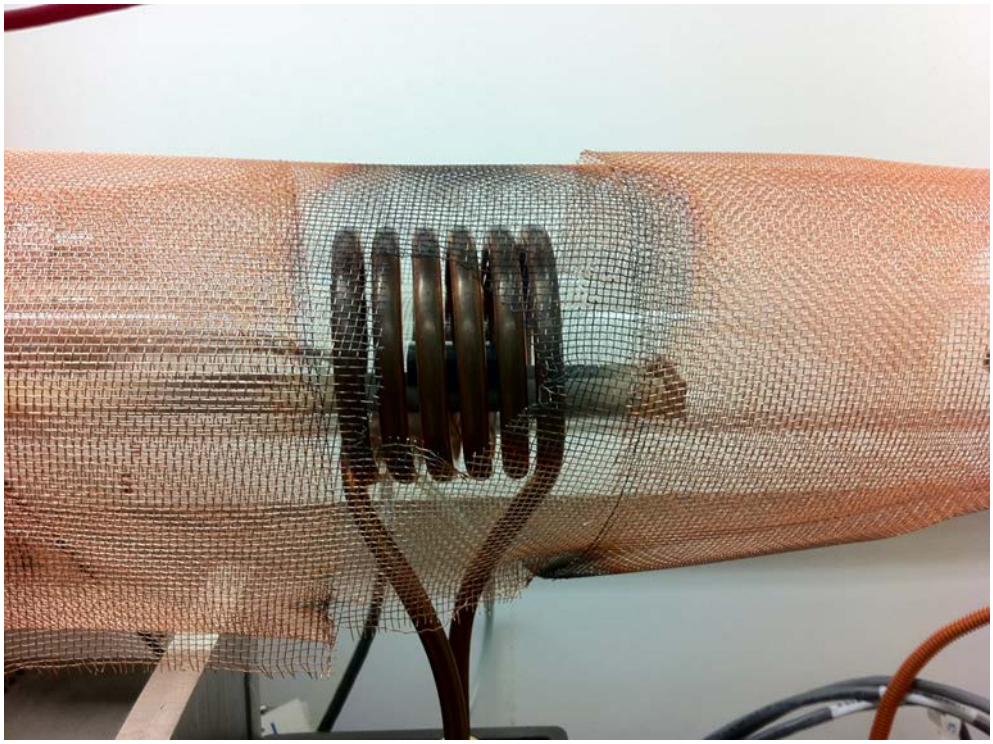

Figure 40. Photo of copper mesh Faraday cage applied to quartz reactor tube

creating a Faraday cage. The Faraday cage was successful at minimizing the noise and allowed for successful operation of the gas flow system while heating.

BP Characterization Techniques

Success in boron phosphide deposition relies on the comprehensive characterization of the deposited thin films. Analytical characterization provides useful information in confirming the presence of boron phosphide and the stoichiometric ratio. As previously discussed, other allotropes of BP are possible. Morphological characterization is useful, in that it can provide information on thin film nucleation and growth. This provides a mechanism of tailoring future experiments to achieve the desired crystal form. In order to address the aspects of comprehensive characterization, several analytical tools and techniques were employed in this work in order to provide feedback to enhance future experiments.

Raman Spectroscopy

As a screening tool Raman spectroscopy provides useful information regarding the presence of BP on a sample. The technique of Raman spectroscopy was developed in the late 1920's when C.V. Raman wrote a letter describing the Raman Effect. The Raman Effect is akin to other types of light scattering, such as Rayleigh and Tyndall. Raman scattering is an inelastic type of light scattering where the molecule is changed by incident photon by a prescribed amount. The incident photon, typically a collimated monochromatic source most commonly a laser, imparts energy to the target molecule. The molecule reacts to this energy influx by changing both its vibrational and rotational energy. Energy is conserved in this process, thus establishing that the energy of the incident photon must be different from the energy of the molecule. Quantitatively this relationship can be expressed by the equation

$$hv_i - hv_s = \Delta E_m$$

Where hv_i and hv_s are the energy of the incident photon and energy of the scattered photon respectively. This equation forms the basis of the dual stokes and anti -stokes scattering common to Raman spectroscopy (Figure 41). If the sample molecule gains energy, then ΔE_m is positive and stoke scattering predominates. In contrast, if the molecule loses energy, ΔE_m is negative giving rise to anti- stokes scattering. Due to thermal dependency and inherently weaker signals, anti-stokes scattering is rarely measured. Selection rules for Raman differ from infrared spectroscopy in that a Raman spectrum is generated from a polarizabilty process rather than a dipole moment shift. To examine this further, consider a molecule of interest placed in an electromagnetic field. The physical forces will align the electrons and the protons in a fixed relationship relative to the applied field. This induces a dipole moment shift in proportion to the strength of the applied field in the molecule. The equation below simplifies the relationship.

$$\mu=\alpha E$$

The dipole moment (μ) is the product of the polarizability of molecule multiplied by the electromagnetic field magnitude. Rearranging for polarizability gives the equation:

$$\alpha=\mu/E$$

or the dipole moment divided by the applied field magnitude. Therefore the polarizability can be described as the transient misshaping of the molecule's electron cloud by the applied field. A molecule must have this polarizabiltiy change to be Raman active. This leads to one of the advantages of Raman over infrared. Water has weak signatures in Raman bands compared to the infrared where it predominates the spectrum.

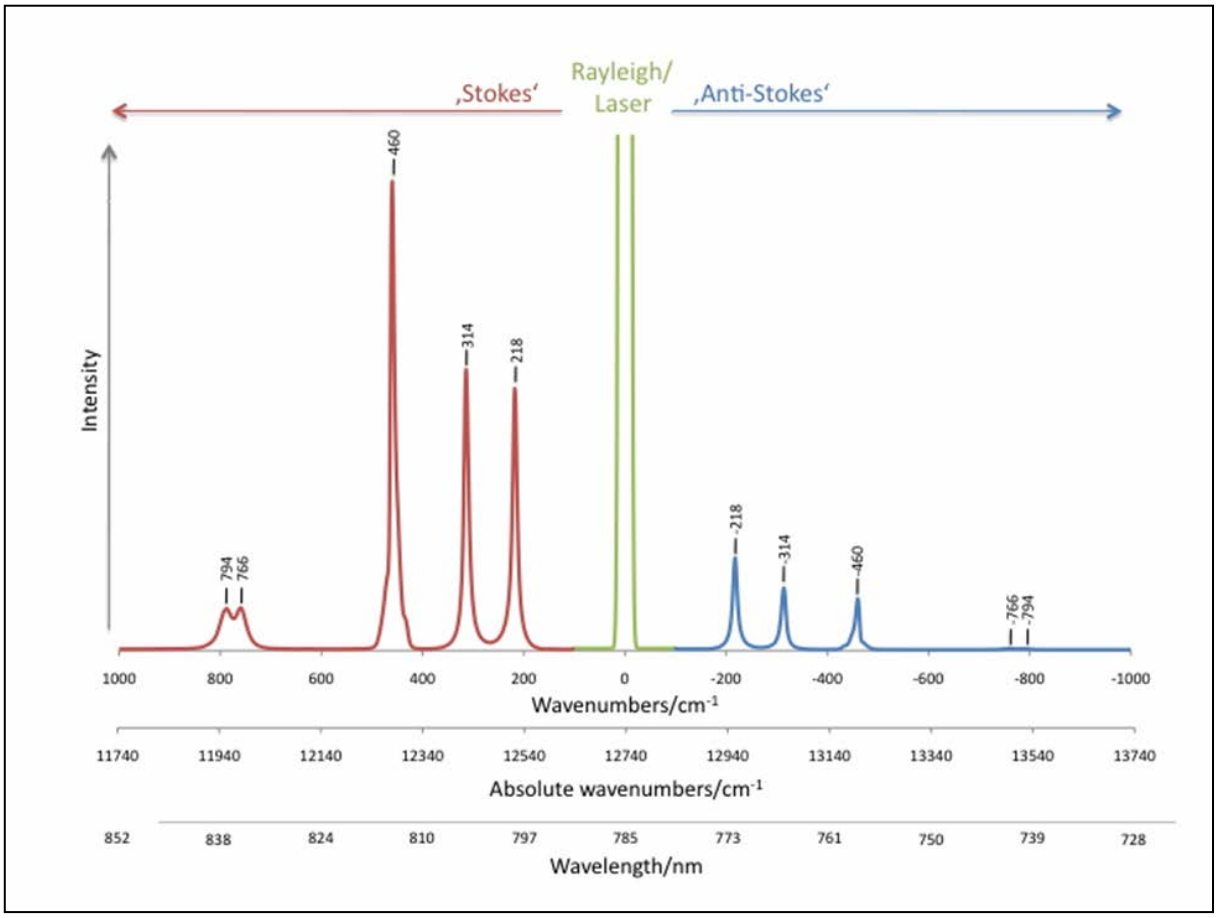

Figure 41. Sample Raman spectrum showing Stokes and anti-Stokes scattering

Raman spectroscopy instrumentation is straightforward. The typical set up involves a laser source in a specified wavelength. The most commonly used excitation wavelengths for broad applications include the 488 and 514.5 nm argon–ion lines. With the advent of solid state lasers, other wavelengths that are much easier to be achieved are currently being explored. One disadvantage to Raman spectroscopy is that scattering is dependent on the excitation wavelength. Raman scattering decreases to the fourth power of the excitation wavelength. Therefore, an inherent lower scattering is observed in the shorter wavelength lasers. This is a generalization and special sample configurations and matrices may necessitate going longer wavelength lasers. Aside from the source, other notable aspects of Raman instrument design include the a 90 degree orientation of sample from the source and specialized optics to further refine the incident light and finally detector of some type. This can be a CCD or photomultiplier tube. Figure 42 shows a schematic triple monochrometer Raman spectrometer utilized in this work. The key difference in the triple monochrometer from a more typical single monochrometer is resolution and range. The cost of a triple stage instrument is analysis time. However, for normal material analysis, analysis time is a non-issue. Raman spectroscopy is applicable to a variety of sample matrices. Solids, liquids, and high pressure gases can all be probed via Raman spectroscopy. When analyzing bulk samples, Raman spectra can provide useful information in the area of fingerprinting. By taking advantage of the sharp bands typically associated with pure samples, Raman spectroscopy can be used to identify unknowns by direst comparison to cataloged spectra of known compounds. Additional aspects of bulk Raman techniques apply to crystallography. Bulk Raman analysis can be used to determine crystal vibrational modes as well as provide insight into crystal order and phase transitions. Crystal defects can also be probed via Raman by comparing spectra results to known ordered systems. More specific to materials analysis, Raman spectroscopy can be coupled to a microscope to achieve higher resolving power on the order of a few microns.

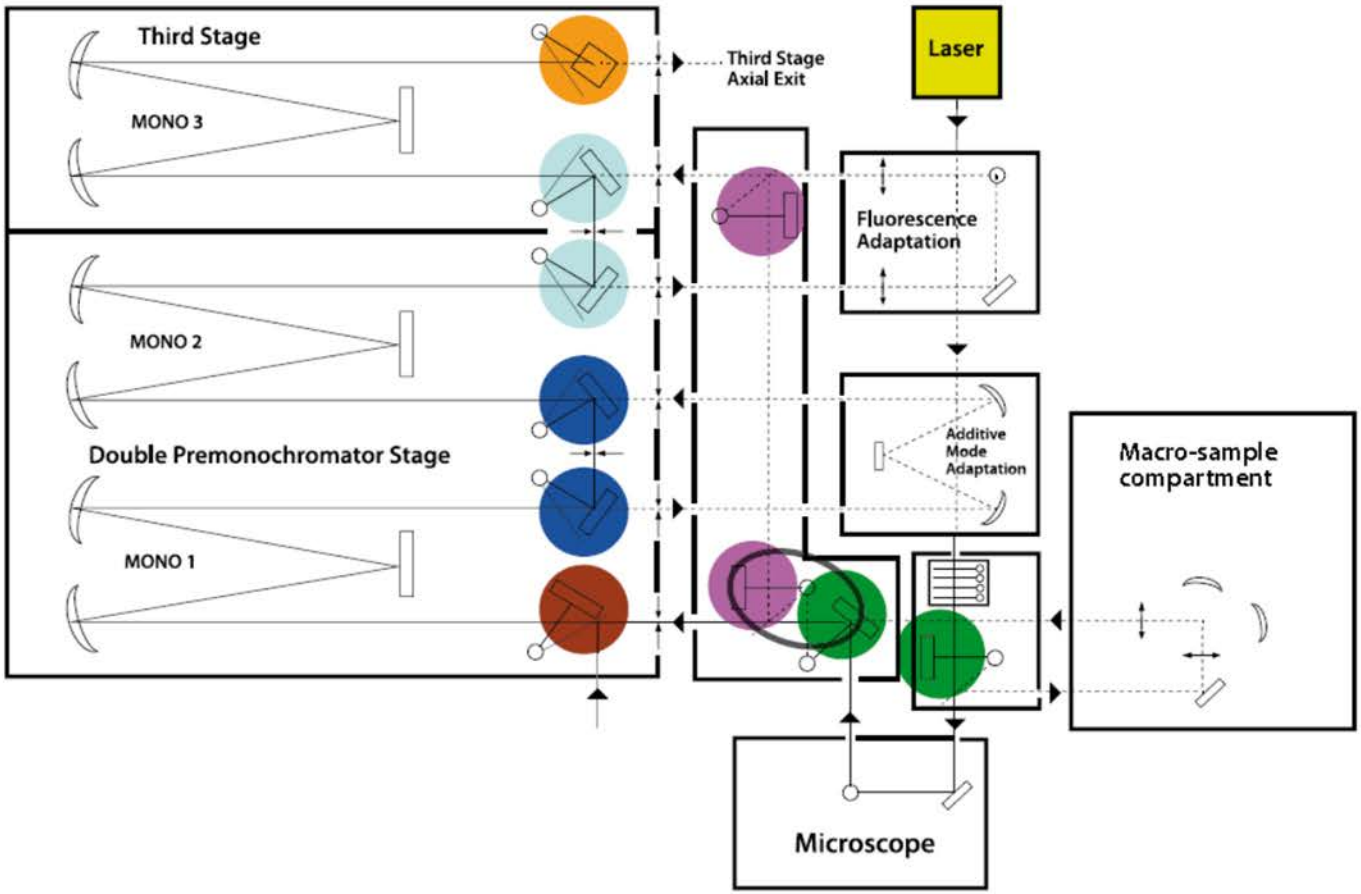

Figure 42. Sample schematic of a triple monochrometer Raman spectrometer[74]

This microscope coupling allows much more focused analysis in solids and thin films which can be used to understand individual grains and grin boundaries in solids. Microfocus Raman can even be used to gauge inherent strain in materials by small shifts in the peaks coupled with line broadening. With analysis capability at both the bulk and microscale, Raman spectroscopy can be a powerful tool for materials analysis.

X-Ray Diffraction

The structural information obtainable from Raman spectroscopy is somewhat limited in depth. Strictly controlled analyses must be performed in order to properly interpret the subtle signatures associated with probing crystal structure with Raman spectroscopy. It is often necessary to use a much more definitive technique to examine crystal morphology. One of the most widely used tools in this area is X-Ray diffraction (XRD). One of the big advantages XRD offers over other techniques aimed at examining structure, is that it is nondestructive. XRD can be used for most materials, but sensitivity scales with Z. Low atomic number materials can be problematic in terms of low intensity. The type of information from XRD tends to vary, based on the material and matrix of the sample being evaluated. Generally, XRD probes crystal phases in materials and XRD spectra can be used to garner information regarding grain size, epitaxial relationship, preferred orientation, and defect propagation.

XRD works on the concept of x-rays interacting with an array of atoms. In an ordered crystalline solid, the diffraction of the X-rays will differ in alternate directions as a function of the ordered arrangement of the atoms. This interaction leads to a relationship between the wavelength of the x-rays and the empty space between the crystal lattice planes and the angle of the impinging x-ray. This is known as Bragg's law and is defined by the following equation:

$$\lambda = 2dsin\theta$$

Diffraction is only observed when the detector is positioned at the diffraction angle of 2θ. Refer to Figure 43 to see an example of XRD in ordered solids. The sample must be positioned such that the defined crystal plane is coplanar with the X-rays in order that the angle between the incident X-rays and the diffracted x-rays is equal to the Bragg angle which can be determined by the equation above. Consider the simplest crystal structure, a single face centered cubic structure. In this system there is only one set of conditions equal to the Bragg angle. However, in more complex systems such as polycrystalline films or amorphous solids, there is a distribution of orientations possible. As crystal systems are more ordered, the number of possibilities that satisfy the Bragg condition lessen and more information on sample crystal phase, strain and preferred orientation can be gleaned from the spectra.

Thus far, the previously described methods of materials analysis have been purely spectroscopic in nature. The information available from spectroscopy is rich; there is no substitute for visual analysis in material synthesis. Visual analysis allows one to quickly see the fine structure of a crystal or thin film and to qualitatively determine its pedigree. Some of the most powerful materials analysis techniques combine aspects of visual analysis and spectroscopy, a brief mention of some of these techniques will follow later in this chapter. The term visual analysis can mean a variety of different things. Bulk visualization with the naked eye is not sufficient for meaningful analysis. The information critical to material characteristics exist only at the microscale and below.

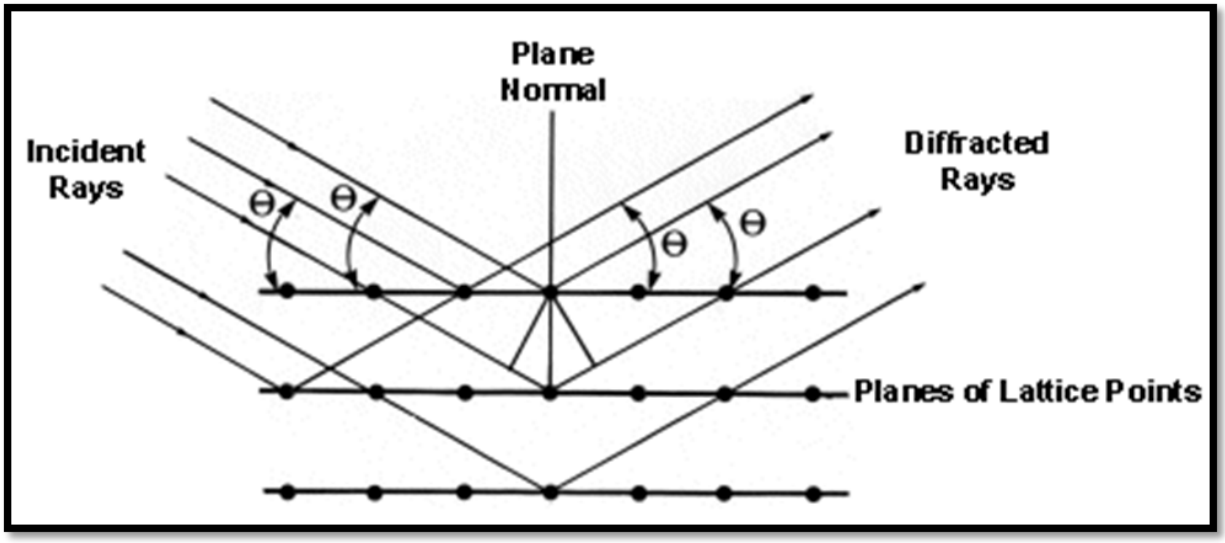

Figure 43. Figure showing the position for the incident and diffracted X-rays in XRD as well as the interaction angel of an ordered crystal

Scanning Electron Microscopy

Electron microscopy is a valuable tool for materials characterization because of the depth of information available in one tool. Modern scanning electron microscopes (SEM) can achieve magnifications exceeding 30,000X, which can allow visualization of particles in a massive 1cm to 50 nm range[2]. SEM's also have a high depth of field, allowing a wide area to be in focus at one time, and high resolution that allows information rich areas to be magnified. Generally speaking, scanning electron microscopy works by rastering the surface of interest with a beam of high energy electrons. The beam originates from a source called a gun and passes through a set of optics and coils designed to condense and focus the beam on the sample[2.] Once the electron beam impinges on the sample surface, a number of interactions take place that can be detected and an image produced. While high-energy electrons can pass through thin samples with little or no interaction, SEM analysis relies on the elastic or inelastically scattered electrons and radiation produced by inelastic scattering to produce the desired information. A schematic of the major components of an SEM is shown in Figure 44.

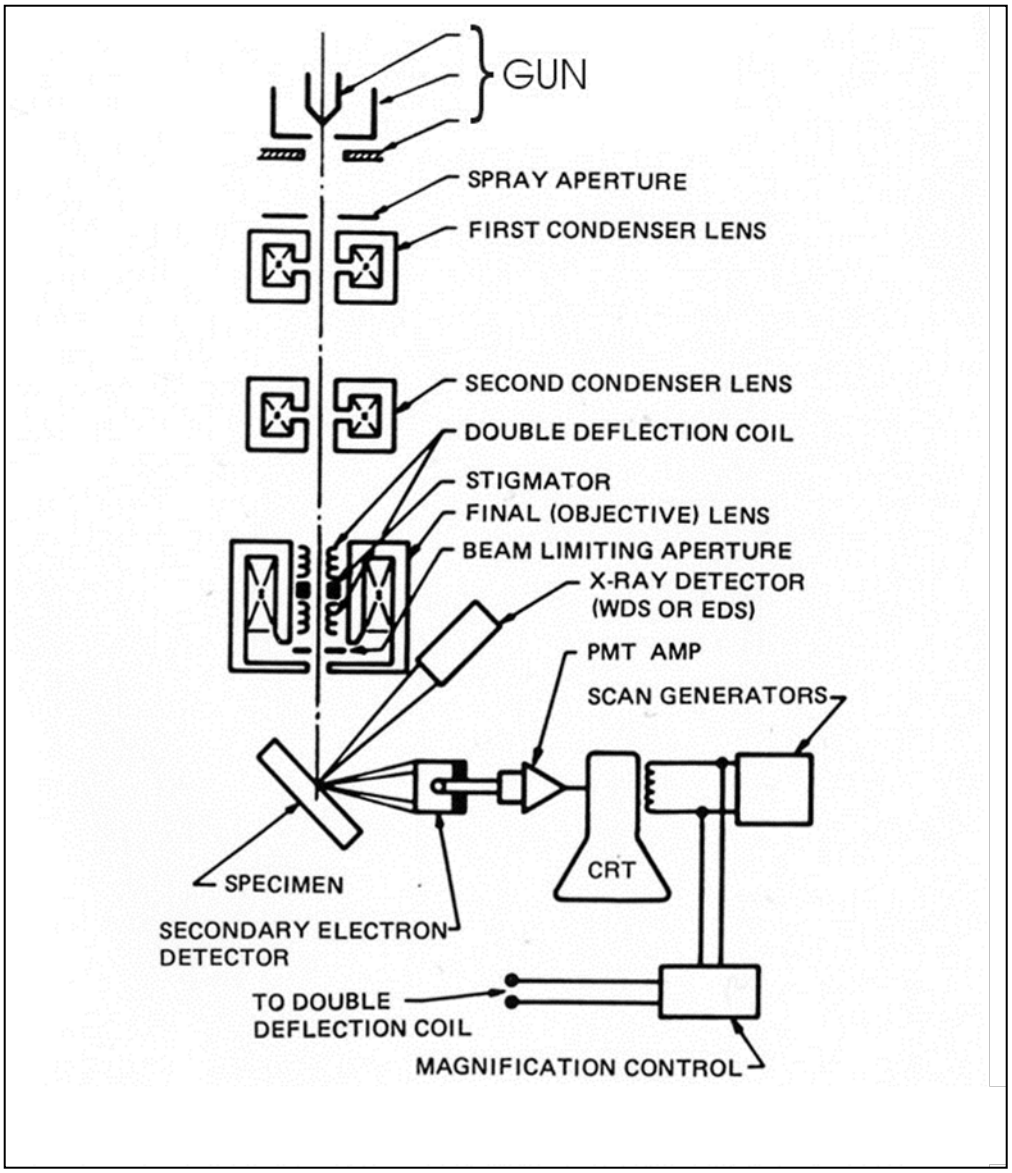

Figure 44. Schematic of a SEM's major components[76]

The interactions typically used in image creation can be seen in Figure 45. Bremsstrahlung X-rays are not specific but form an energy continuum from very low energy to the energy of the incident beam. This creates a characteristic background radiation that can mask some of the characteristic X-rays. The beam quality is dependent on the energy of the incident beam, the interaction volume in the sample and the orientation of the volume with respect to the incident beam. Asymmetry in the interaction volume will produce an askew image. To produce an image, each of the aforementioned interactions are detected independently and have specific resolution with Auger and secondary electrons producing the highest resolution followed by backscattered electrons, cathode luminescence, and lastly Bremsstrahlung.[2]

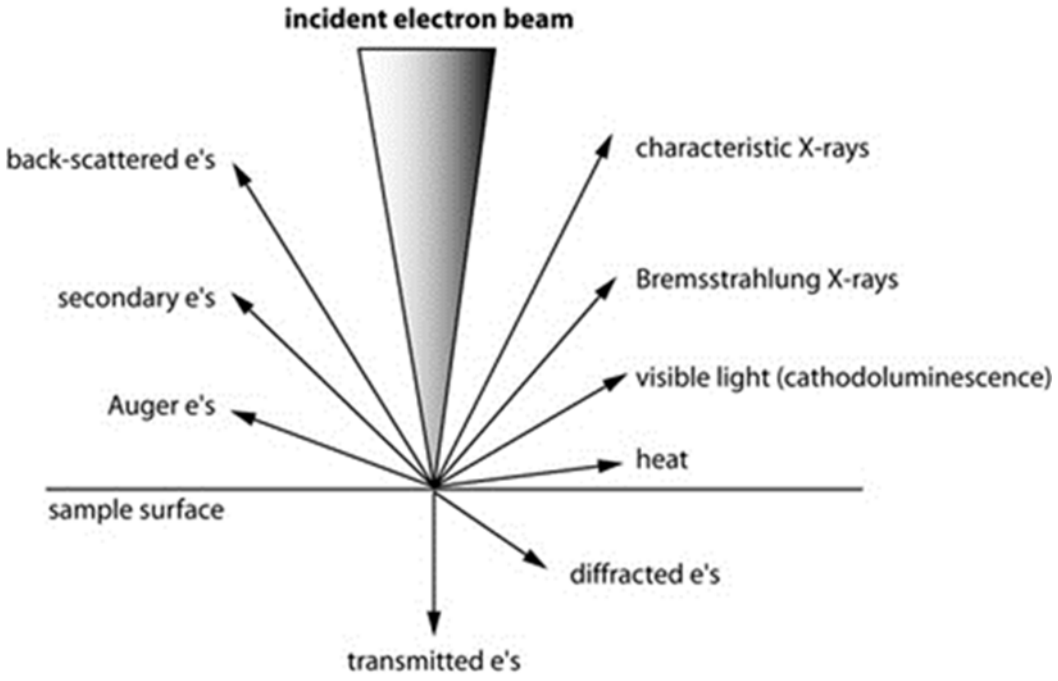

Figure 45. Cartoon depicting likely interaction from an electron beam in SEM[76]

Transmission Electron Microscopy

Transmission electron microscopy (TEM) is another powerful technique used for materials analysis. It is similar to SEM in that both techniques utilize electron beam to probe the sample. The primary difference of TEM is that the beam energy is not terminated on the sample surface, but rather passed through or transmitted to the sample. A series of complex magnetic (Figure 46) lenses direct the resultant energy relaxing processes and direct them to a centralized detector. TEM provides excellent spatial resolution, and this is one of the primary advantages of this technique. The high spatial resolution is achieved in TEM by the highly focused electron beam used to probe the sample. The wavelength of the incident electrons is exceedingly small and the beam is only directed at a micrometer spot on the sample. The result is a probing electron beam much smaller than other techniques including visible light or X-rays. With a smaller probe, the space between the atoms becomes much more apparent. High spatial resolution of TEM also comes about by only examining extremely thin samples. Typical sample thickness for TEM investigation is on the order of tens of angstroms to hundreds of nanometers. The thin samples reduce beam dilution thus retaining a more coherent probing beam. In addition to providing visual imaging at the nanometer scale, the focused electron beam of TEM can be used for a variety of scattering techniques that can provide more detail in terms of chemical composition and crystal quality.

EELS

Electron energy loss spectroscopy is a tool affixed to a high number of TEM's; it can provide chemical composition information interactions with the electron clouds of atoms. When the electron beam scans across an atom, it experiences elastic scattering with heavy species such as atomic nuclei and an inelastic process with the tightly bound inner shells or more loosely bound

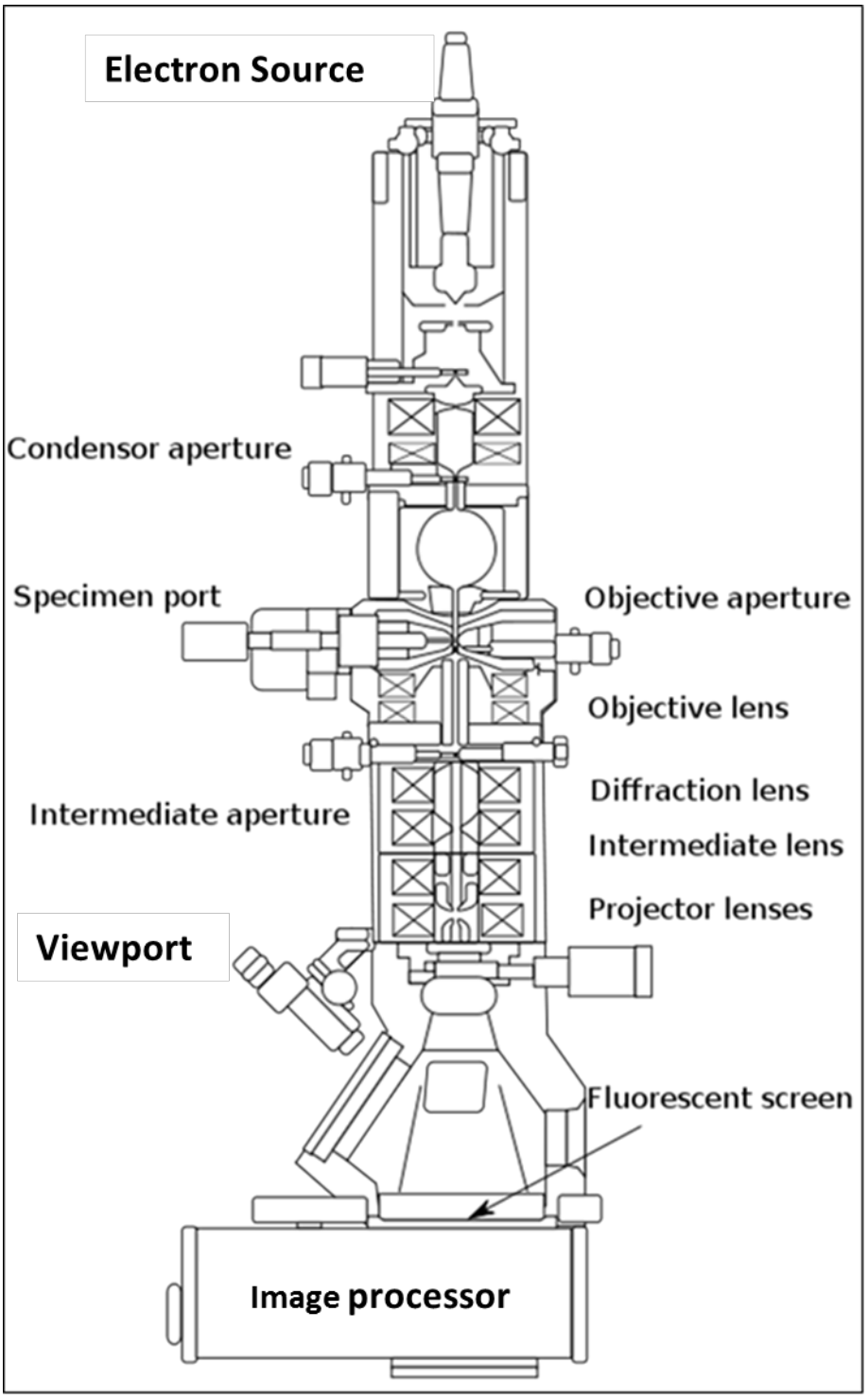

Figure 46. Schematic diagram of a typical TEM

Outer electron shells. The energy in these reactions is sufficient to promote the electrons to the next higher level or completely eject from the atom.

For clarification, consider the spectrum in Figure 47. Here electron intensity is graphed as a function of energy loss in units of electron volts. The tall peak at zero is appropriately named the zero loss peak and refers to the electrons that have not experienced a degradation in their original intensity as a result of an interaction. The region of the spectrum from 1 to 50 eV contains a series of broad lines that correspond to inelastic collisions with the valence electrons of the sample. In regions above this chemical composition can be determined as ionization on the inner shells. The vacancies created by the ionization correspond to the binding energy of the respective shell. The binding energies of the electrons is known, therefore the identity of the element can be deduced. In this manner EELS is similar to other techniques that rely on creation of vacancies like Auger electron spectroscopy (AES) and energy dispersive spectroscopy (EDS). Modern TEM is typically operated in two modes: diffraction and image. Image mode is self-explanatory; pictures of the sample characteristics are displayed on the screen. However, TEM operation in diffraction mode can be useful in determining crystal quality.

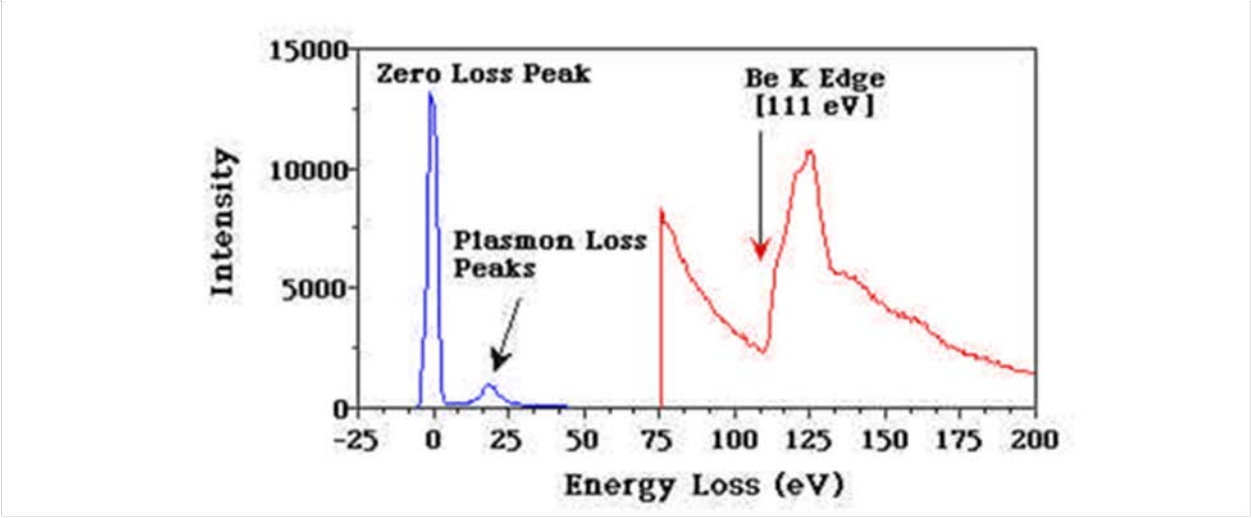

Figure 47. Sample EELS spectrum of Be depicting low and high loss regions

Selected Area Diffraction

By realigning the objective lenses post sample and defocusing them to produce illumination at the sample, a series of spots is created on the screen. This pattern of spots is referred to as the selected area diffraction (SAD) pattern and is representative of the primary electron beam interacting with crystallites in the small area of interest. Image 48 shows a SAD pattern from a BP sample. The SAD pattern depicts the interface of the BP with the SiC substrate. Analyzing the alignment of the spots indicates the crystalline nature of the sample. In this case the BP diffraction pattern overlaps the SiC diffraction pattern indicating an epitaxial relationship. SAD is also used to determine Bravais lattice and lattice parameters of crystalline systems.

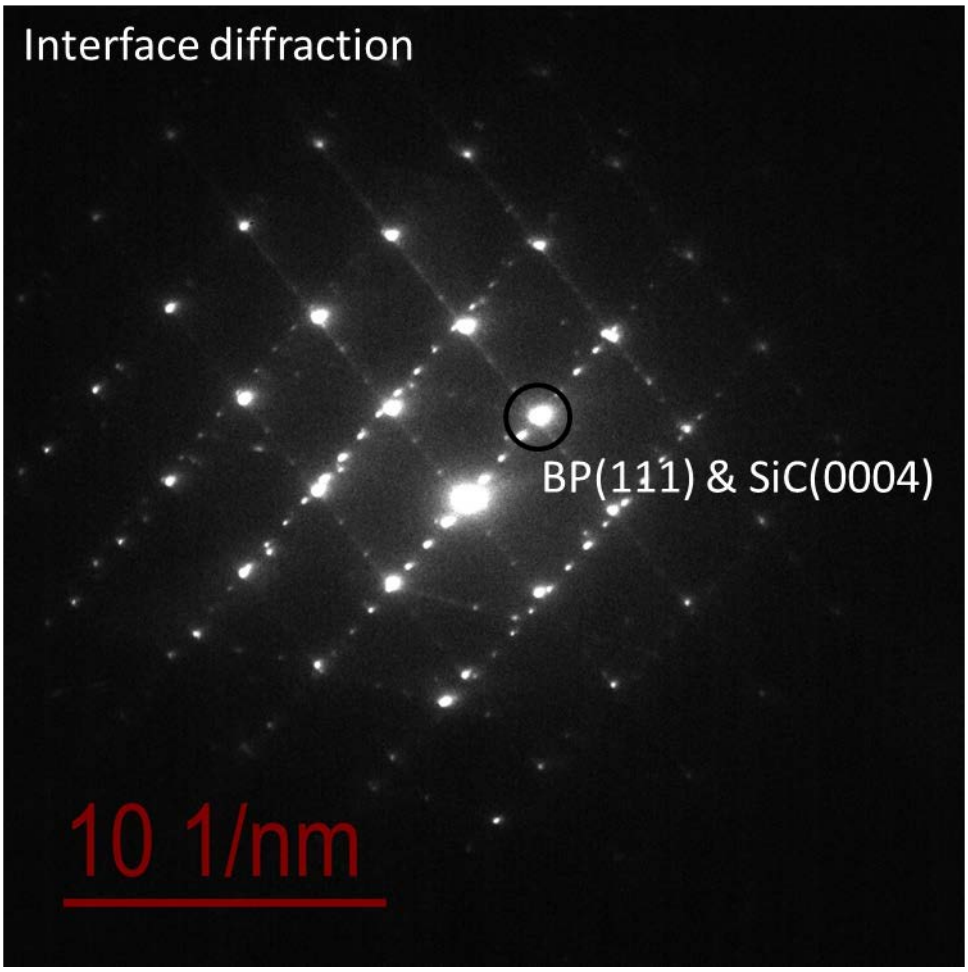

Figure 48. SAD diffraction pattern of BP on SIC. Showing epitaxial relationship

Summary

A systematic approach was used to address the numerous areas required for custom CVD reactor design. Topics including gas flow, purity, process automation, material compatibility and safety were individually approached in a series of efforts to develop a working system. A series of systematic function tests were performed with surrogate gases to ensure all systems were operating as designed. Characterization techniques applicable to BP thin film analysis were presented and discussed. Overall, experiments have proven that the reactor design presented here is successful. Further advances in reactor design will be driven by analysis of BP deposition.

CHAPTER III
DEPOSITION OF BORON PHOSPHIDE ON SILICON SUBSTRATES

Silicon Experiments

Experiment 1

Experiments were conducted to establish the CVD reactor's ability to grow boron phosphide on silicon substrates. As previously described, the bulk of the prior BP work present in the literature has been conducted on Si. Therefore growths on Si can provide a direct comparison of depositions in this reactor with previously published work. It is worth noting that starting with the first attempt at BP deposition, a continuous film was obtained.

Experiment one was intended to verify the operation of the reactor by emulating Kumashiro's previously published parameter settings established by his work on Si. Silicon substrates (0.75" x 0.75" in intitial experiments) were wet chemically etched to remove native oxides using the procedure described in appendix B prior to insertion in the reactor. Substrates were placed on the graphite susceptor and correctly positioned in the reactor. The reactor was evacuated to $<10^{-5}$ Torr before starting a CVD growth sequence, which begins with in situ hydrogen etch. The hydrogen etch procedure is described in detail in appendix B, but consisted of heating the sample to 1000 °C in a hydrogen atmosphere. The duration of the hydrogen etch is typically 20 minutes. In early attempts when a 10 minute hydrogen etch was used , post deposition analysis of these samples showed the presence of an oxide on the substrate surface. Doubling the etch time eliminated the surface oxide and all future samples were etched for 20 minutes. At the end of the hydrogen etching period, the susceptor and substrate were cooled to the desired deposition

temperature. Once the deposition temperature was reached, phosphine and diborane were added to the flow which begins the CVD reaction. At the end of the reaction period, flow of phosphine and diborane is halted and the sample is cooled in a hydrogen flow.

The flow rates of 1% diborane and 5% phosphine and balance hydrogen gas were 20 sccm, 300 sccm and 2500 sccm respectively. A system pressure of 630 torr was used for the initial experiment as well as most subsequent experiments. The substrate temperature used in this experiment was 786° C and the reaction duration was 90 minutes. A photograph of the resultant sample is given in Figure 49. The film exhibits a non-uniform coloration, indicating varying coverage of the substrate or a substantial thickness gradient. Optical microscopy images of sample 1 shown in Figure 50 indicate a continuous film is formed but this technique does not have sufficient magnification to fully characterize coverage. SEM images of sample 1 are more informative. Surface SEM images (Figure 51) depict the film as having a rough texture with islands of large particles dispersed throughout. Cross sectional SEM of sample 1 shown in Figures 52 and 53 confirm a significant thickness gradient in the film. Following the direction of gas flow, the thickness drops from ~8000nm at the front of the sample to 5739 nm near the back. The thickness varies less in the direction perpendicular to the flow, reaching a peak near the middle and dropping off slightly toward each edge. This thickness distribution is consistent with a depletion of growth species as the gas flow moves across the sample.

Raman spectroscopy was performed on sample 1 for comparison to published literature values. The Raman spectrum of BP, shown in Figure 54, consists of a single phonon mode peak and a weaker overtone. The Raman spectrum for sample 1 exhibited a strong peak at 822 cm^{-1},

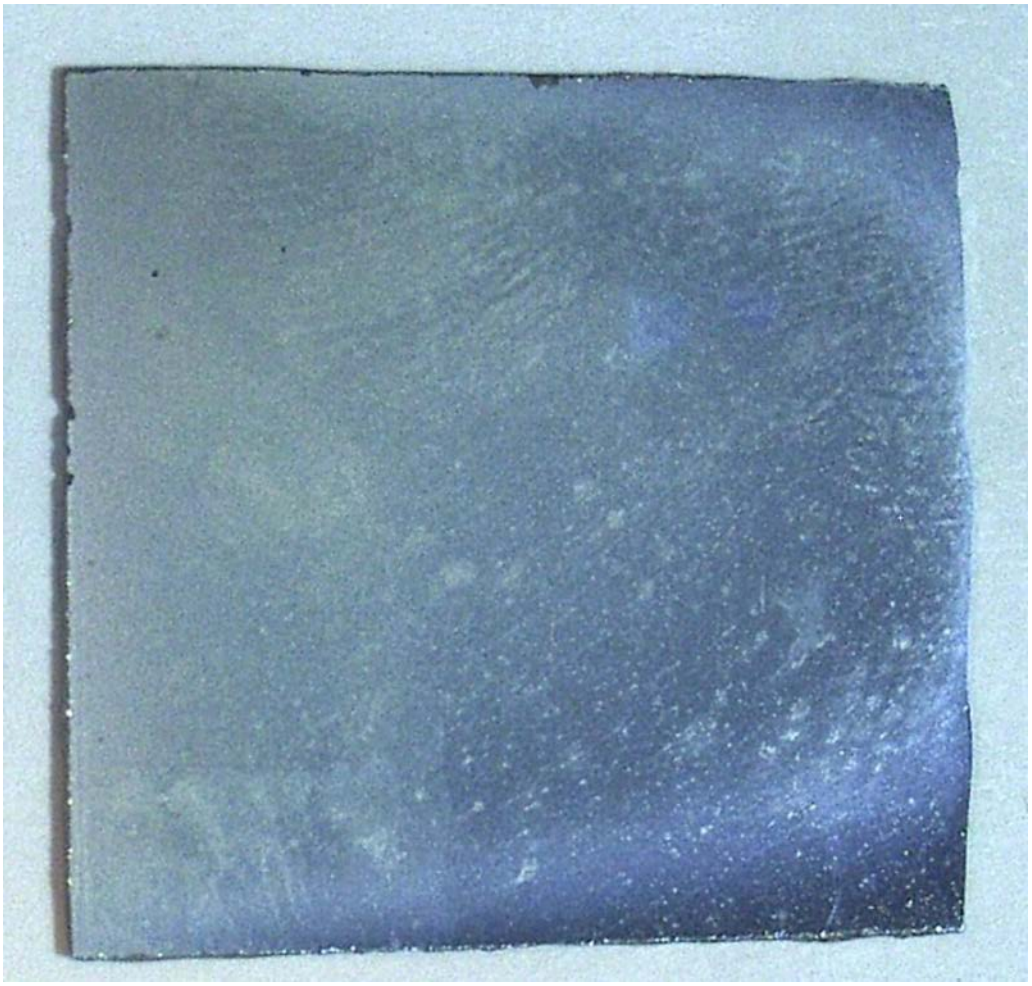

Figure 49. Photograph of Sample 1 immediately following deposition. Note the non-uniform deposition evidenced by the varying coloration in the film

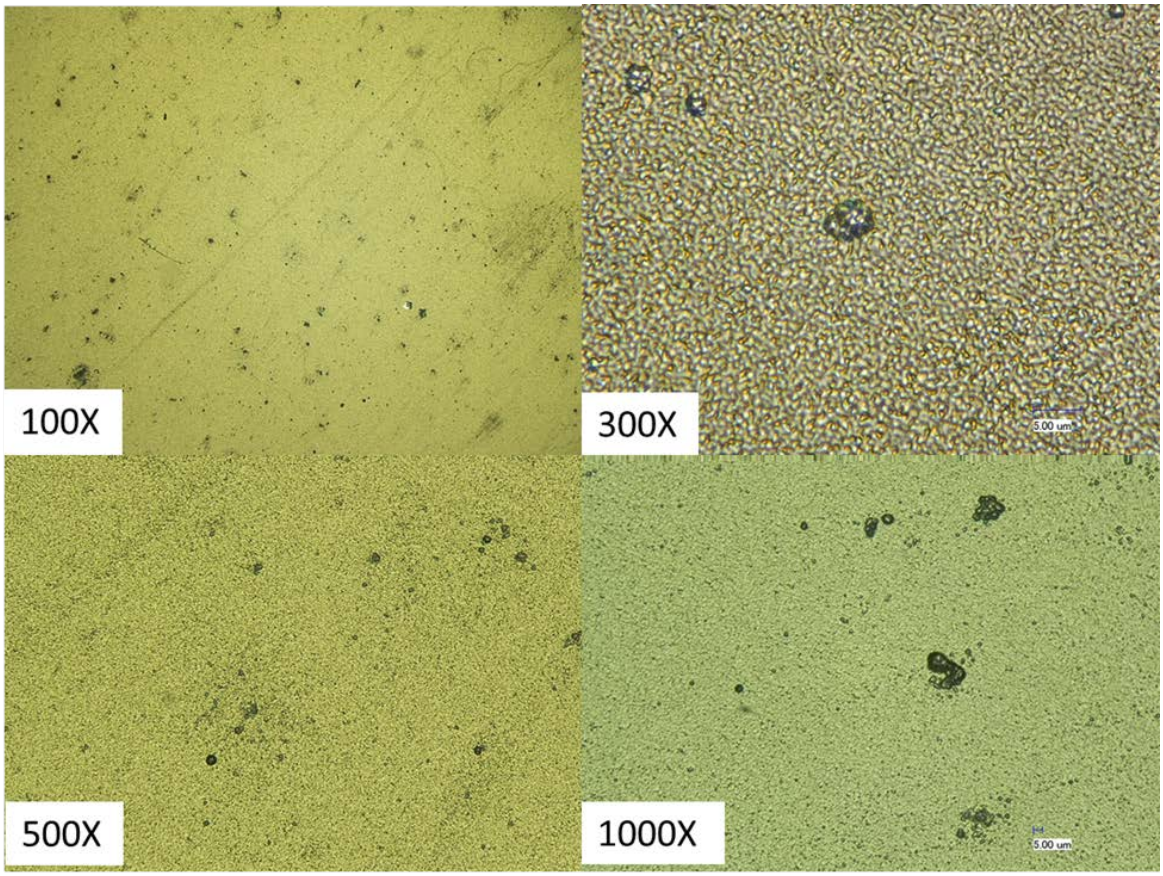

Figure 50. Optical Microscope images of Sample 1 at 100 X magnification to 1000 X magnification

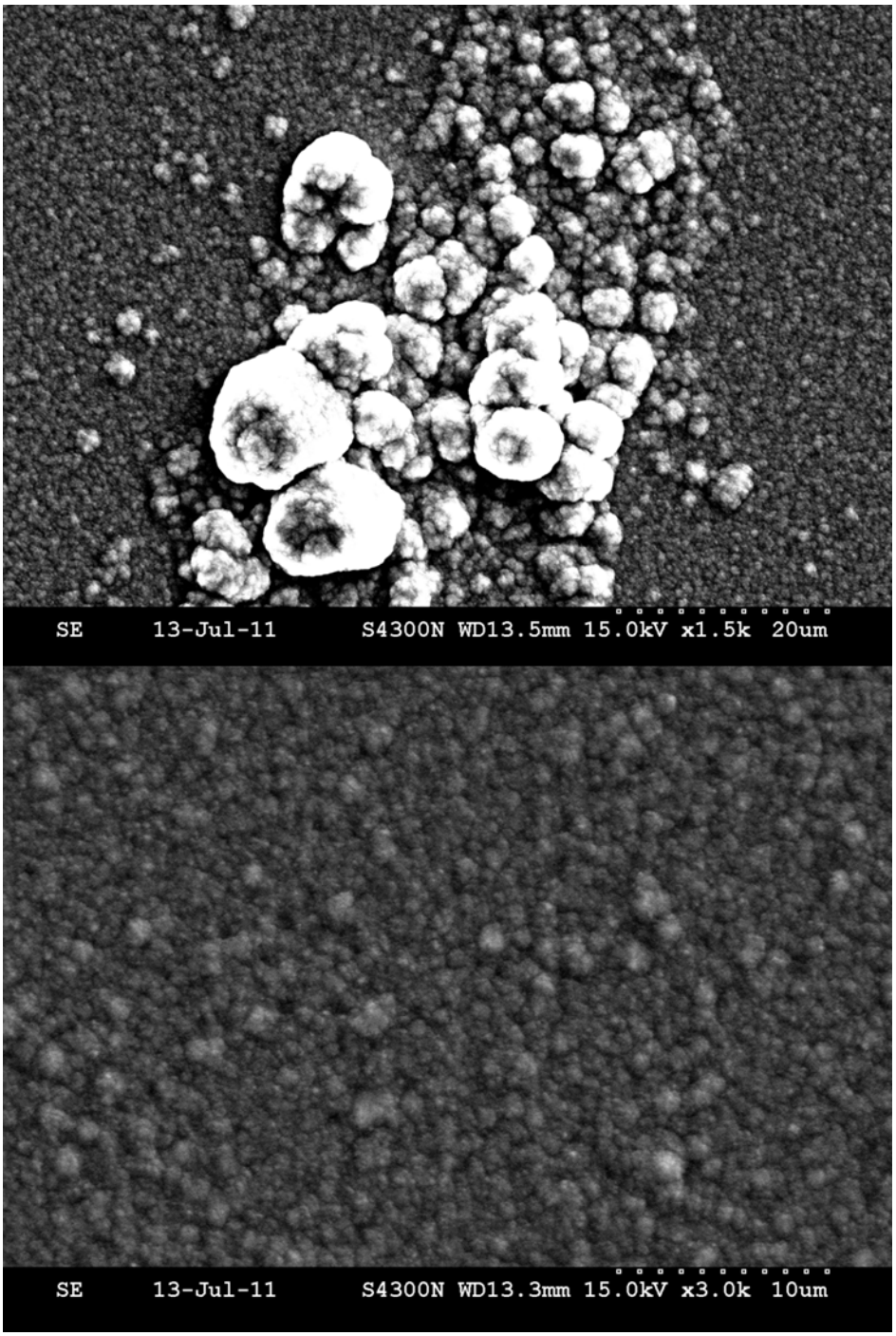

Figure 51. SEM image of BP sample 1. Showing BP particle cluster (top) and rough surface (bottom)

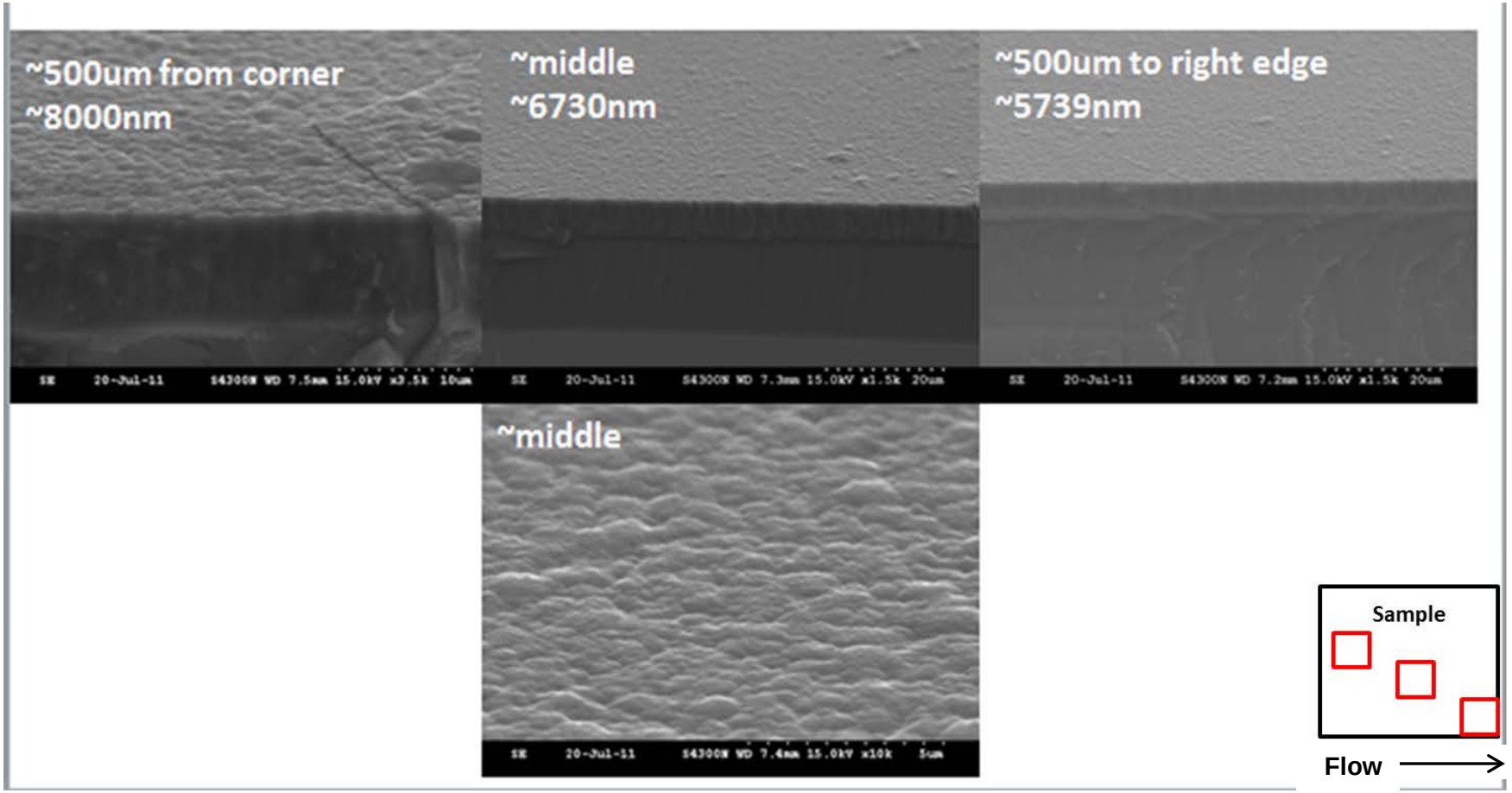

Figure 52. Cross section SEM of BP sample 1. Red squares indicate approximate location of corresponding image

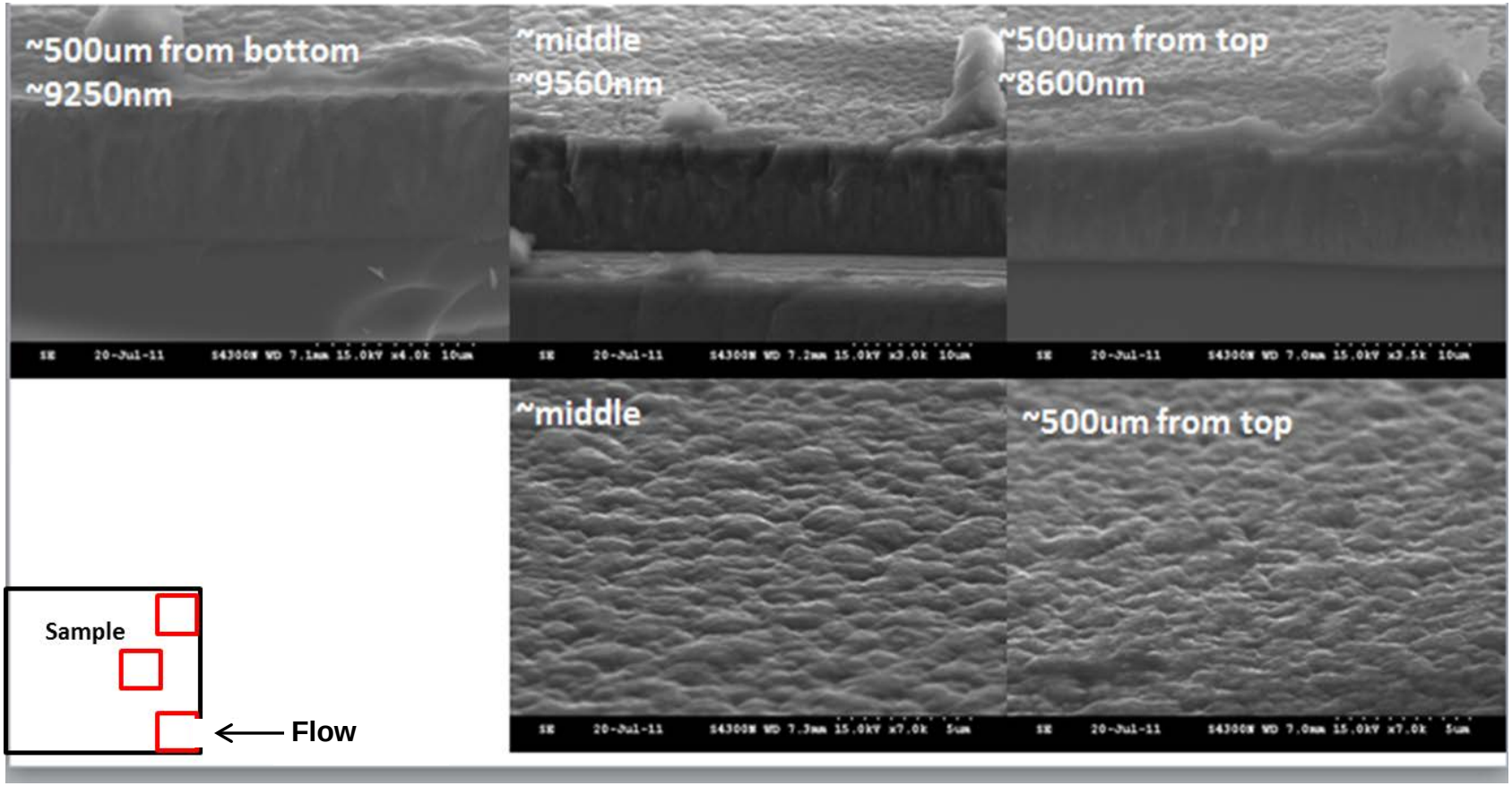

Figure 53. Additional cross sectional SEM images of sample 1. Samples taken 90 degrees off from those shown in figure 8

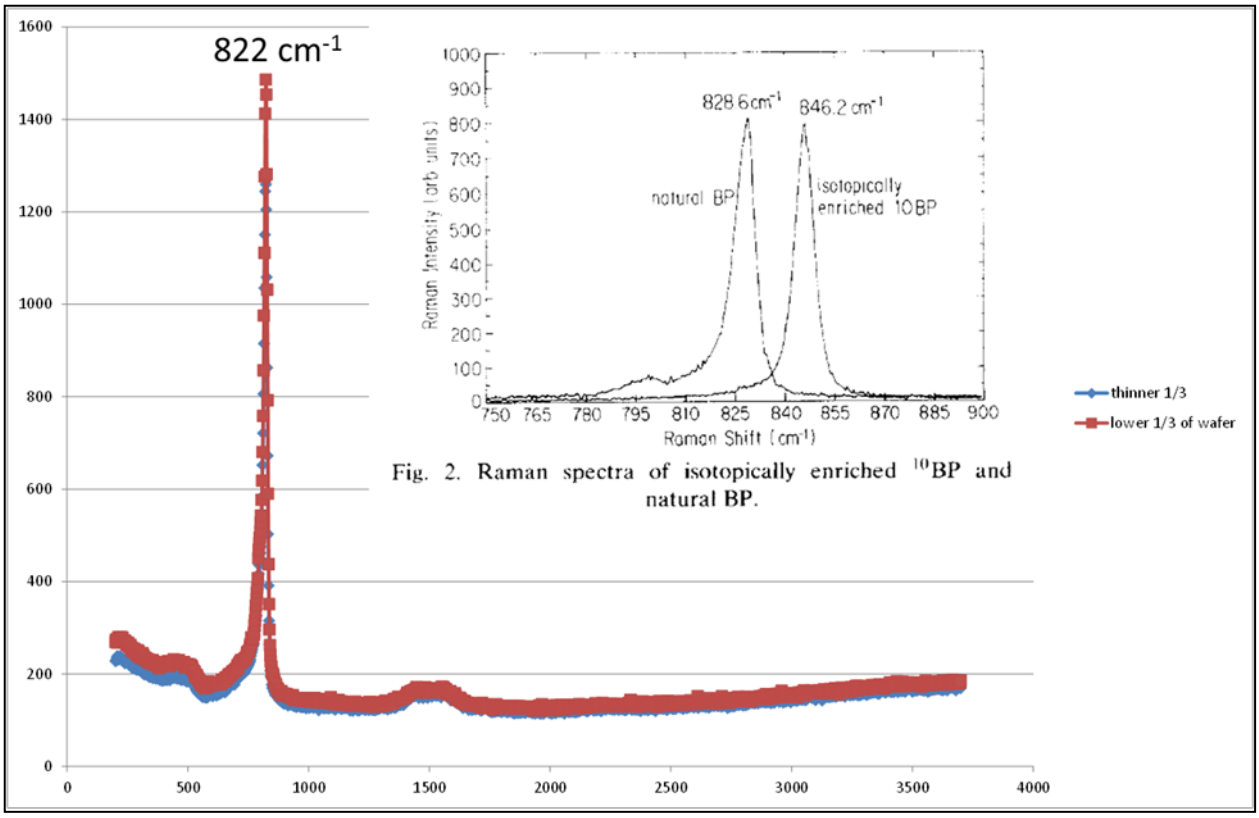

Fig. 2. Raman spectra of isotopically enriched ^{10}BP and natural BP.

Figure 54. Graph of Raman spectrum on Sample 1. Note inlay of literature values. Published Raman spectrum peak is 828 cm^{-1}. measured valued of sample 1 is 822 cm^{-1}

whereas the phonon peak for BP containing natural abundance boron has been reported at 828 cm-1.[42] Differences in calibration and stresses in the film could account for this shift.

Parametric Analysis Samples 1-20

A total of 30 experiments were performed on Si substrates. Table 4 shows the experimental parameters used during growths of the first 20 samples including system pressure, temperature of the graphite susceptor measured by disappearing filament optical pyrometer, gas flows of the H_2, PH_3 and B_2H_6 process gases, respectively, as established by the mass flow controllers. the system, the time of run, which is the duration of deposition and does not include time for substrate preparation or cool down, and the substrate material used in the experiment. Mass gain is the difference between the average of three sequential weighings of the sample before and after growth. The average film thickness is the thickness expected for a uniform film based on the mass gain and density of BP.

Table 4. Layout of selected sample parameters for samples 1-20

Sample #	1	2	3	4	5	6	7	8	9	10	11	12	13	14	15	16	17	18	19	20
Pressure (torr)	630	630	630	650	650	650	630	630	630	630	630	630	630	630	630	630	315	315	630	150
Temp (°C)	810	>743	798	840	800	915	816	830	815	815	820	800	806	825	854	845	803	811	813	800
H_2 (sccm)	2500	2500	1250	1250	2500	2500	2500	2500	2500	2500	2500	2500	2500	2500	2500	2500	2500	1250	2500	1000
PH_3 (sccm)	300	300	150	150	300	300	300	300	300	300	300	300	300	300	300	300	300	150	300	100
B_2H_6 (sccm)	20	30	30	15	30	30	30	30	30	30	50	60	60	30	30	30	30	15	30	10
Time of run (hrs)	1.5	2	0.5	2.25	2.25	2	2	2	2	2	2	2	2	2	0.5	0.5	0.5	0.5	0.5	0.5
Predicted film thickness (μm)	N/A	11.8	0	1.14	4.10	0.32	7.06	4.26	7.38	2.41	10.97	14.00	16.83	9.45	2.85	2.47	4.15	1.56	2.62	0.
mass gain (mg)	?	14.4	0	1.4	5	0.4	8.6	5.2	9	2.94	13.37	17.06	20.51	11.5	3.48	3.02	5.06	1.9	3.2	0.9
Substrate	Si	Si	Si	Si	Si	Si	Si	Si	Si	Si	Si	Si	Si	4H-SiC-4° off axis	4H-SiC-4° off axis	4H-SiC-4° off axis	Si	Si	4H-SiC-4° off axis	Si
mass gain (mg)/hr	N/A	7.2	0	0.62	2.22	0.2	4.3	2.6	4.5	1.47	6.685	8.53	10.25	5.76	6.96	6.04	10.1	3.8	6.4	1.8

Average film thickness is calculated from the following formula:

Average film thickness (μm) = mass of film (g) / [wafer area (cm^2)] x [density of BP (g/cm^3)]

The last row in Table 4 is labeled PH_3/B_2H_6. This row lists the flow rate ratio of the BP precursors. This is calculated by dividing the respective flow rates reported in the PH_3 and B_2H_6 rows of the table. The flow rate ratio is a convenient parameter for linking changes in the relative proportion of PH_3 and B_2H_6 gas flow rates and the resultant film.

BP thin films grown and characterized in samples 2- 20, were primarily used to develop an understanding of the behavior of the CVD reactor and establish confidence and reliability metrics for future experiments. Successful depositions were achieved in this sample set and a brief discussion will be provided here. Raman spectra were obtained for all but one sample in the data set. An overlay of the Raman spectra of these samples given in Figure 55 show a predominate peak at 823 cm^{-1} and an overtone around 1500 $cm^{-1.}$ The spectra are all consistent with BP growth. It is worth noting that samples 5-10, 14-16 and 19 were all grown using the same gas flows. A minor variation is noted in deposition pressure, which varied from 630 to 650 Torr for a couple of samples. Deposition temperature varied the most with the outlier of sample 6 at 915 °C; however, the remainder of the growths was carried out between 800-850 °C. Given these conditions, some notable observations can be made. For example, growth rates in samples 5-10 vary significantly despite the similar experimental conditions. This is most likely due to ongoing process refinement and conditioning of the system. This variability was not observed in later samples grown under similar conditions. In contrast, samples 14-16 and 19, which are all growths on 4H SiC, show very similar growth rates indicating that some measure of reproducibility has been achieved. In general, greater variability in growth rates is observed with early growths on silicon substrates, at times varying by as much as a factor of 2 for nearly identical growth parameters.

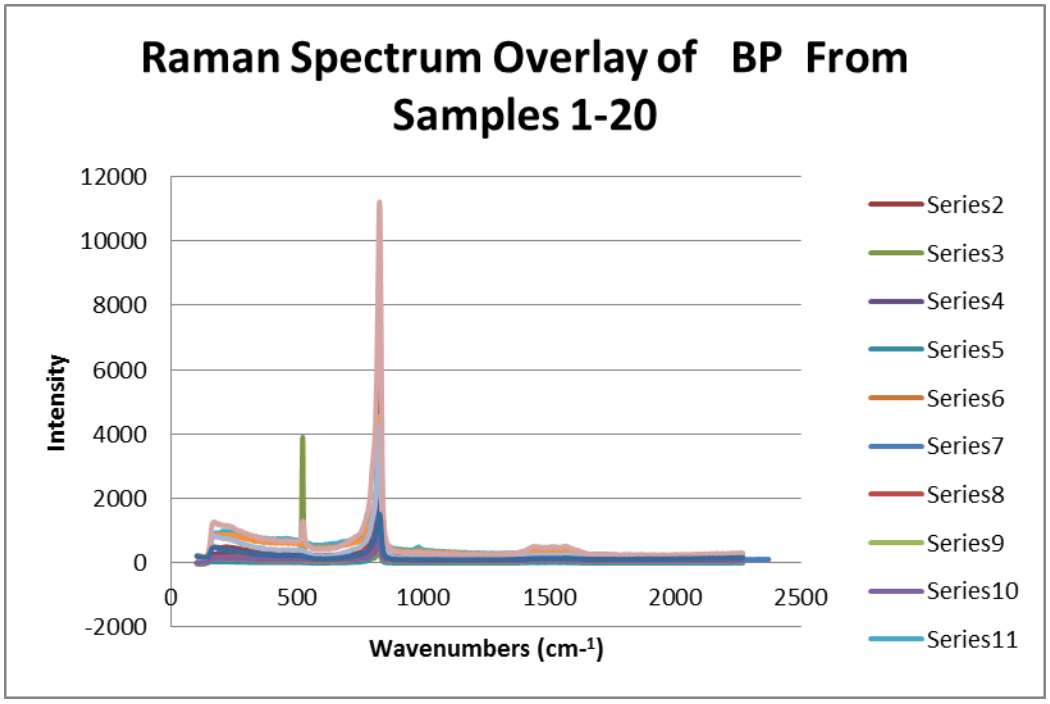

Figure 55. Raman Spectra. Overlay of Samples 1-20

In spite of the variability of growth rates on silicon in these first 20 samples, certain trends do seem to emerge. Increasing the diborane flows increases the growth rate as seen by comparing samples 11-13 to sample 5-10. The effect of varying flow rates and flow rate proportions will be investigated further in samples 21-27. These early samples also suggest that small changes in deposition temperature in the range of 800-850 °C have little effect on the growth rate at constant pressure. There are also indications that lowering the total pressure increases the growth rate. Comparing sample 17 with samples 5, 7-9, show a more than doubling of the growth rate with a 50% reduction in pressure. The exact cause of this is not clear at this time, but one possible cause is by lowering the system pressure, there is less thermal transfer and therefore less gas phase nucleation. This would allow more diborane to be available for deposition rather than being reacted and pumped away. Since diborane appears to be the limiting reagent in the reaction as suggested by this data set; conversely, lowering diborane flow rate generally corresponds with lower growth rates, and having more diborane is consistent with higher growth rates.

Samples 21-27

Samples 21-27 were grown taking care to establish that good reproducibility in growth rate was achieved for identical growth conditions and to probe the effects of changing growth parameters on growth rates and film quality. Table 5 lists the experimental parameters for this data set. Prior to presenting individual samples, a brief discussion on general observations is needed to clarify conclusions later in this chapter and will be presented here. Unlike some of the early samples where growth rates varied widely, this data set has remarkable consistency. System pressure and

Table 5. Table of experimental parameter settings for samples 21-27

Sample #	21	22	23	24	25	26	27
Pressure (torr)	630	630	630	630	630	630	630
Temp (°C)	800	803	805	805	798	811	855
H_2 (sccm)	2500	2500	2500	2500	2500	2500	2500
PH_3 (sccm)	100	300	100	300	300	150	300
B_2H_6 (sccm)	10	30	10	30	10	30	30
Time of run (min)	0.5	0.5	0.5	0.5	0.5	0.5	0.5
Predicted film thickness (µm)	1.018	2.718	0.961	2.668	0.846	2.660	2.537
mass change (mg)	1.24	3.31	1.17	3.25	1.03	3.24	3.09
Substrate material	Si	Si	Si	Si	Si	Si	Si
ave. thickness (µm)	1.2	3	1.3	3	1	3.2	2.7
Growth Rate/hr	2.4	6	2.6	6	2	6.4	5.4
PH_3/B_2H_6	10	10	10	10	30	5	10

temperature settings are mostly unchanged with the exception of sample 27 that was performed at 855 °C. Phosphine and diborane flow rates were varied allowing further conclusions to be made about the role each of the precursors play in BP deposition. Generally, when the phosphine and diborane flow rates is reduced by 1/3 a corresponding reduction in growth rate ensues. This is clear from comparing samples 21 and 22 with 23 and 24. In sample 21 and 23, the precursor flow rates are 100 sccm and 10 sccm for phosphine and diborane respectively. Sample 22 and 24 were grown at higher flow rates of 300 sccm and 30 sccm. Samples 21 and 23 exhibit approximately 1/3 the mass gain, average thickness and growth rate compared to samples 22 and 24. Thus reducing both gases corresponds to a similar reduction in the amount of material deposited. Varying just one of the precursors with respect to the other yields a different result. Consider samples 22 and 25, in these experiments, the phosphine flow is held constant at 300 sccm, but the diborane differ by 1/3, 10 sccm in sample 25 and 30 sccm in sample 22. The result is a growth rate 2 mg/hr, for sample 25, which is 1/3 of the rate obtained for sample 22 which was 6 mg/hr. Akin to observations in the previous data set, lowering the diborane flow directly affects the amount of BP grown. The same is not true for phosphine. Comparing samples 21 and 25 show that reducing the phosphine by 1/3 and holding the diborane constant does not affect the growth rate. Sample 21 had a growth rate of 2.4 mg/hr whereas sample 25 had a growth rate of 2 mg/hr. Combined, these results for samples 21-25 establish that the diborane concentration limits the reaction rate, supporting earlier conclusions by Kumashiro et al.

Although most of these samples were performed at temperatures close enough to be considered identical, one sample temperature was varied to explore temperature effects. A more thorough study of the effect of temperature will be given in the next chapter on growths on SiC. Sample 27 was grown at identical pressure and flow rates as sample 22 and 24, but at ~ 50 degrees higher temperature. This increase in temperature has a marginal impact on film growth rates. Sample 27 recorded a growth rate of 5.4 mg/hr where samples 22 and 24 both recorded growth rates of 6

mg/hr. The difference of 0.6mg/hr corresponds to an expected thickness of 300 nanometers or 10% of the total growth for samples 22 and 24.

Overall, data sets 21-27 demonstrate good reproducibility. Furthermore, all samples in this data set had the presence of BP confirmed by Raman Spectroscopy and XRD analysis. Figure 56 shows an overlay of the Raman spectra acquired for these samples and Figure 57 shows a collection of XRD spectra showing the two distinct peaks consistent with BP.

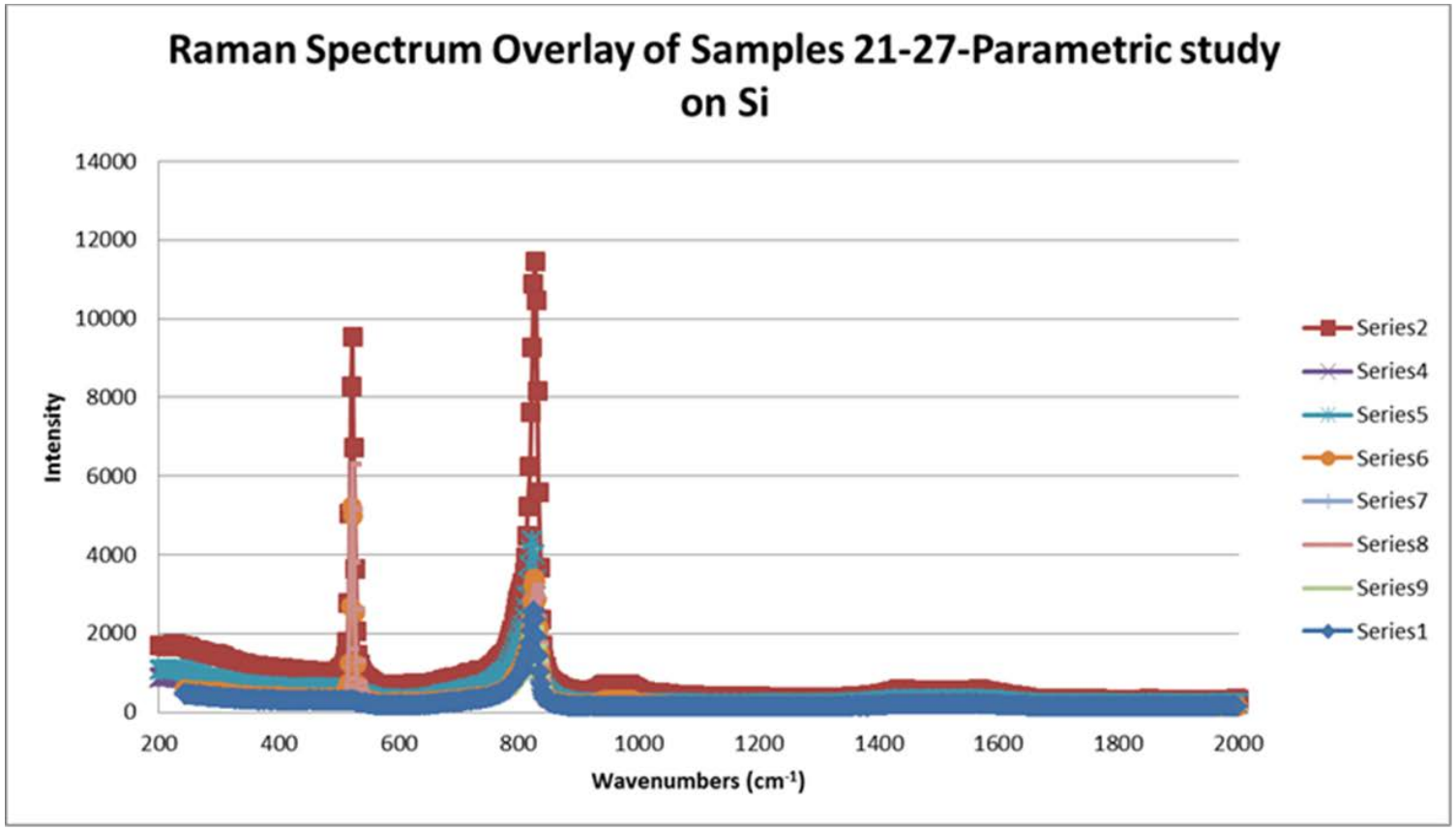

Figure 56. Overlay of Raman Spectra for samples 21-27. BP peak appears at 828 cm^{-1}. The 522 cm^{-1} peak is consistent with Si

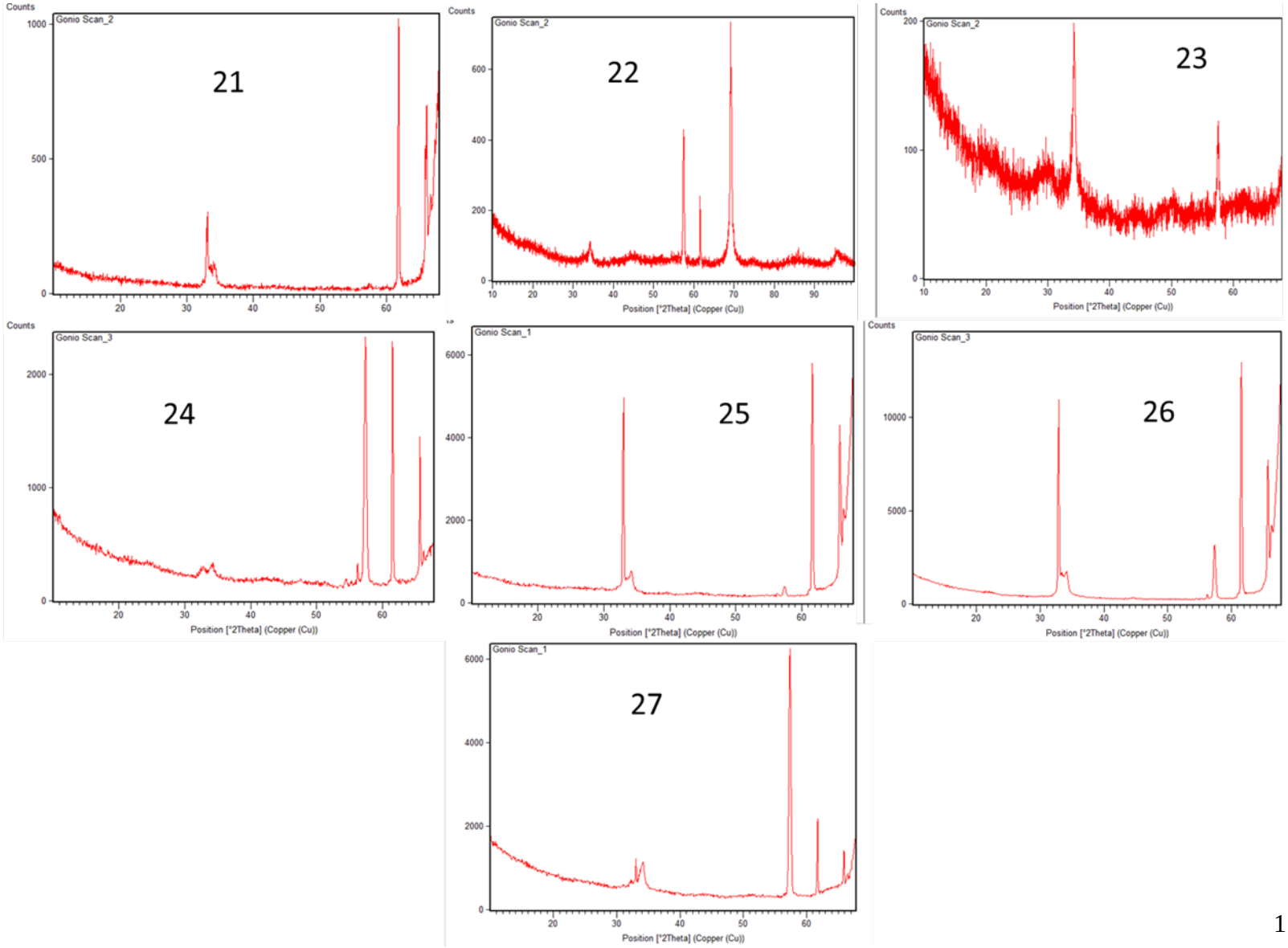

Figure 57. Collection of XRD spectra of samples 21-27 showing peaks consistent with BP

Sample 21

Sample 21 is the first sample in a series of experiments to explore the effect of varying precursor flow rates on the growth and morphology of BP on Si substrates using the as built reactor. Experimental run conditions were as follows; system pressure was 630 torr, temperature of the susceptor was measured at 800 °C, hydrogen flow rate was set to 2500 sccm, phosphine flow rate was 100 sccm, diborane flow was set at 10 sccm and the run time was 0.5 hours. An important note on strategy is the run time is significantly reduced here because the focus of the experiments has changed. Experiments designed to elucidate reactor function were conducted at the bulk scale. These experiments, designed to determine optimum morphology on Si, were focused on the substrate-film interface. Run time was subsequently reduced in order to allow for easier sample preparation for electron microscopic analysis. Results of the experiment on sample 21 showed a mass gain of 1.24 mg with a predicted film thickness of 1.02 μm. Additionally, the phosphine-diborane flow rate ratio was 10. A photograph of the casual observation immediate following deposition can be seen in Figure 58. Note, all photos post deposition are shown with the gas flow direction proceeding from right to left. Blue fringes can be seen on the top of the sample indicating variations in film thickness. Optical microscopy was not performed on these samples because they provide little useful information on film morphology. In lieu of optical microscopy, SEM and cross-sectional SEM microscopy was performed on the sample. Figure 59 shows a 5000X imagination of the surface of the BP thin film. This image is taken distal to the flow orientation. A diagram showing image location on the sample is also shown in Figure 59 in the lower right corner. The red square indicates the area where the corresponding image is taken. BP particles are seen, but a continuous

Figure 58. Photograph of sample 21 post deposition.

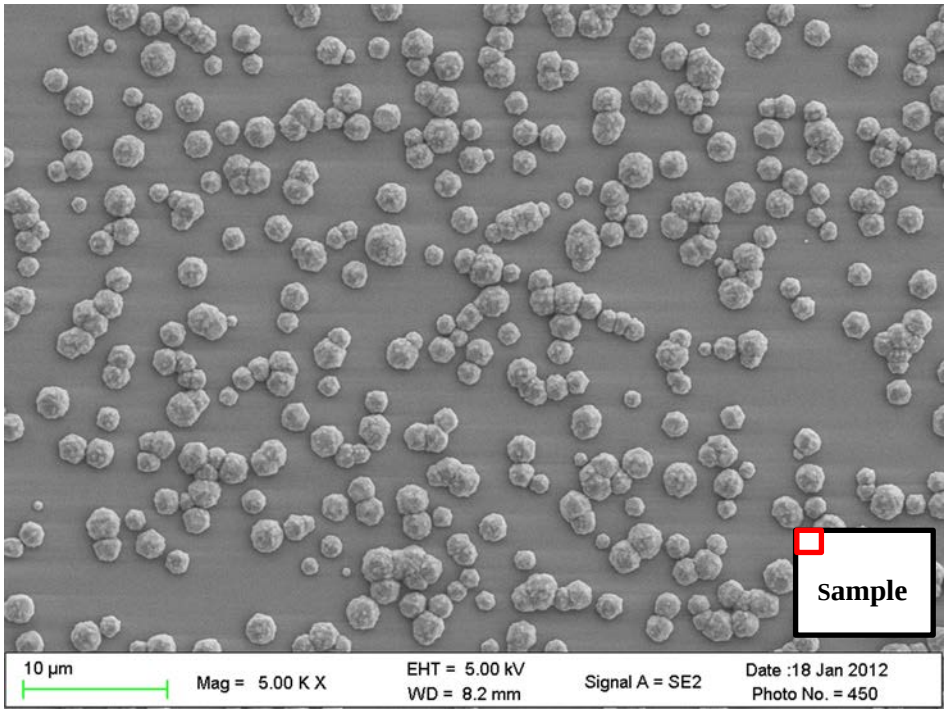

Figure 59. SEM image of sample 21, Si substrate surface. Showing BP particles dispersed on substrate

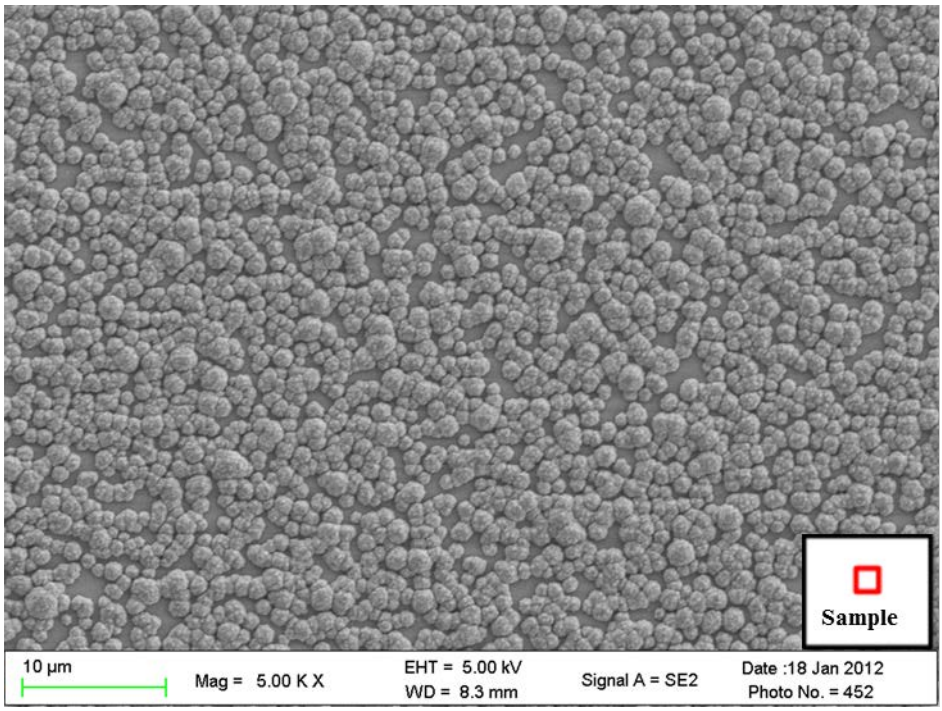

Figure 60. SEM micrograph of sample 21, showing BP particles with increasing density. Sample taken from middle of wafer with flow direction from right to left

film is not observed. The distance between particle grouping ranges from 0 to approximately 12 microns. Towards the center of the sample, as shown in the coverage is much denser (Figure 60). The distance between particle groups is less than one micron. A SEM image of an area of the substrate nearest to the gas flow is given in Figure 61 and shows a rough continuous thin film at the higher magnification of 10,000X. While each image considered individually only represents the spot coverage in those particular areas, the images collectively indicate that wafer coverage varies as function of distance from the gas flow. Furthermore, the Volmer–Weber growth mode is suggested where a thin-film does not form a monolayer on the substrate surface due to adatom-adatom interactions being preferred over adatom-surface interactions. Islands of growth are formed initially and as growth progresses, the islands begin to coalesce forming a continuous film. Cross sectional SEM images of the right edge of sample 21 at 30kX (Figure 62) and 60kX (Figure 63) show the thickness of the resultant film at the front of the flow and columnar growth is indicated from the long veins perpendicular to the interface.

Raman spectroscopy is used in these experiments to confirm growth of BP. Raman spectra measured for these samples (21-27) consistently exhibited a BP peak near 828 cm-1. The additional peak appearing at approximately 521 cm-1 is the phonon peak from the Si substrate.

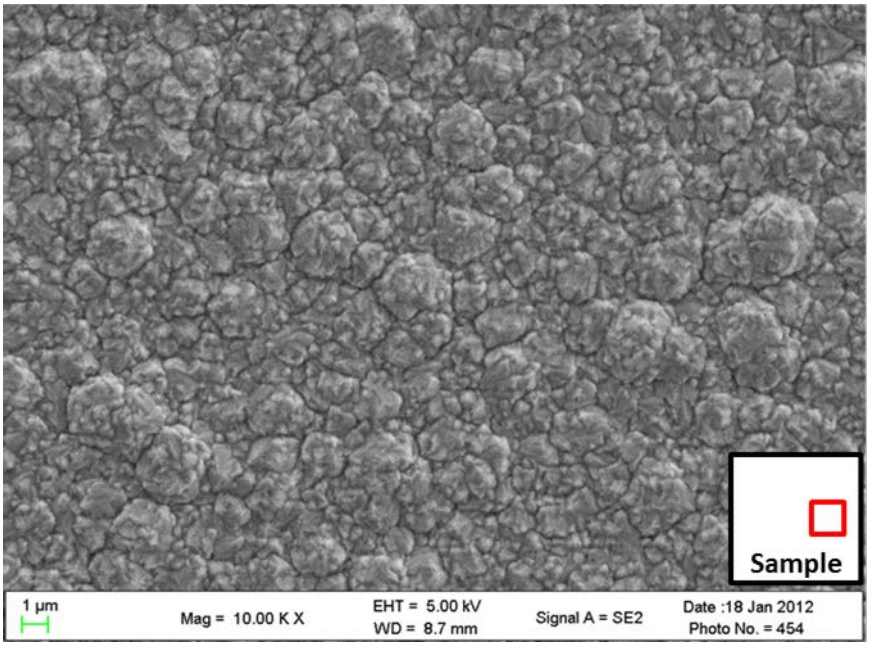

Figure 61. SEM micrograph of sample 21, showing BP particles with increasing density. Sample taken from middle of wafer with flow direction from right to left

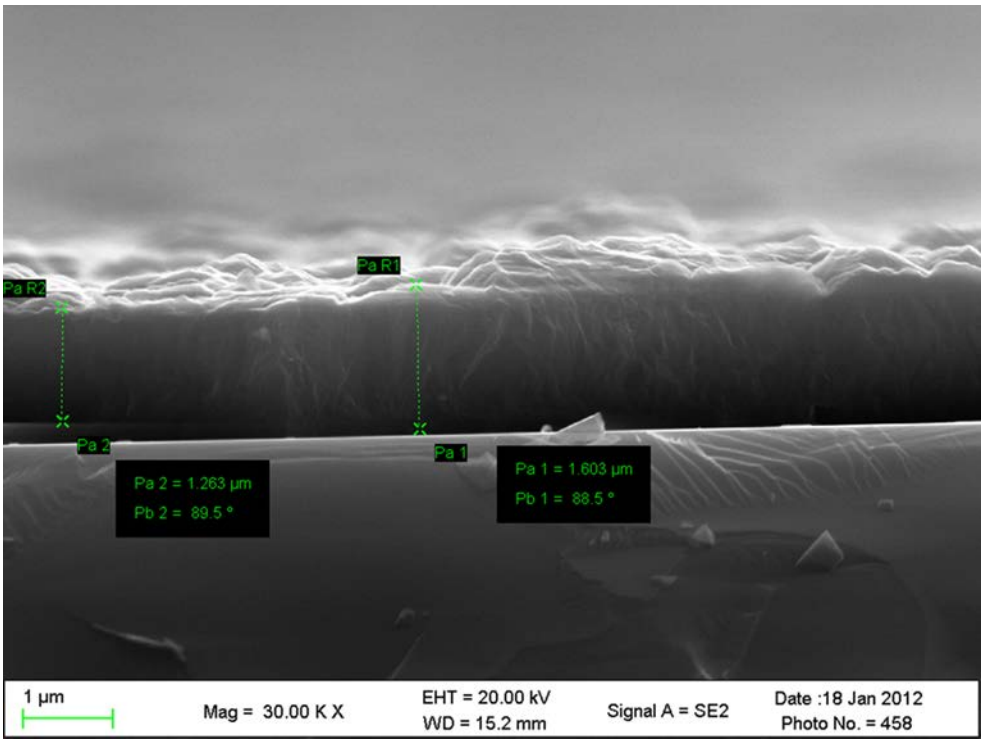

Figure 62. Cross-sectional SEM of sample 21. Showing a BP thin film of 1.6 um in thickness on Si

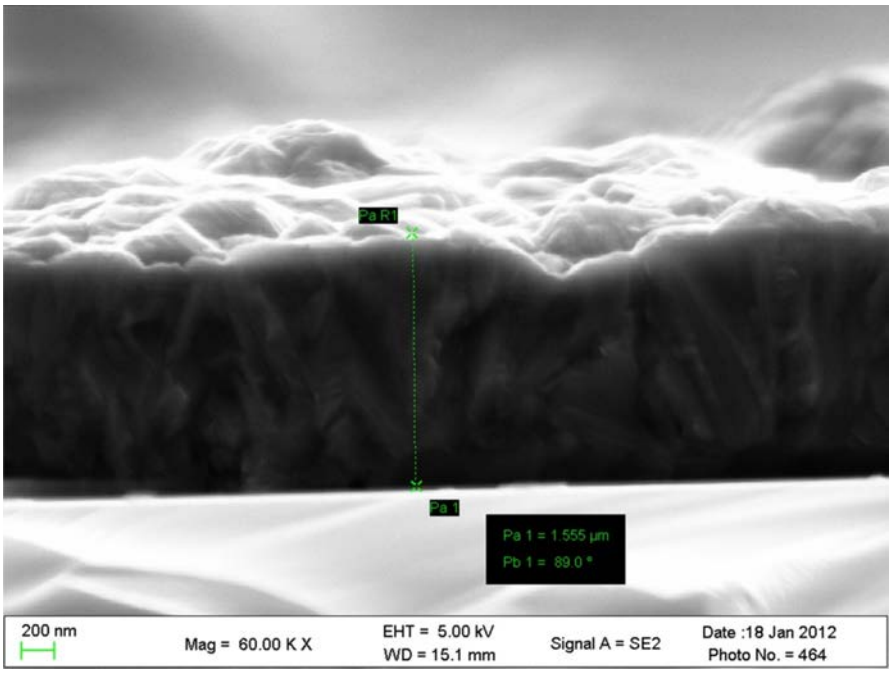

Figure 63. Cross- sectional SEM micrograph of sample 21. Suggesting columnar growth

Sample 22

Sample 22 is the second sample in a 7 sample series of samples designed to determine the optimum BP on a Si substrate. Experimental parameters are shown on Table 5 and are identical to sample 21 with the exception of flow rates of diborane and phosphine. In this sample, the respective flow rates were increased from 10 sccm and 100 sccm in sample 21 to 30 and 300 sccm respectively. The result was an increased mass gain of 3.31 mg compared to a mass gain of 1.24 mg in sample 21. This is a percentage change of 167% and is expected due to the increased amount of gas flowing through the reactor. The average film thickness increased from 1.02 um to 2.72 um a percent change of 167%. The flow rate ratio was unchanged from sample 21. Figure 64 shows photographs immediately post deposition. Film coverage appears complete across the entire surface of the wafer and no thickness gradients were observed. Cross sectional SEM micrographs shown in Figure 65 depict a columnar BP film with a maximum thickness of 4 um. Overall morphology for this sample appears similar under SEM to sample 21.

Samples 23 -27

The remaining samples in the series are briefly discussed together. Appendix C contains Figures with images of these samples. Samples 23 and 24 were grown using the same parameters as in samples 21 and 22 and little difference is seen in these samples. Repeating growths under the same reactor conditions was necessary to examine reproducibility in successive experiments and to confirm reactor stability. The resultant growth rate for samples 23 and 24 compare closely with that obtained for 21 and 22, respectively. Mass gain for sample 23 was 1.17 mg compared to a mass gain of 1.24 mg for its cohort sample 21. Mass gain for sample 24 was 3.25 mg compared to a mass gain 3.31 mg for sample 22. Similar crystalline structure is present in both samples with the major difference being the increase in film thickness between 23 and 24

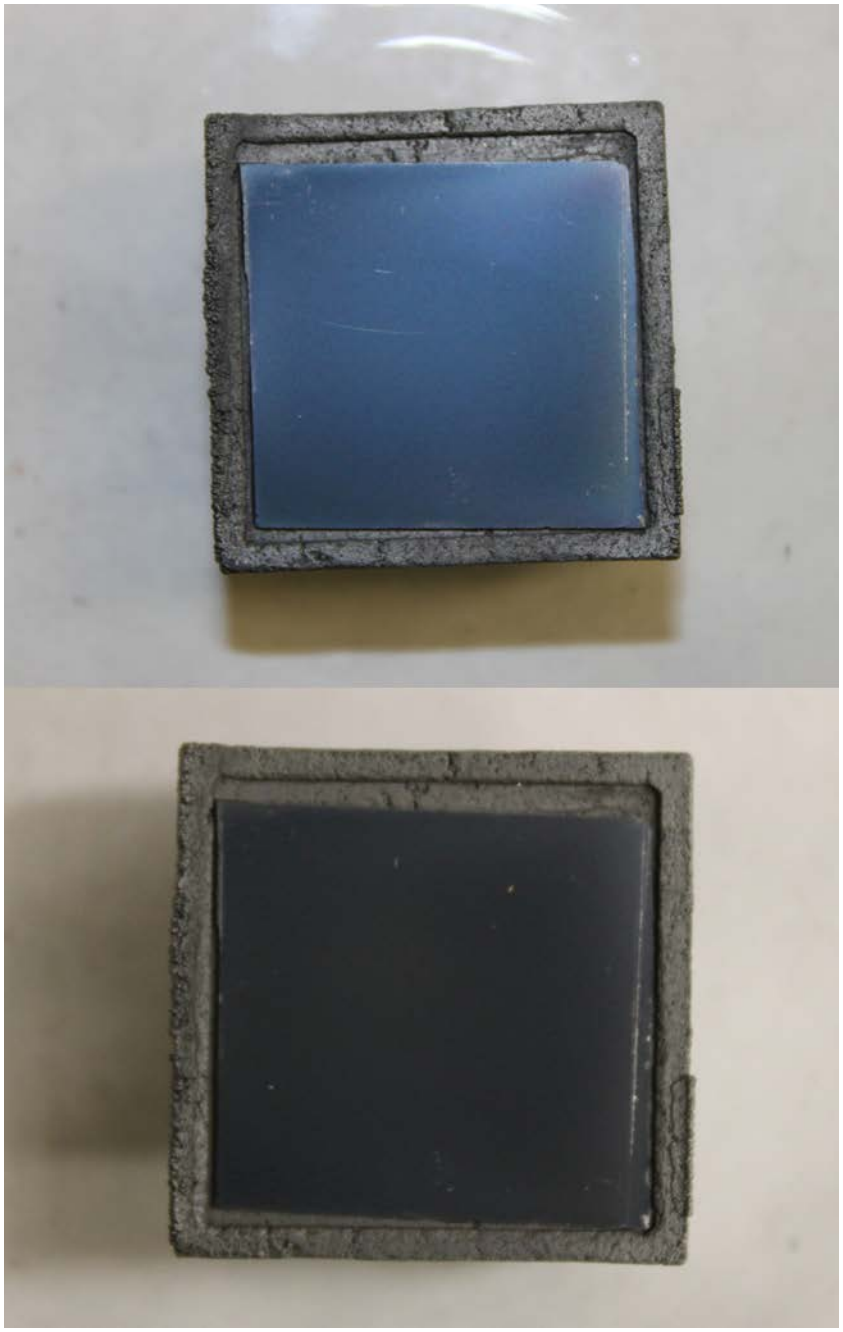

Figure 64. Photographs of sample 22 post deposition

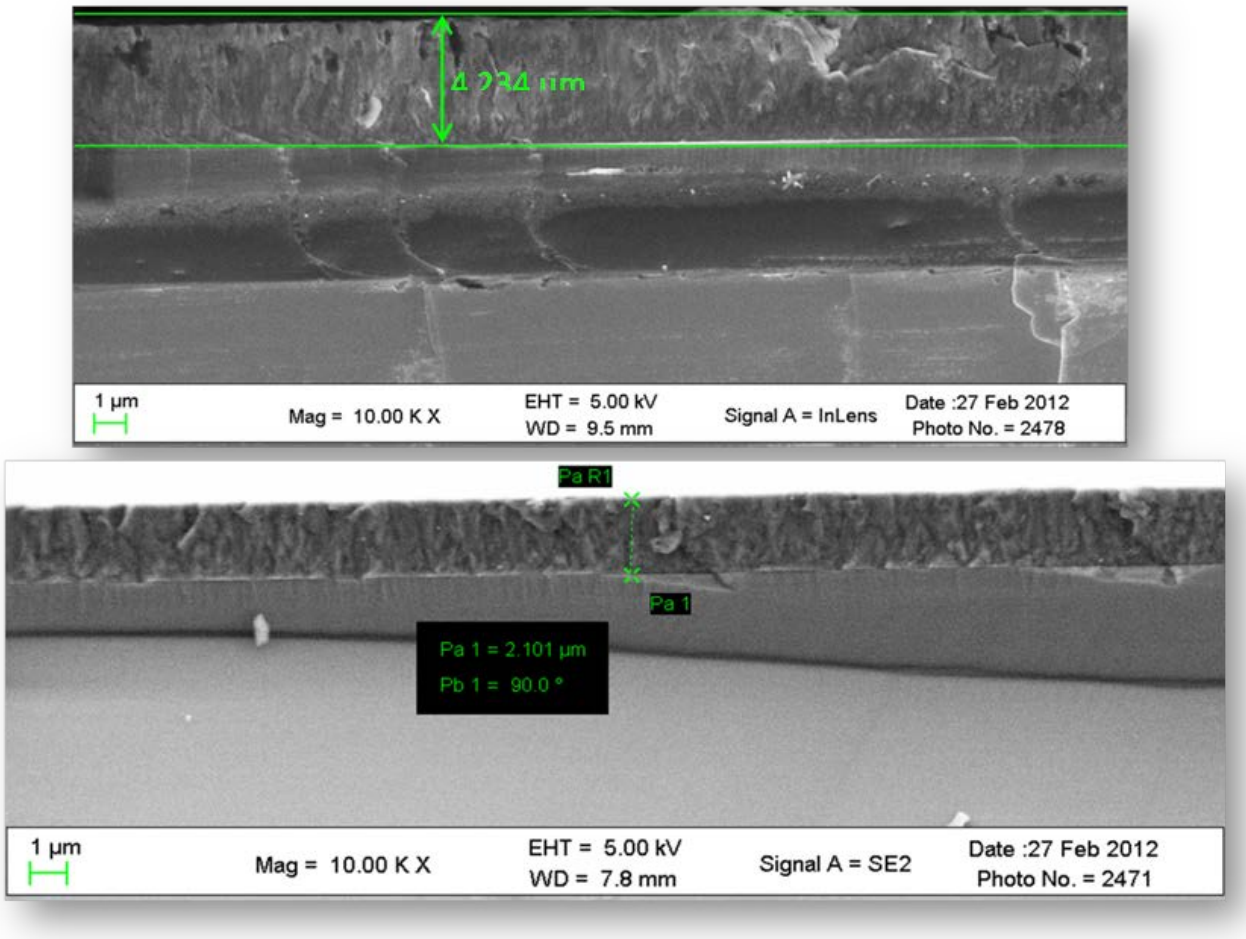

Figure 65. Cross sectional SEM images of sample 22. Showing columnar film of BP with a maximum thickness of 4 um

resulting from increasing the flow rates by a factor of 3. Predicted film thicknesses of each sample compares well with measured thickness in SEM.

For sample 25, parameter settings for pressure, PH_3 and hydrogen balance flow rate remain unchanged from samples 22 and 24, whereas the diborane flow rate is reduced to 1/3rd. Growth temperatures were similar. The mass gain for sample 25 was 1.03 mg which is approximately 1/3rd that of samples 22 and 24, and nearly equal to that of samples 21 and 23, which were grown at the same diborane flow rate. The resultant film has a conical appearance indicating a greater depletion of growth species as the flow moves from the front to the back edge of the sample. Surface SEM imagery shows a rough continuous film at the front of the sample with particles becoming further separated as growth species are depleted toward the back edge. The low mass gain in this sample is attributed to the lower diborane flow rate setting.

In Sample 26 the phosphine flow rate setting was 150 sccm, while the diborane flow rate was 30 sccm. This sample is the antithesis of sample 25 and was selected to further isolate the importance of diborane concentration and thin film growth. By decresing by one-half the phosphine flow rate from the previous experiment and increasing the diborane flow by a factor of three, the mass gain was 3.24 mg, about $1/3^{rd}$ that of sample 25. Cross sectional SEM images of sample 26 shown in Figure 104 show an average thin film thickness of 3.22 um, slightly above the predicted thickness previously reported. Morphology of sample 26 is consistent with the earlier samples in this study as shown by SEM microscopy. This sample confirms that diborane concentration limits the growth rate over a wide range of phosphine concentrations. Phosphine concentration does not seem to directly correlate with observed film thickness.

In sample 27, the pressure and hydrogen balance flow rates were returned to those used in samples 22 and 24 but the growth temperature was raised slightly from approximately 800 °C to

855 °C. This sample had a mass gain of 3.09 mg, with an average film thickness of 2.54 um. This is consistent with earlier observations that the growth rate varies only slightly with temperature in the range of 800-850 °C. Overall, the results of the parametric study establish that diborane is the limiting factor for BP film growth in this regime and a Volmer–Weber growth mode appears to be followed under these conditions on silicon.

BP-Si Interface Morphology and Fine Structure

Sample 7

While mass gain, SEM, and Raman analyses provide useful information on growth rates, confirmation of BP formation and gives insight into growth modes, it does not interrogate the interface which is critical for heteroepitaxial growth. The interface between the substrate and thin film serves as the foundation for future growth. The morphology at the film interface is subject to intrinsic stress and observations of morphology and defects are useful in understanding their effects on future growth. As previously shown, SEM micrographs and even cross sectional SEM images are not sensitive enough to probe the interface with significant resolution in order to observe morphology and defects. TEM must be employed for this purpose.

TEM analysis was performed on two samples grown in silicon substrates to probe the interface morphology, the crystal structure and defects developed in BP films grown on silicon. In addition, TEM-EELS was performed on these samples to provide much needed information on the chemical composition of the films. For a brief discussion of EELS fundamentals refer to chapter 2. The first sample that was analyzed by TEM and TEM-EELS was sample 7. Table 6 shows the experimental conditions for this sample.

Table 6. Experimental Parameter settings for Sample 7

Sample	Pressure (torr)	Temp (°C)	H_2 (sccm)	PH_3 (sccm)	B_2H_6 (sccm)	Duration (hrs)	Mass Gain (mg)	Pred. Film Thickness (µm)	PH_3/ B_2H_6
7	630	816	2500	30	30	2	8.60	7.06	10

The thickness of this sample, measured by SEM at 9.4 um, created a challenge for TEM microscopy and required more preparation time than for thinner samples. The deposition time was reduced for most of the later samples to make them more appropriate for TEM analysis. Figure 66 shows a photograph of the sample immediately after deposition. The coverage looks even with some artifacts observed on the surface of the sample which are circled for easier identification. These artifacts were determined to be debris from the CVD and were removed from the sample surface with a sweep of dry nitrogen prior to analysis being conducted. Surface and cross sectional SEM images were obtained on samples prior to submittal for TEM. Surface SEM images given in Figure 67 show a rough continuous film, consistent with observations on other films grown on silicon. Cross sectional images presented in Figure 68 show columnar growth similar to that seen in other films.

Figure 69 shows a TEM micrograph of the entire film from interface to surface. Due to the narrow field of view on the instrument the images must be taken individually and stitched to provide the entire 9.4 um film. The unique thickness of this sample provided some key information regarding the stages of growth in this film. Broadly, the TEM images show that BP growth on SI substrates create an amorphous region at the interface and then small polycrystalline grains followed by larger polycrystalline grains. A revealing aspect of this sample is the polydispersity of the varying crystalline phases observed in the large polycrystalline region.

Figure 66. Photograph of sample 7 post deposition. Image shows even covering. Variations in colors are caused by shadows. Artifacts from CVD reactor are circled in red for easy identification. These were removed prior to deposition

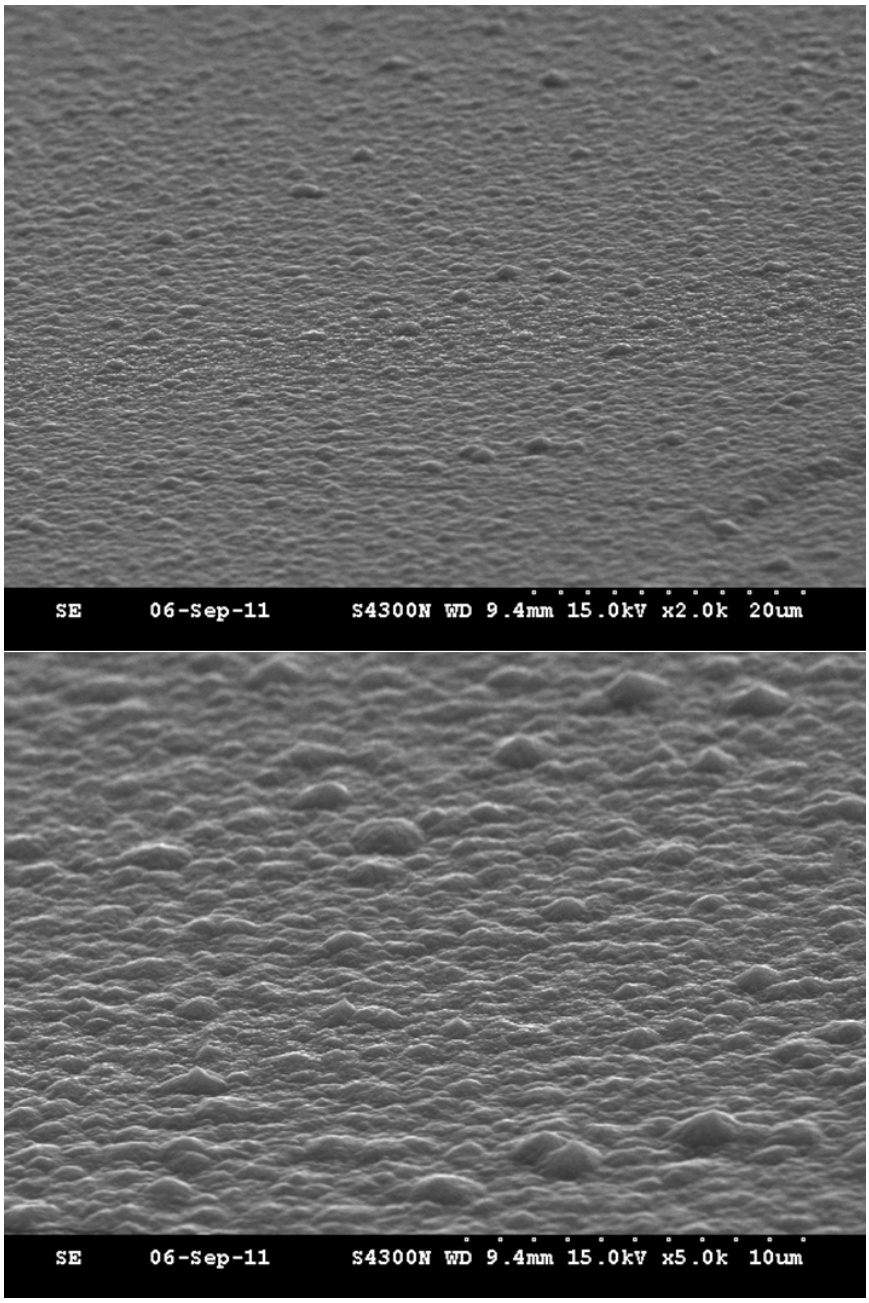

Figure 67. Surface SEM images of Sample 7

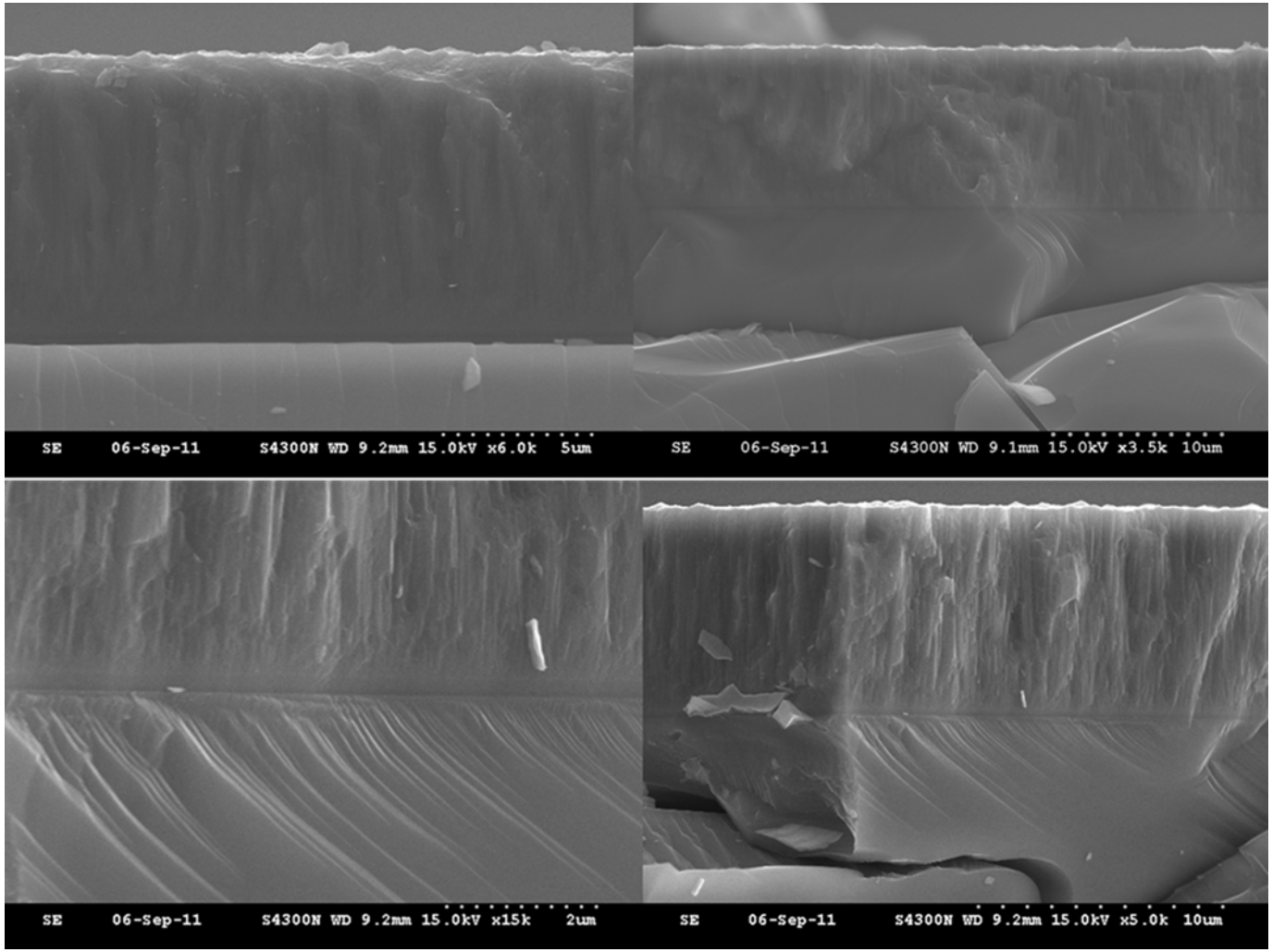

Figure 68. Cross-Sectional TEM images of BP on Si

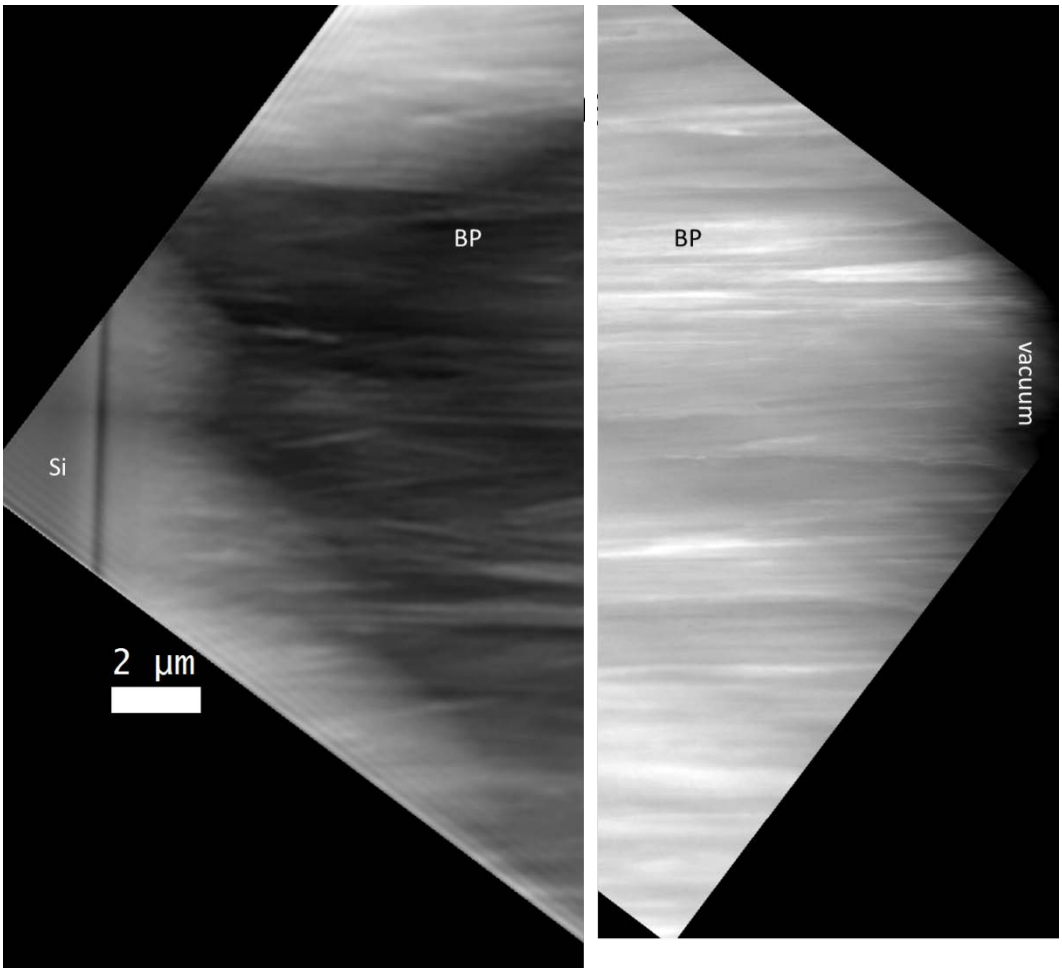

Figure 69. TEM image of entire Sample 37

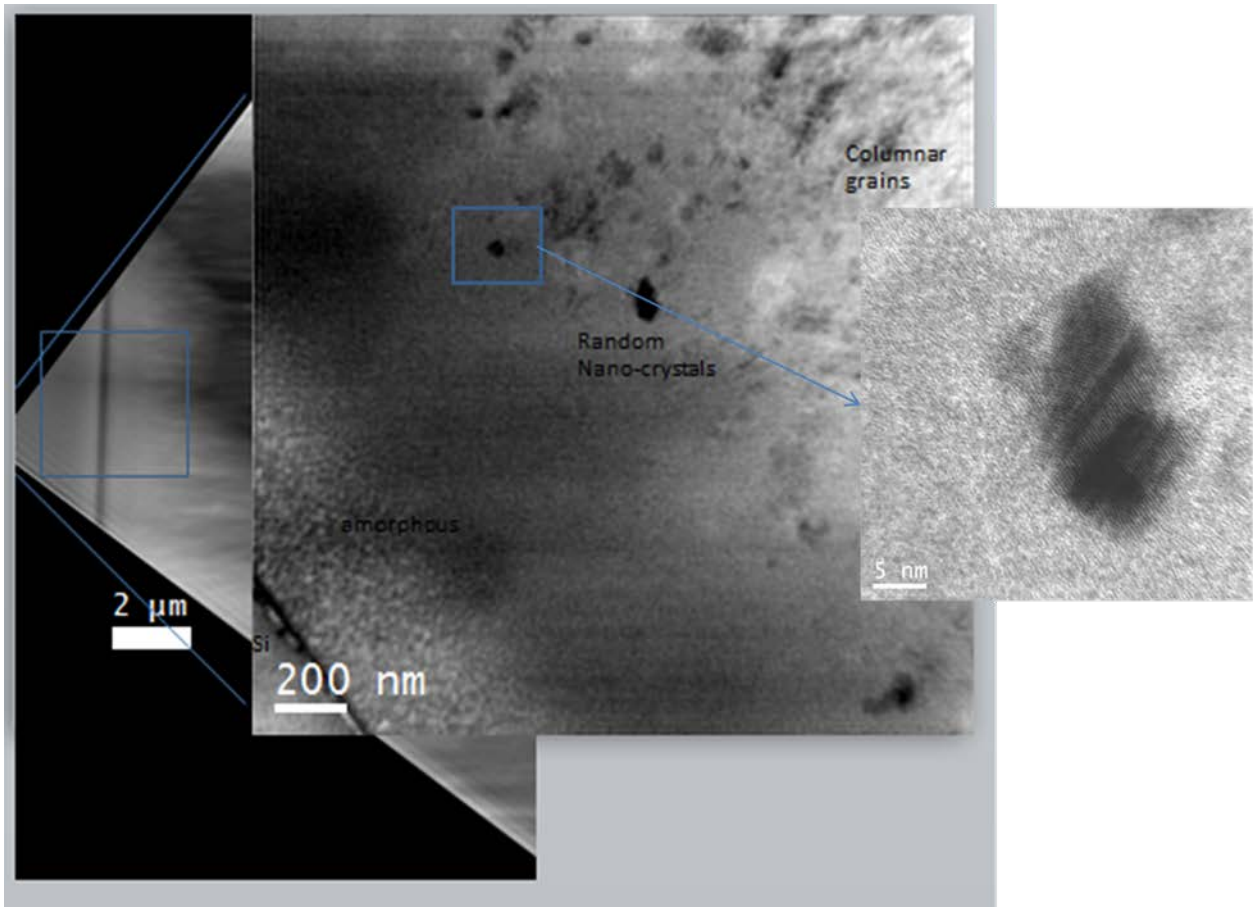

Figure 70. TEM image of BP-Si system in the near-interface region. Showing the presence of a BP nanocrystal

These crystals have <110> orientation, indicating that the preferred growth direction for BP is <110>. Figure 70 shows a TEM micrograph taken of the BP –Si interface and near interfacial region with the insets providing blown –up images of selected portions of the film. This region consists of an ~ 1 μm amorphous region of BP extending outward from the interface, followed by random generation of BP nanocrystals over the 2nd μm and polycrystalline columnar growth extending out to the surface. The dark spots that are randomly distributed in the first inset are BP nanocrystals. The last inset shows an enlarged view of one of the crystals. The spacing of the planes in this crystal is consistent with that of BP.

Stoichiometric data for sample 7 was obtained by scanning the EELS probe across the Si-BP interface. Figure 71 shows the location of the spectrum highlighted in the colored box and the resultant spectrum below the image. The EELS spectrum is a graph of atom % verses distance. The blue line is the Si line and is shown at unity suggesting the presence of pure Si. The Si signal decreases as a function of distance and the ingrowth of B and P are represented by green line and red line respectively. A distance of 30 nm from the origin of the scan, the B and P lines overlap indicating equal distribution or 1:1 ratio of both B and phosphorus in the film and confirming the presence of boron monophosphide. EELS can also be used to identify the difference between amorphous and crystalline BP. Using the same sample location shown in Figure 71, a graph of intensity verses energy loss (Figure 72) shows a clear difference in the fine features of the spectrum. The green line is the intensity vs. loss plot of the amorphous region of the sample. There is little detail in the spectrum and no observable resolution of feature. In contrast, the blue line is the intensity vs. energy loss plot of the columnar crystal region, closer to the surface of the film. The peaks from L shell electrons from P and the K shell electrons from B are clearly resolved.

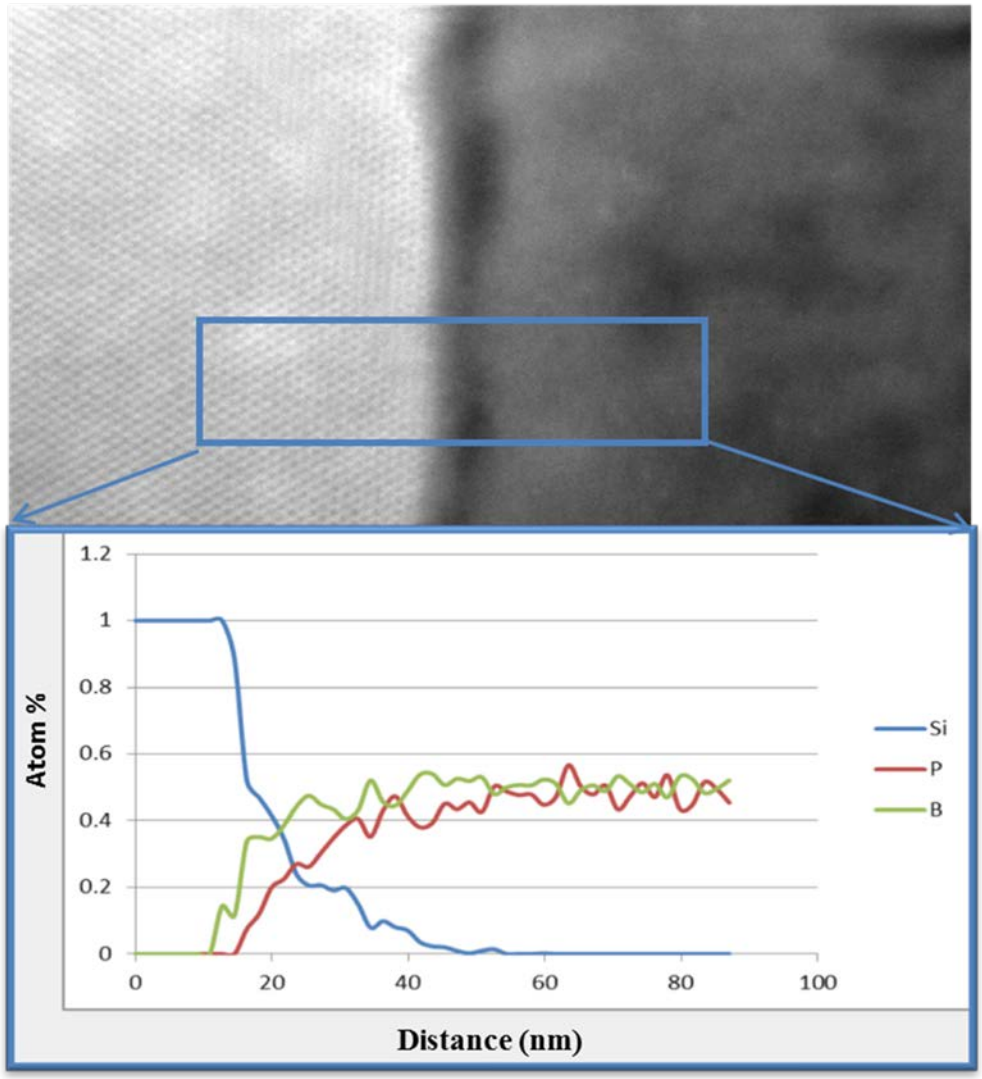

Figure 71 TEM-EELs spectrum of Sample 7. Spectrum acquired by scanning across Si-BP interface

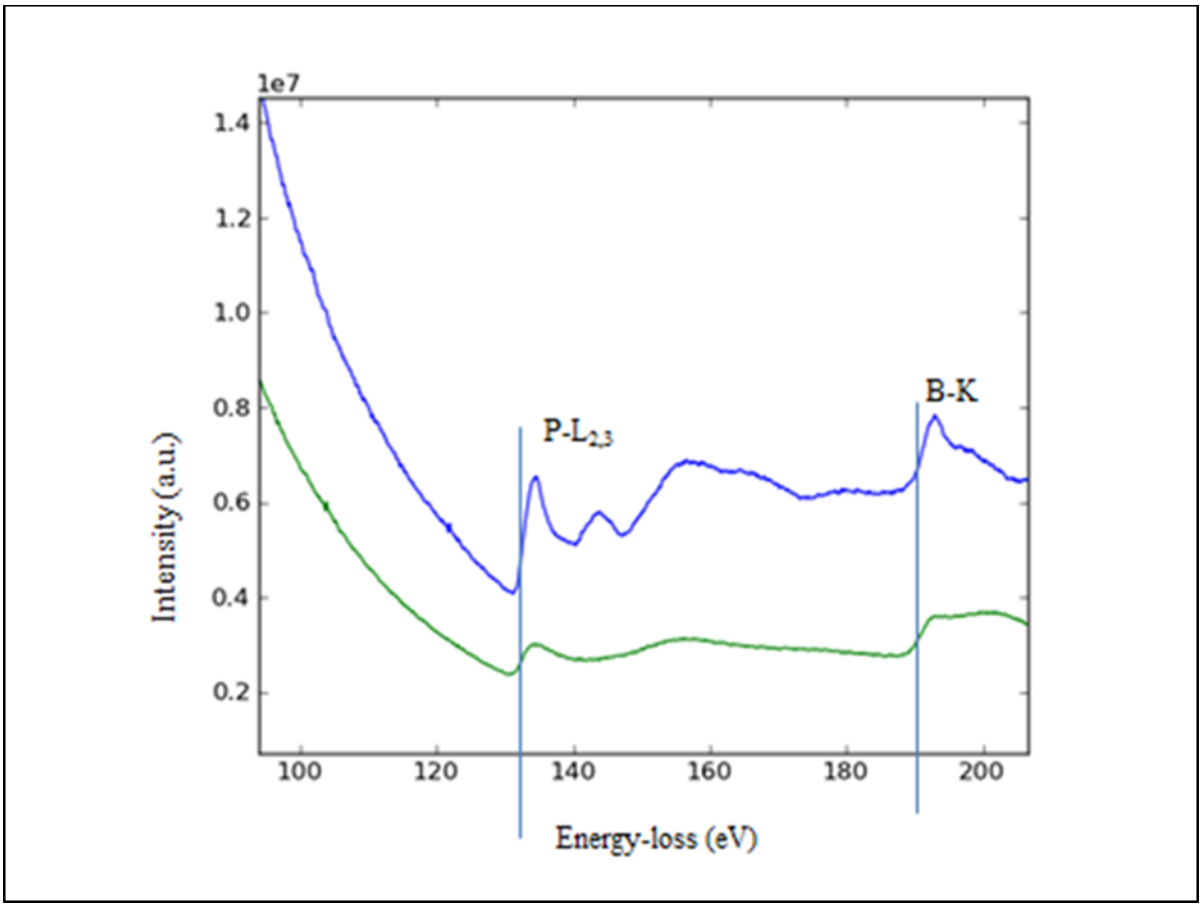

Figure 72. TEM- EELS plot of Intensity vs. energy loss for amorphous and polycrystalline BP

The TEM results on sample 7 provided important insight that was used to guide future growths. The large amorphous region at the interface needs to be eliminated if epitaxial growth is to be achieved. Slowing the growth rate should help and allow ordering to occur. It was also suggested there may still be residual oxygen at the substrate surface. Sample 7 was grown prior to increasing the in situ hydrogen etch time to 20 minutes and may have been affected by oxygen, though there was no evidence of oxygen in the TEM-EELS. Guided by results from the parametric study (samples 21-27) and other later growths on SiC, the following parameters were chosen for sample 37. These included flow rates for diborane and phosphine at 20 sccm and 100 sccm, respectively to give a flow rate ratio of 5, substrate temperature of 812 °C and system pressure and hydrogen balance flow rate were unchanged from all previous experiments at 630 torr and 2500 sccm respectively. Figure 73 shows a photograph of the sample post deposition. The photo depicts even coverage with a slight discoloration on the right side of the sample. This is the side nearest to gas flow introduction. Raman spectroscopy of this area confirmed the presence of BP. Because this sample was selected for TEM analysis prior to deposition, only surface SEM micrographs were obtained. The surface SEM images shown in Figure 74 indicate a continuous rough film. SEM of this sample is similar in morphology to samples shown in the parametric study. Higher magnification images shown in photos C and D of Figure 74 still suggest a coalescing island growth mode, not ideal for smooth highly ordered films.

The sample was prepared for TEM analysis by Guoling Li.[66] . The thickness required for electron tranparency in BP is less than 80 nm. Cross sectional TEM images of the BP-Si interface given in Figures 75 -77 show a distinct amorphous region of BP of approximately 50

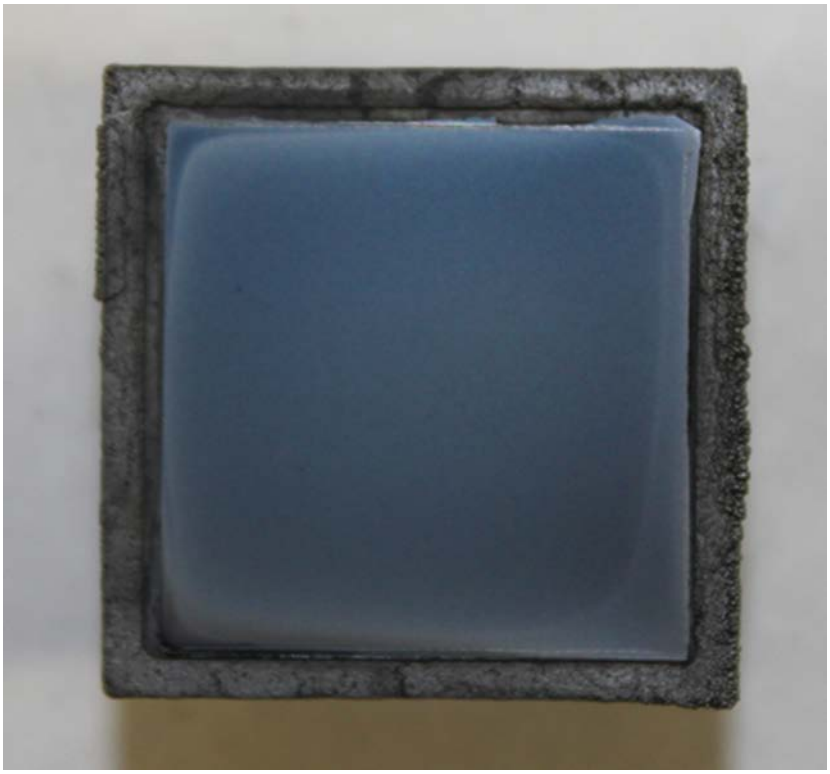

Figure 73. BP Sample 37 deposition on Si

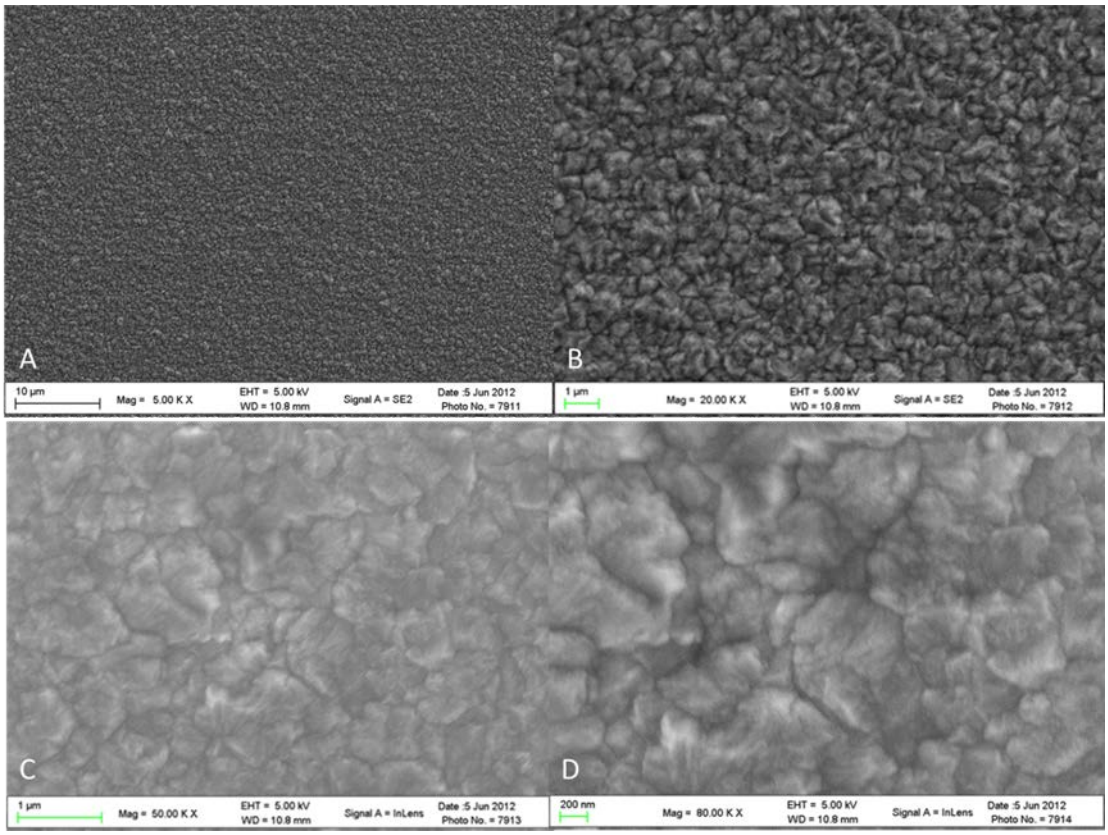

Figure 74. Surface SEM micrographs of BP on intrinsic Si. Magnifications range from 5K X to 80K X. Surface morphology is indicative of Volmer-Weber growth mode

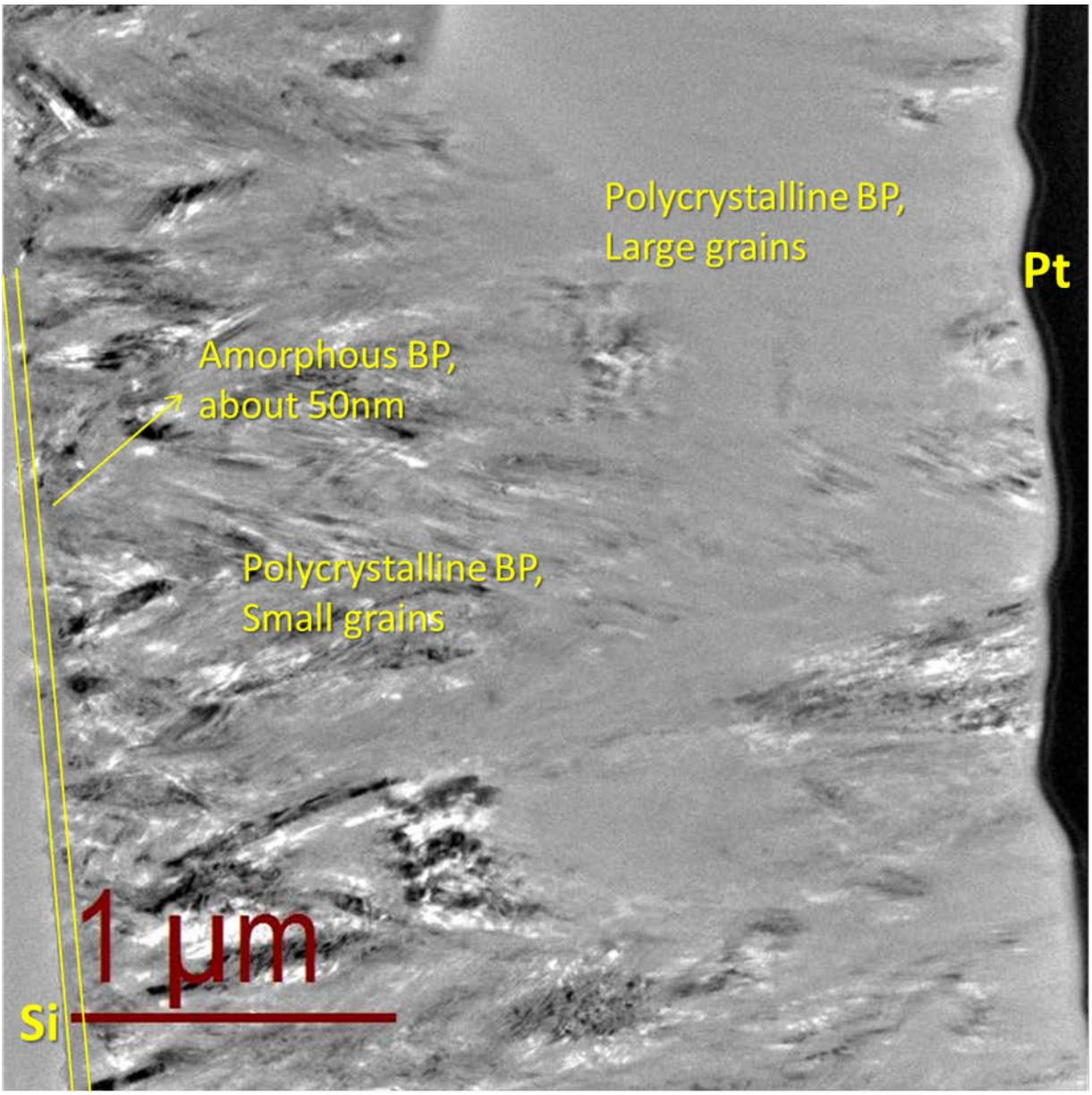

Figure 75. TEM cross section showing amorphous BP interface

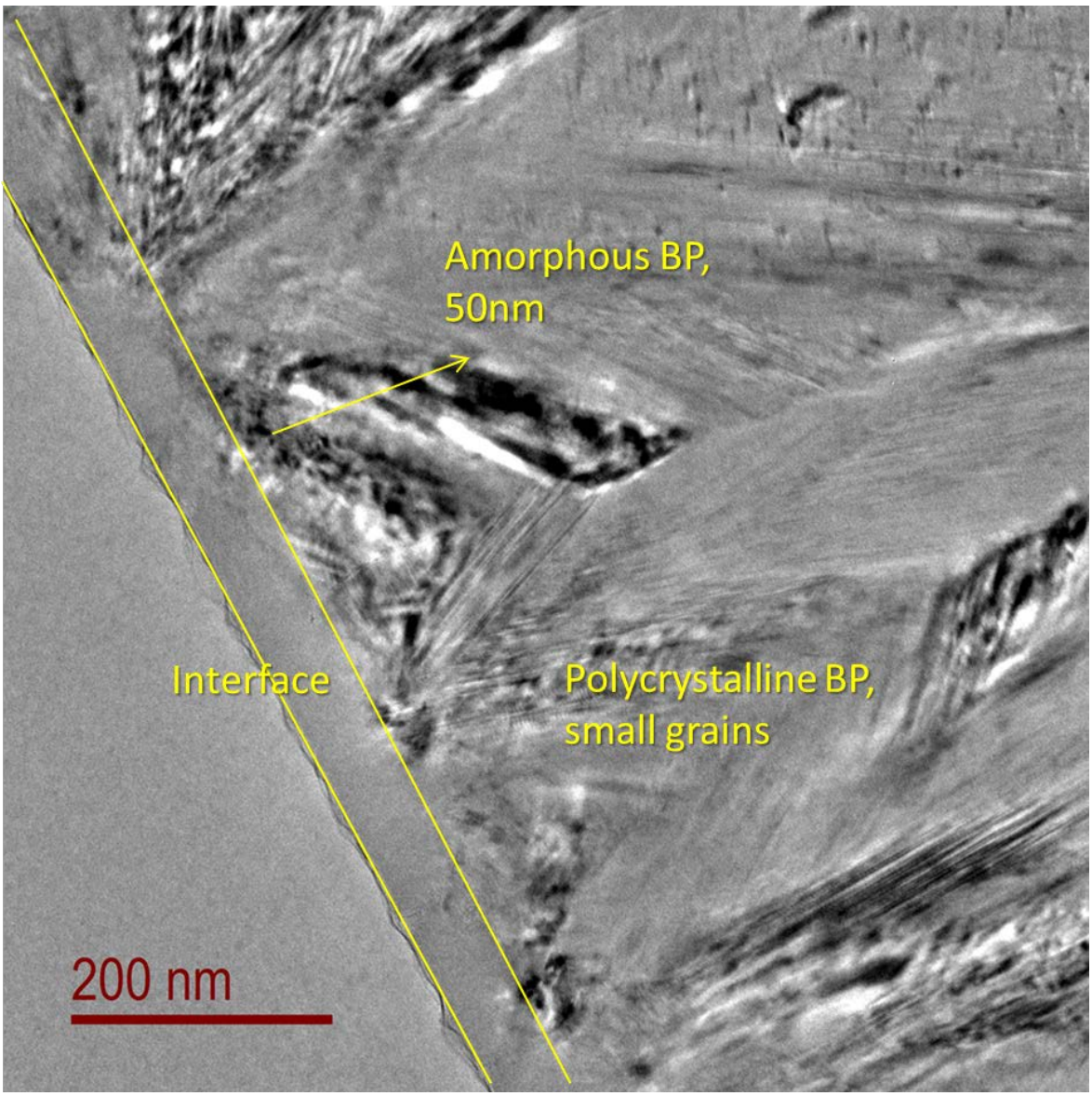

Figure 76. Zoomed image of Figure 75. Showing interface in greater detail

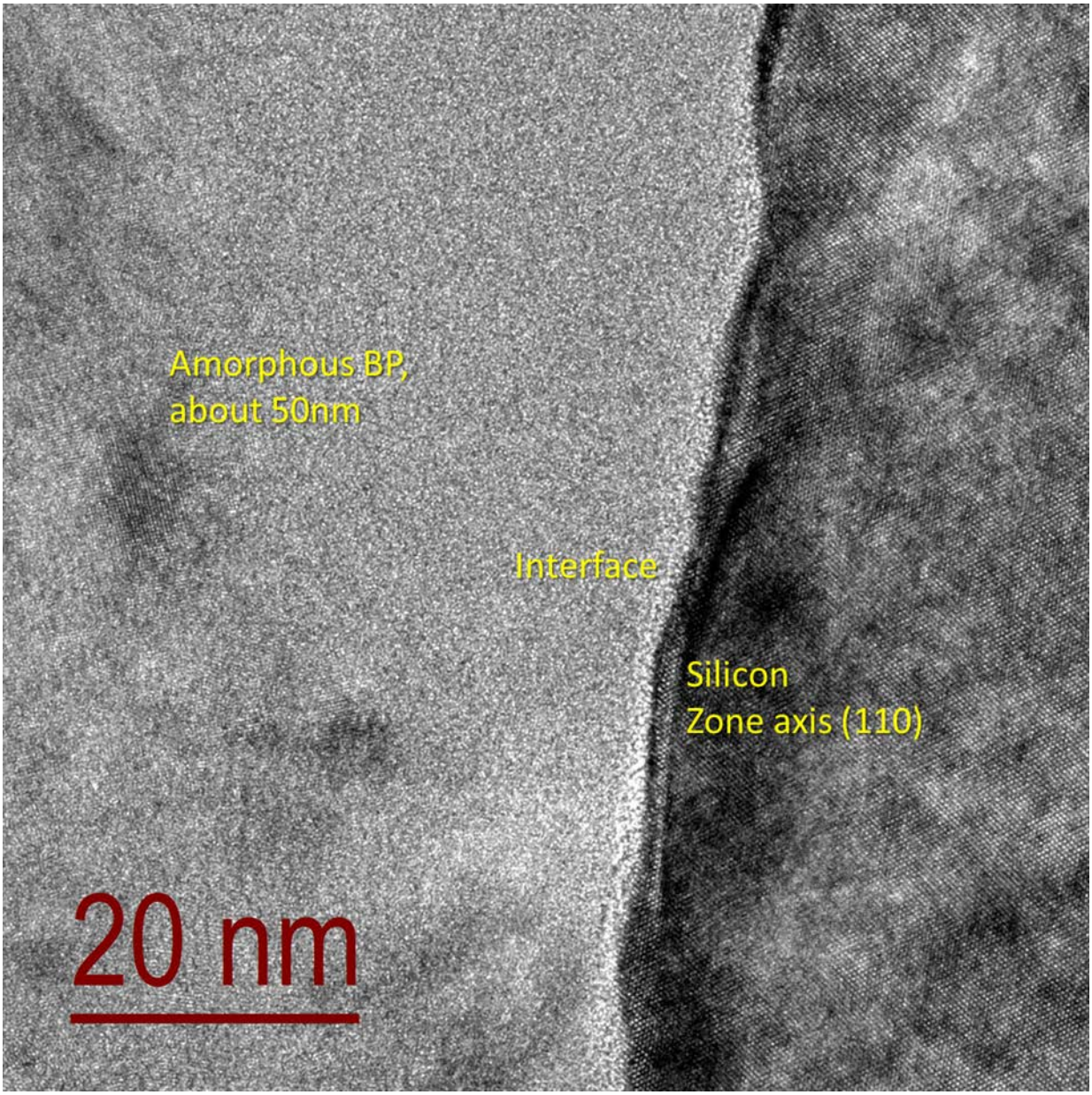

Figure 77. TEM cross section of BP-Si interface at 315 K X magnification

nm thickness at the interface. Clearly, changes in growth parameters and surface preparation have greatly reduced the extent of amorphous region. After ~50 nm of film growth, small grain polycrystalline BP forms and propagates for approximately 1.25 um before large grain polycrystalline BP develops and grows for an additional 1.5 um. This is confirmed in the selected area diffraction (SAD) studies of the sample. Electron diffractions of selected samples are valuable for analyzing the crystallinity and defects in the film and how they progress as the film thickens. Specific regions of the sample were identified based on their appearance in the cross sectional TEM images. SAD images were obtained at the interface, small crystalline region and the large crystalline region. The images shown in Figure 78 depict the SAD patterns from the approximate areas marked by the yellow circles. The circles, labeled A, B, and C, correspond to the SAD pattern with the same letter. The diffraction image from section A contains electron diffraction from the silicon crystal, the amorphous interface and small grain polycrystalline BP. The single crystal silicon substrate shows up as a hexagon pattern of spots relative to the central beam position. If single crystal BP has been grown epitaxially on top of the silicon, another hexagonal pattern, slightly displaced from the silicon spots would have been observed. Instead, clusters of bright spots develop in a ring surrounding the middle of the image, consistent with a number of BP crystals with varying orientation. An electron diffraction image from a powder sample with random crystal orientation would have produced a continuous diffraction ring. Furthermore, progressing from pattern A to pattern C shows a decrease in the number of observed diffractions in the ring, indicating the number of crystal orientations is decreasing, an observation consistent with the cross sectional TEM image indicating growth of larger BP crystals. A comparative analysis of the images in Figure 79 to those shown in Figure 78 further show the presence of larger crystal BP near the surface of the film. The TEM image shown in the upper left corner of Figure 78 shows the approximate sample location of the following SAD pattern. The increased intensity and the reduction in number of diffraction peaks in the ring in

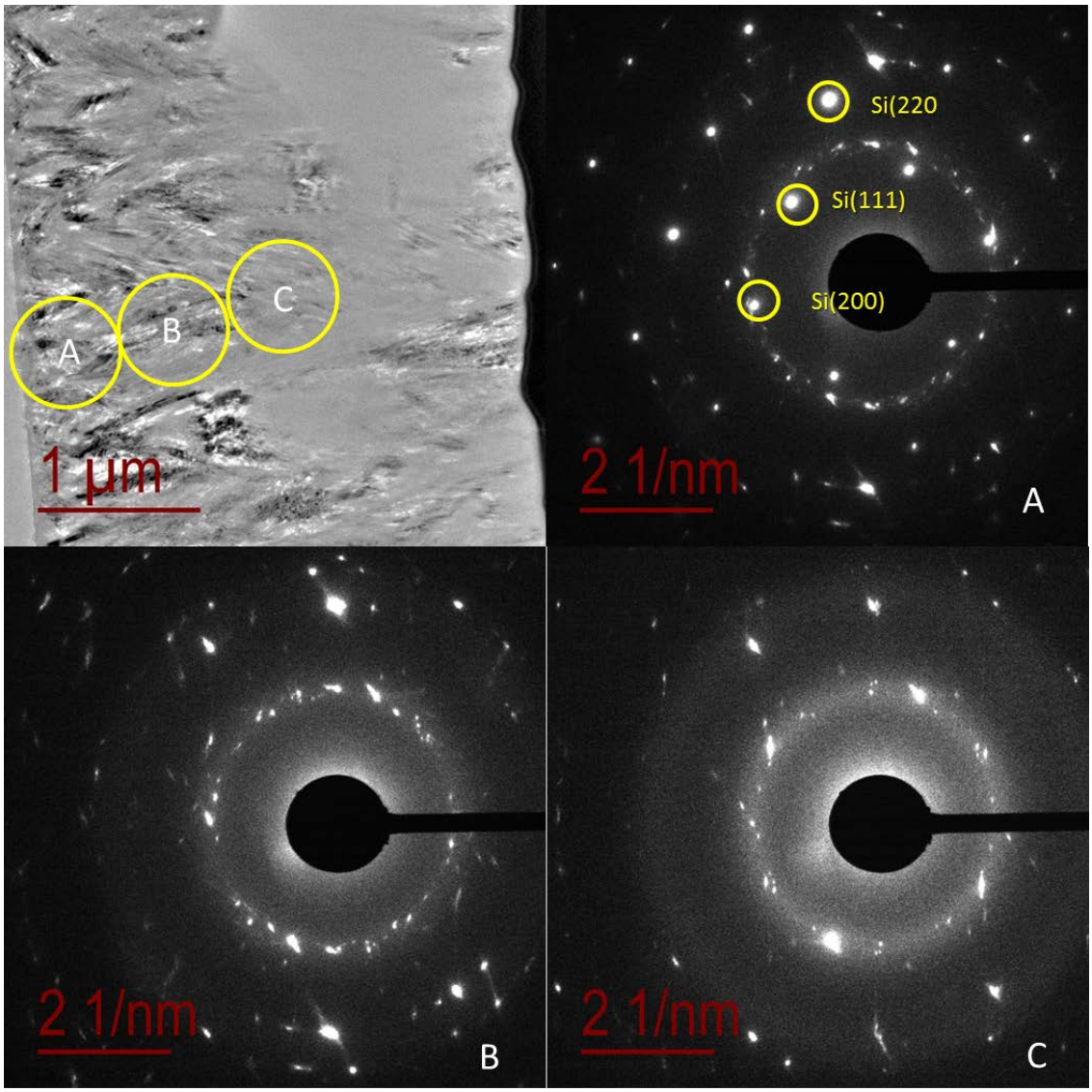

Figure 78. Figure showing the SAD pater for specific regions within the BP-Si thin film. Each SAD pattern corresponds to the region with the corresponding letter shown in the top left.

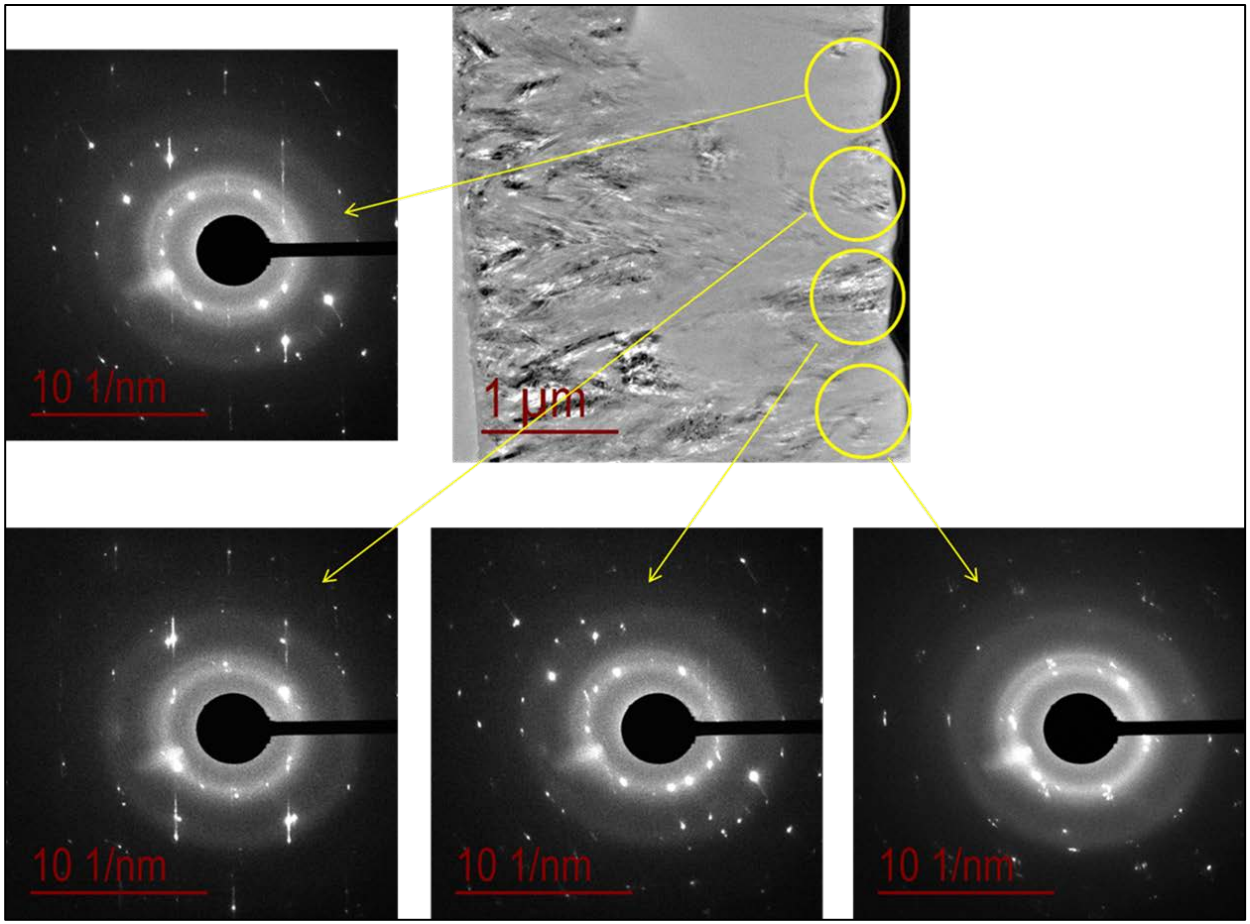

Figure 79. Cross sectional TEM image and corresponding SAD Patterns of the Near surface region of the BP film on Si

Figure 79 relative to Figure 78, indicates larger BP crystals are present in the near-surface region of the film

Summary

The preceding set of experiments address the controlled BP deposition on Si substrates. A parametric study was conducted to establish a reliable set of conditions for BP deposition on Si. Early experiments were subject to variability in BP growth rate; this was not fully explored but attributed to system conditioning and possibly incomplete surface preparation. Despite the growth rate variability, relevant observations were made from the data set regarding the impact of temperature under constant conditions as well as the role diborane and phosphine play in BP deposition. Raman and XRD analysis of the films confirmed the presence of BP in all samples. SEM microscopy was useful in measuring thicknesses and identification of bulk film features but showed limited use in interfacial analysis. To better probe the interface, TEM was employed. Relevant findings from TEM probing of the interface region showed that an amorphous region is present at the BP –SI interface and is most likely the result of intrinsic strain due to the large lattice mismatch of Si and BP. Additional imaging and analysis via TEM demonstrated a hierarchy in film order as a function of thickness. Bulk film analysis showed the formation of BP as auto terminated nanocrystals. These structures seem to serve as seeds for growth of columnar grains observed in many of the SEM cross sections. TEM –EELS confirmed the presence of boron monophosphide in lieu of the other known BP polytype, boron subphosphide. BP on Si substrates is not suitable for device fabrication and further experiments were abandoned in favor of a more suitable material for epitaxy, SiC.

CHAPTER IV
DEPOSITION ON SILICON CARBIDE SUBSTRATES

A fundamental consideration in semiconductor heteroepitaxial deposition is induced strain from lattice mismatch. The previously reported work of BP on Si showed a persistent presence of an amorphous area at the BP-Si interface which was attributed to poor lattice matching. As the film grew, random nano particles formed and the eventually columnar BP morphology was observed in cross sectional SEM. This amorphous area followed by nucleation and crystal growth suggests that induced strain at the interface was sufficient in magnitude to prevent long range order from initially developing and epitaxial growth to be established. As the film waxed in thickness, the induced strain from the lattice difference between Si waned and crystalline order developed. By minimizing the strain, it should then be possible to allow crystalline order to be established at the interface. This interfacial order would serve as a foundation for long range order in the film, maximizing the potential for single crystal growth.

XRD on Offcut Wafers

Prior to the discussion of individual samples, a brief discourse on the evolution of XRD analysis used on SiC substrates is warranted. It was proposed that if a perfect, i.e., single crystal, epitaxial film of BP were grown on the basal (0001) plane of 4H or 6H SiC, that film would have <111> orientation. The XRD of that film would then consist of diffraction solely from (111) planes. Therefore, a possible measure of epitaxy in the film is the ratio of (111) to (220) X-ray diffraction intensities. Growth in the <111> direction for BP is indicative of high quality growth, while growth in the <110> direction has been found to grow out of amorphous material. Diffractions from (110) planes are forbidden and therefore (220) diffractions are used as a measure of (110) material. Because of the 4° (or 8°) off cut of the SiC wafers, the diffraction planes of both the

SiC (0004) and the BP (111) are tilted by 4° (or 8°) from the surface normal. Due to this relationship, conventional theta/2-theta scans, aligned to the surface normal, will give misleading results. This was recognized after engaging Dr. Elliot Specht of ORNL, who is an expert in X-Ray diffraction, to perform analysis on a couple of samples. Before consulting with ORNL, all scans were taken on the surface normal without regard to the SiC offcut orientation. Therefore the (111)/(220) diffraction ratios measured on offcut SiC wafers were misleading. Figure 80 shows the rocking curve data for samples 31 and 45, measured by Dr. Specht. Rocking curves will show the tilt of the film from the surface normal as well as the full-width at half maximum, which gives an indication of variation in alignment within the film. Here the measured tilt was 5-6°, slightly larger than that expected for a 4° off-cut crystal. Since (111) is higher quality growth, the peaks in Figure 1(a) are sharper (1.6-2.56° FWHM versus to 5.69-6.22° FWHM) than the (220) peaks in Figure 1(b). It is worth noting that due to the broadness of the (220) peak, scans taken on the surface normal may show the (220) peak as relatively more intense than the (111) just by virtue of poorer quality material being grown in the <110> direction. This means that in some of the samples initially thought to be poor quality due to the (111):(220) ratio may actually be better quality, because as the (111) quality improves, the peak seen in the rocking curve will become more sharp, thus reducing the amount of the peak tail seen on the surface normal.

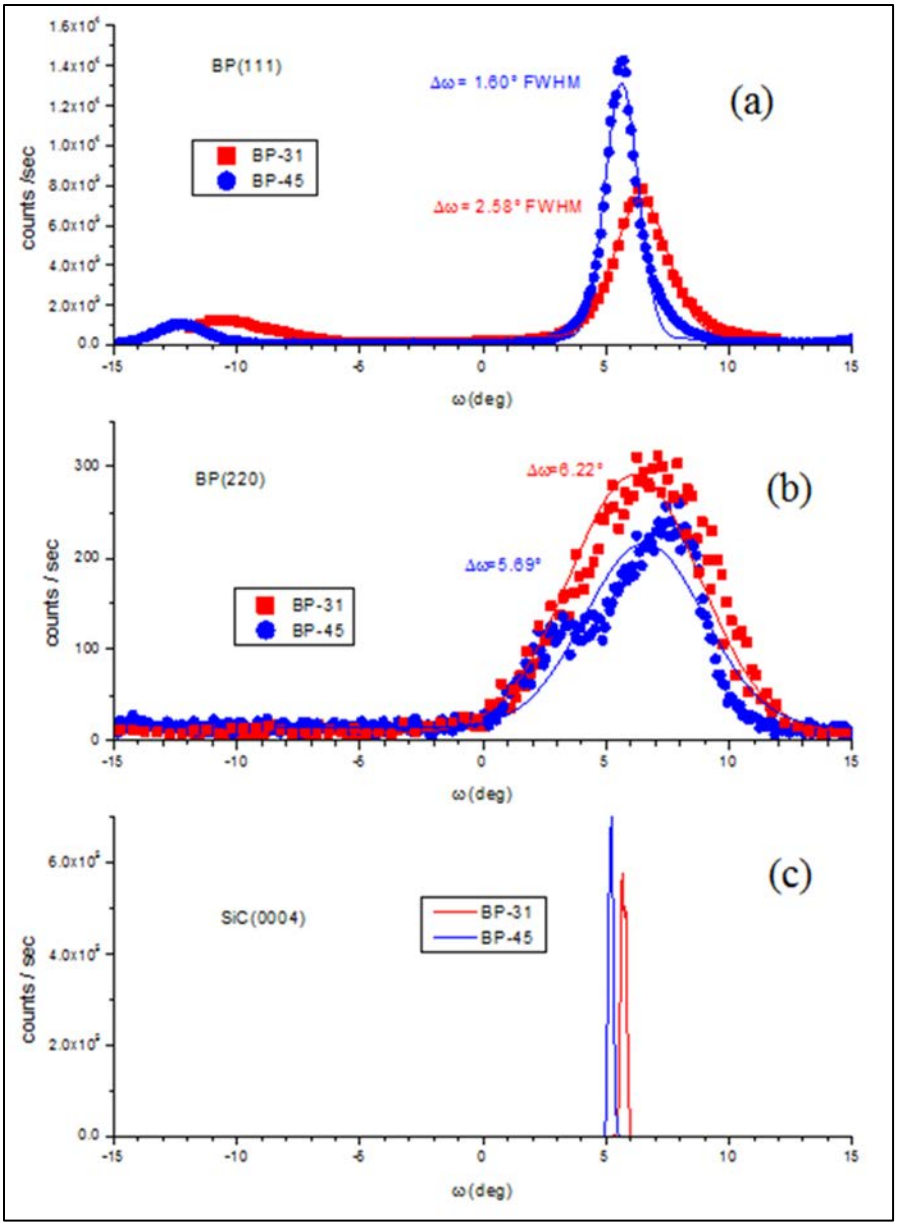

Figure 80. XRD Rocking curves of samples 31(red) and 45(blue). The films align with SiC(0004) and not the substrate surface.

Figure 80 also indicates that the epitaxy is improved for sample 45 compared to 31. As will be presented later, sample 45 was grown at 850°C and sample 31 was grown at 802°C; higher temperatures improves surface mobility and surface ordering. From this point on, all XRD spectra presented for films grown on offcut SiC substrates were recorded with a tilt offset to accommodate for the miscut orientation. The Panalytical XRD analyzer used in this work is not equipped with a four or 5-axis stage to perform rocking curve measurements. Alternatively, theta/2-theta scans can be run in the Panalytical XRD with an adjustable offset, which is adjusted to maximize signal intensity. Generally, setting the offset to -4° is sufficient to optimize the spectrum. An offset angle of this magnitude is plausible when evaluating BP on 4 degree offcut wafers.

Sample 31

Given the small lattice mismatch between BP and SiC, the ability to grow epitaxial BP on SiC was thought possible. Therefore, the immediate focus of the BP depositions on SiC was to demonstrate epitaxial growth of BP on SiC and determine through a series of controlled experiments the growth conditions for epitaxy. The growth parameters demonstrated in Si deposition were used as the starting point for SiC deposition. Table 7, shows a list of applicable experiments and associated parameters performed on 4H 4 ° off cut SiC. The bulk of SiC work was performed on this substrate. BP depositions on alternative SiC orientations will be discussed separately.

Table 7. List of applicable depositions and associated system parameters performed on SiC substrates

Sample #	31	43	45	61	72	73	75	80	81	82	83	84	85	86
Pressure (torr)	630	630	630	630	630	630	630	630	630	630	630	630	630	630
Temp (°C)	802	805	850	950	850	800	1000	850	800	900	950	1000	950	950
H2 (sccm)	2500	2500	2500	2500	2500	2500	2500	2500	2500	2500	2500	2500	2500	2500
PH3 (sccm)	100	100/300	100	100	100	100	100	100	100	100	100	100	100	100
B2H6 (sccm)	20	20/60	20	20	20	20	20	20	20	20	20	20	20	20
Time of run (hr)	0.5	0.5/1.5	0.5	0.5	0.5	0.5	1	0.5	0.5	0.5	0.5	0.5	0.5	0.5
Predicted film thickness (µm)	2.65	22.34	2.72	1.45	2.24	2.33	2.37	2.33	2.80	2.33	2.16	0.98	1.99	2.10
mass change (mg)	1.24	10.45	1.27	0.68	1.05	1.09	1.11	1.09	1.31	1.09	1.01	0.46	0.93	0.98

Initial system parameters for SiC deposition were set identical to the last depositions performed on Si. System pressure was set to 630 torr, hydrogen balance flow rate was maintained at 2500 sccm throughout the experiment. Set point for the diborane and phosphine were 20 sccm and 100 sccm, respectively, for a flow rate ratio of 5. Susceptor temperature was maintained as near to 800° C as possible. The duration of the experiment was kept to 0.5 hours in order to facilitate TEM analysis of the interface. The predicted film thickness was 2.65 µm, calculated using the same formula presented in the chapter on Si. The resultant film, shown in Figure 81 had a mass gain of 1.24 mg. Coverage of the film appears uniform with some variation along the outer edges of the right side of the wafer. Like the Si substrate samples, Raman analysis was also performed and the resultant spectra were remarkably consistent for samples measured. Figure 82 shows an overlay of the measured Raman spectra for selected samples of table 8. Raman data is not available on all samples because the technique was discontinued in favor of more informative analysis methods such as XRD. The observed peaks at 824 cm^{-1} are consistent with BP and match nicely to the spectra shown from depositions on Si. This gives high confidence that changing the substrate from Si to SiC had no deleterious effect on the Raman signature of BP.

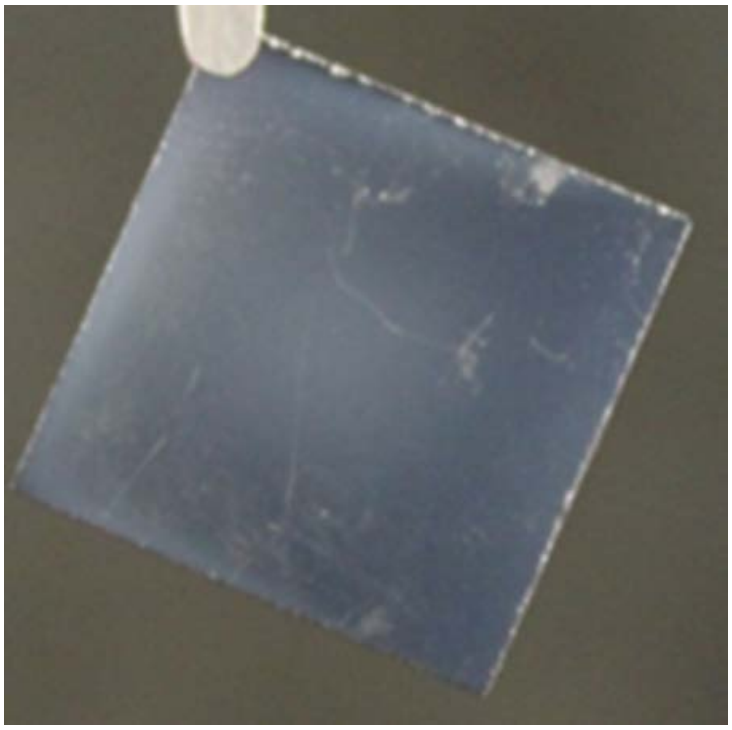

Figure 81. Photograph of BP deposition on SiC immediately post deposition

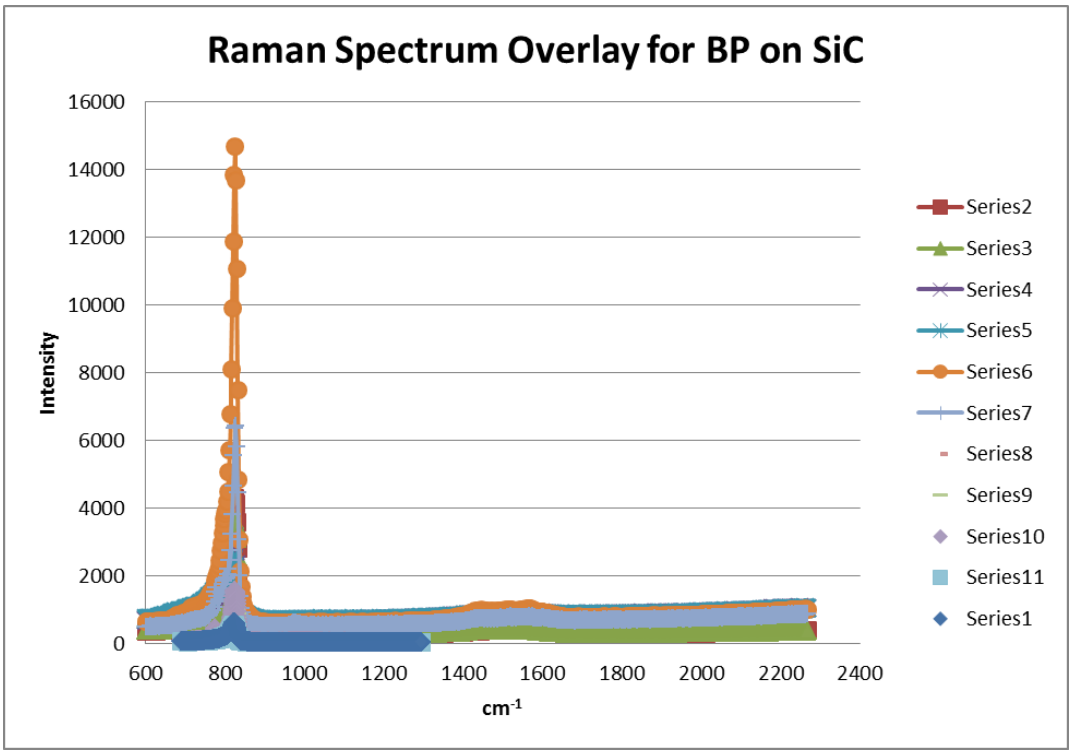

Figure 82. Overlay of Raman Spectra of BP on SiC of selected samples

A surface SEM image of sample 31 (Figure 83) shows a continuous film with a slightly less rough appearance in the film as compared to the experiments performed on Si. Cross sectional SEM (Figure 84) shows an average measured thickness of 2.803 μm, slightly more than predicted. The morphology of the resultant film is different than that observed on Si. The long columnar crystals are not present in the SiC and replaced with what looks to be multi-faceted polycrystalline grains.

Cross sectional TEM images show a much improved interface from that observed on Si. Figure 85 shows an overview of the film and substrate. The BP thin film is comprised of heterogeneous polycrystalline grains of varying size. The far right portion of the image shows the interface region. At this magnification it is possible to see crystalline structure at the interface rather than amorphous material. Figure 86 shows a zoomed image of the first ~ 100 nm of the interface. Moving from left to right on the image shows the transition from the SiC to the BP film. The regular pattern visible in the single crystalline SiC is matched in the BP film. The polycrystalline nature of the film is more evident in this image; as the film progress in thickness, deviations in the epitaxy become more prevalent. The inset image in the top left is the Fourier Transform of the image on the right. The linear arrangements of the bright spots indicate direct alignment or epitaxy.

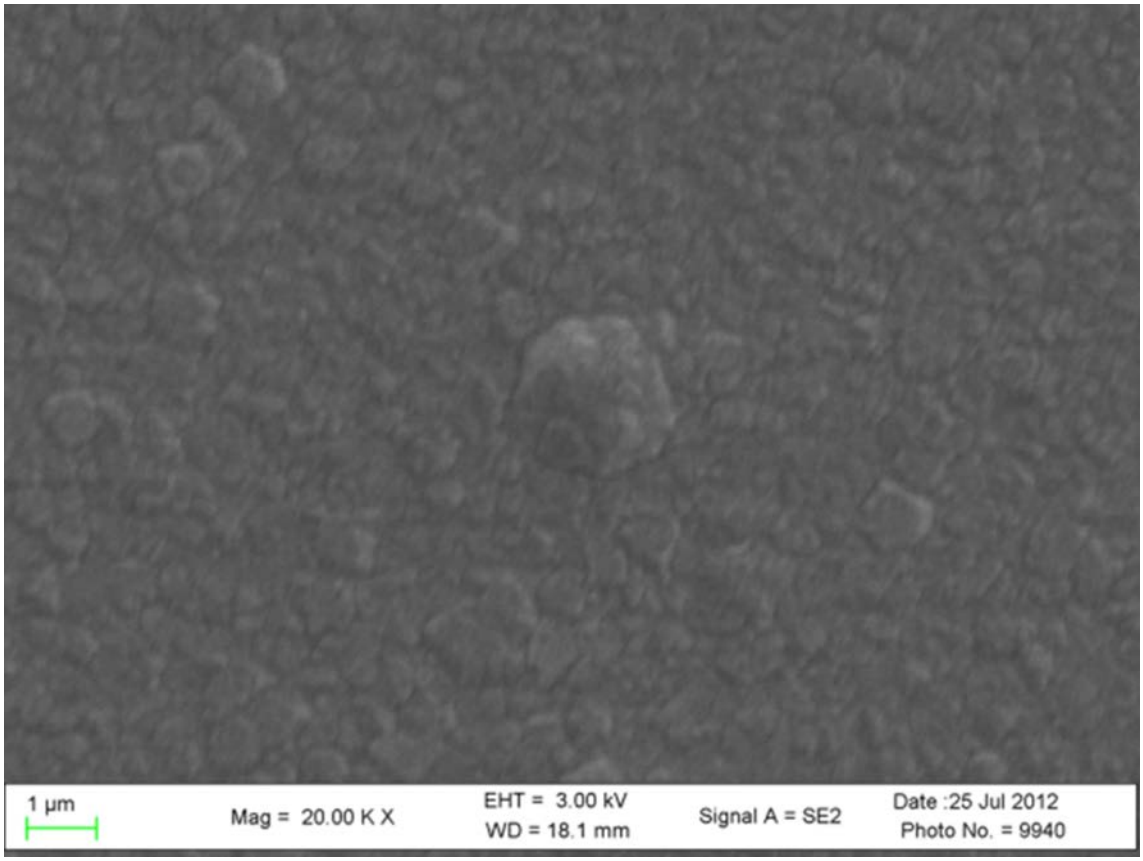

Figure 83. Surface SEM of BP on SiC. Shows continuous film with rough appearance

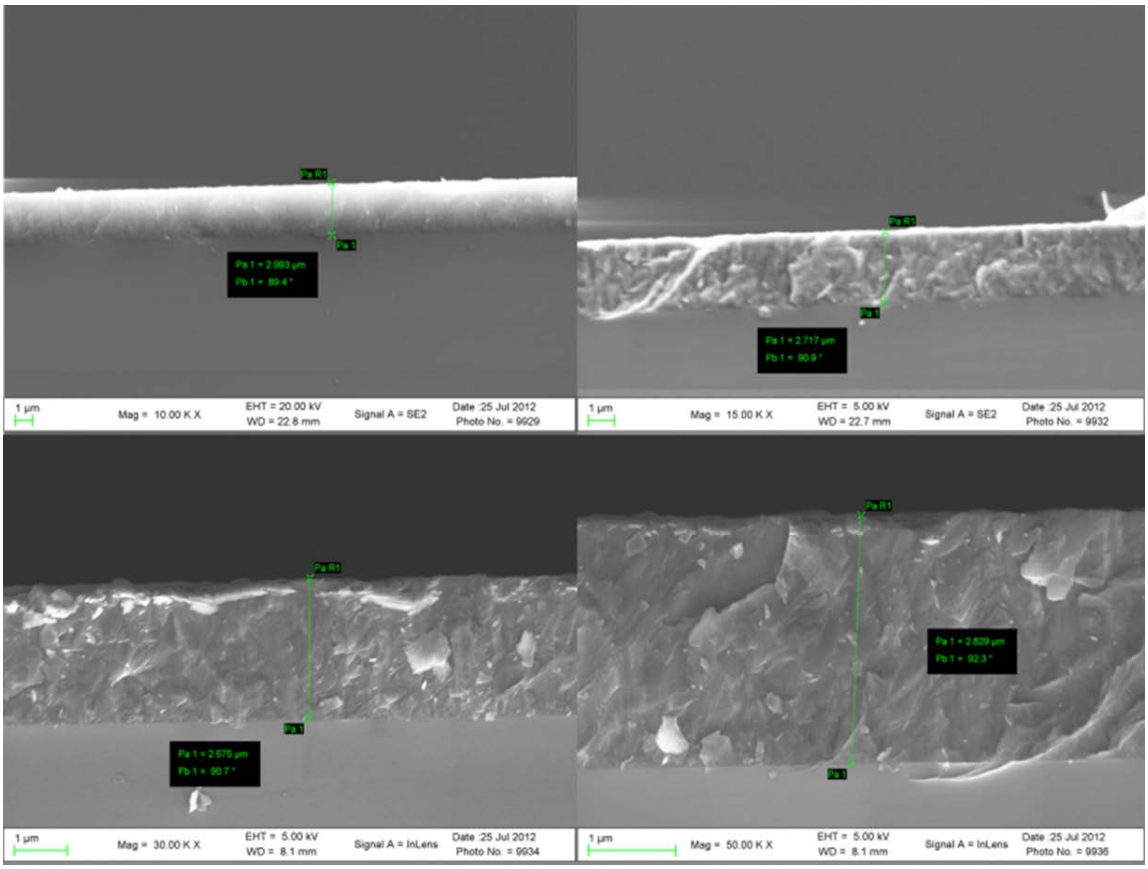

Figure 84. Cross sectional SEM of BP on SIC showing measured film thickness taken in 4 locations

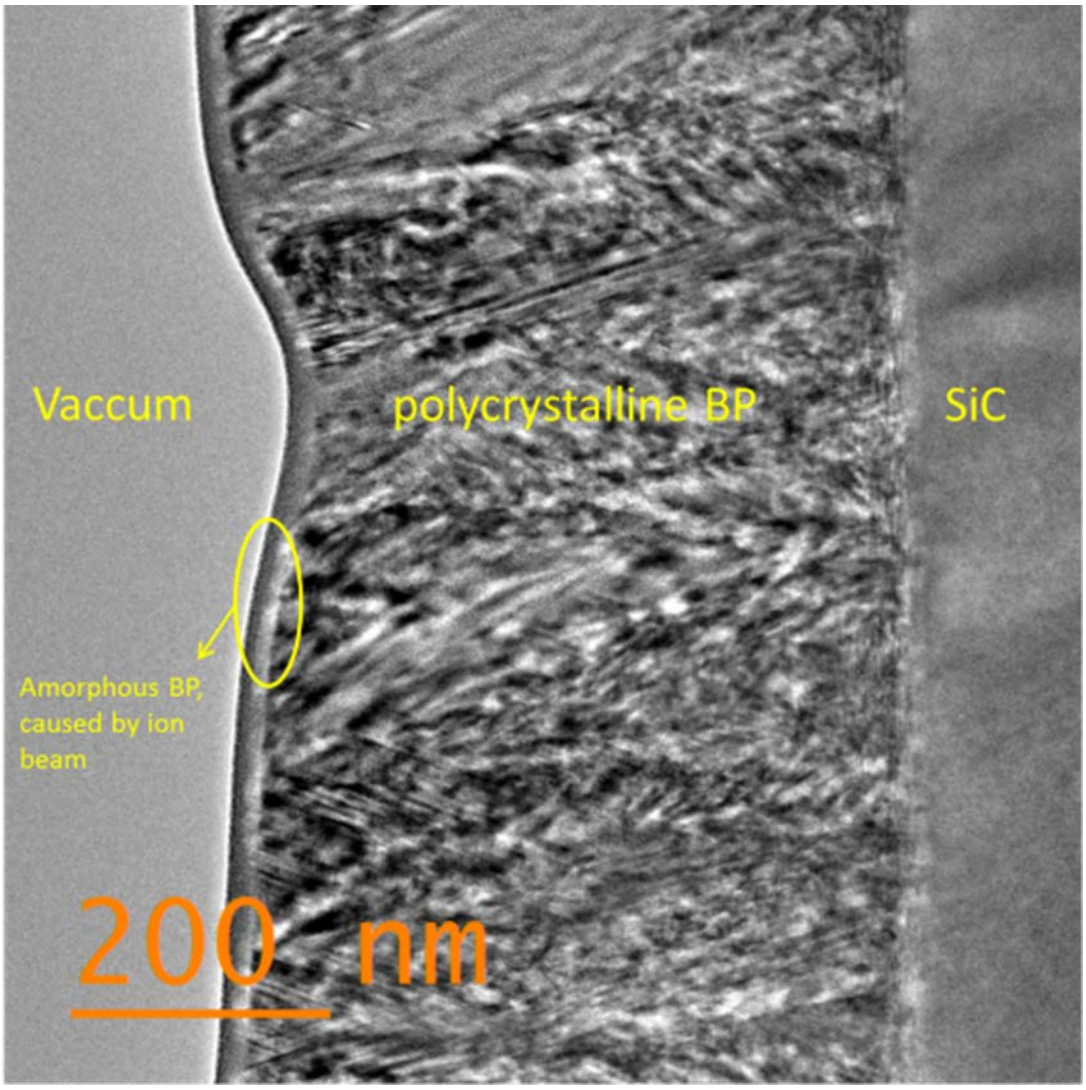

Figure 85. Cross-sectional TEM of BP on SiC. Showing polycrystalline grains and morphology at the film-substrate interface

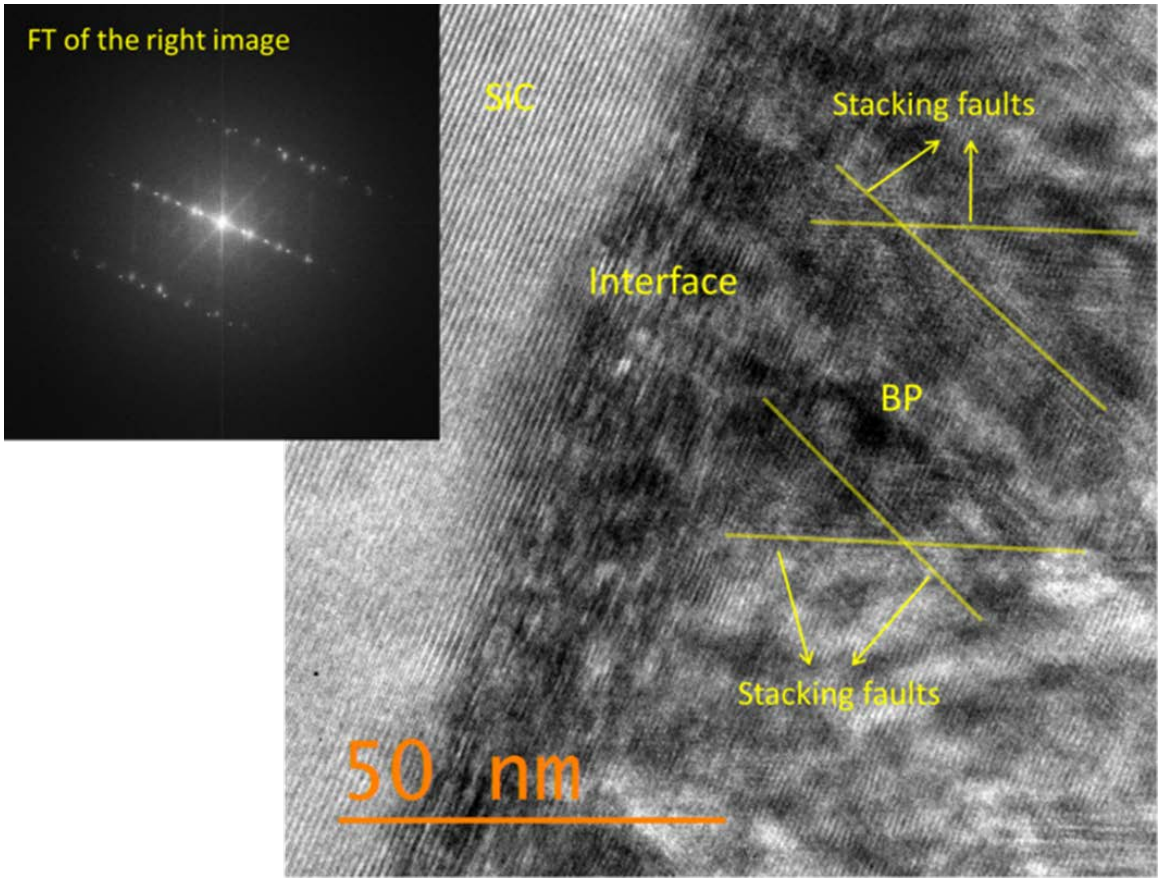

Figure 86. Zoomed TEM image of the BP-SiC interface. Showing Heteroepitaxy. The inset image is the Fourier Transform of the image on the right confirming epitaxial growth

The corresponding SAD patterns (Figure 87) indicate that there is strain at the interface evidenced by the contrast in size of the satisfied diffraction conditions of BP and SiC.

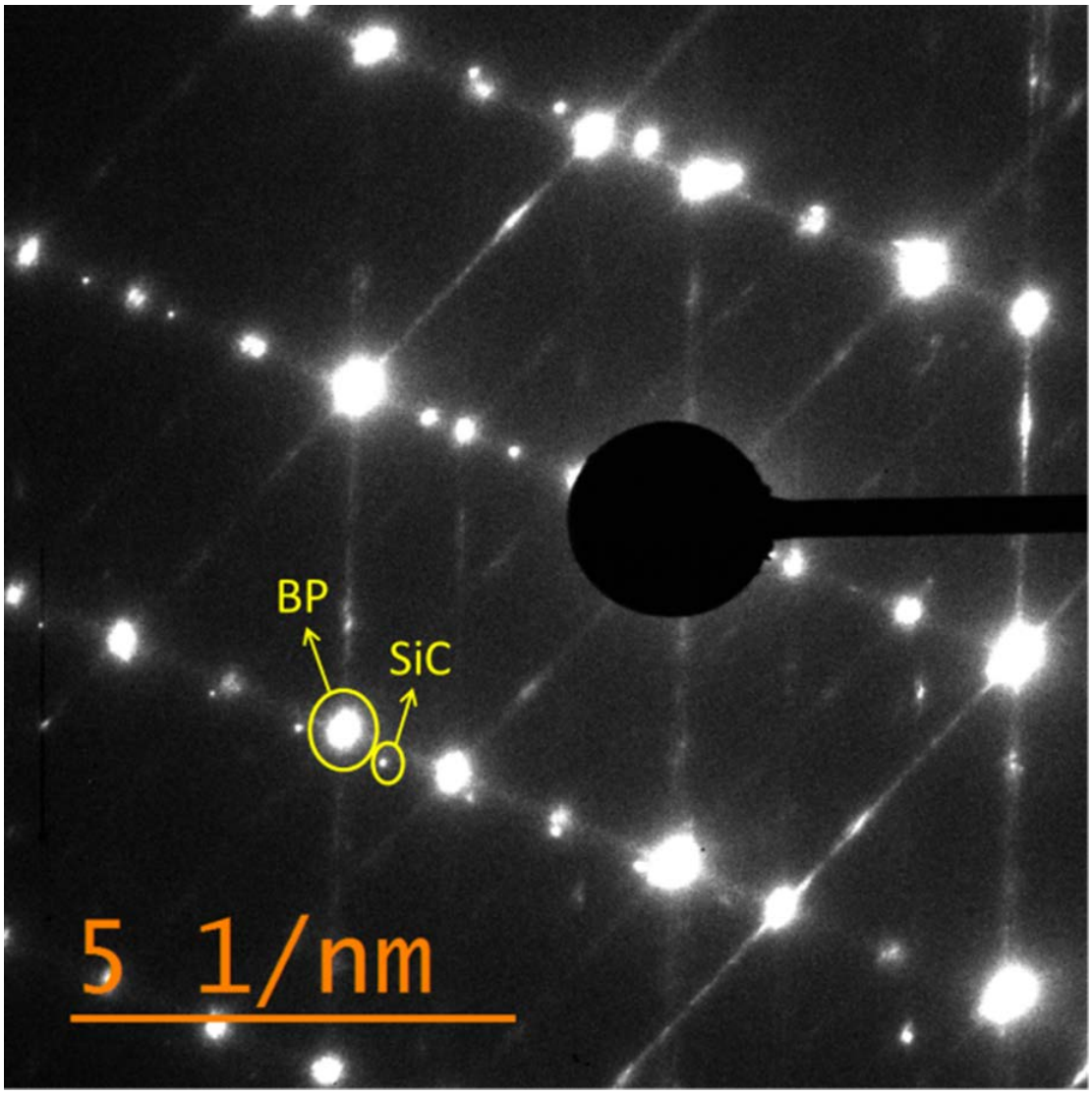

Figure 87. SAD pattern of BP on SiC. Indicating strain in the epitaxial film

Sample 45

While sample 31 did show epitaxial growth BP on SiC at the interface, there were considerable defects which led the film to deviate from continuing this epitaxial relationship tens of nanometers into growth. The bulk polycrystalline nature of the film is not ideal for signal conduction, therefore future experiments were designed to reduce defects and improve the bulk morphology of the BP film. In order to minimize variability in the system parameters, the growth condition of sample 45 were held constant from sample 31 with exception of temperature which was raised from 800° to 850°C. Theoretically, a higher temperature corresponds to a higher surface mobility for the B and P atoms on the SiC which should lead to improved layer-by-layer or Frank-van der Merwe growth. Sample 45 shows a total mass gain of 1.27 mg and a predicted film thickness of 2.72 um. The photograph of sample 45, shown in Figure 88, indicates the film covers the entire substrate and color variations can be observed in the middle of the film with several dark colored areas present. Figure 89 shows a series of surface SEM images at increasing magnification; image A is the lowest magnification and image D is the highest magnification. The higher magnification images depict a rough surface which has been consistently observed throughout the experiments conducted. TEM analysis of the BP-SiC interface shows higher order crystal quality and epitaxial growth. Figure 90 shows both the image and the resultant FT of the image. Some twinning is observed in the near interface region, but analysis of the d spacing from the atom arrangement show approximately 2-3% lattice distortion. This is slightly better than the 4% calculated mismatch between BP and SiC.

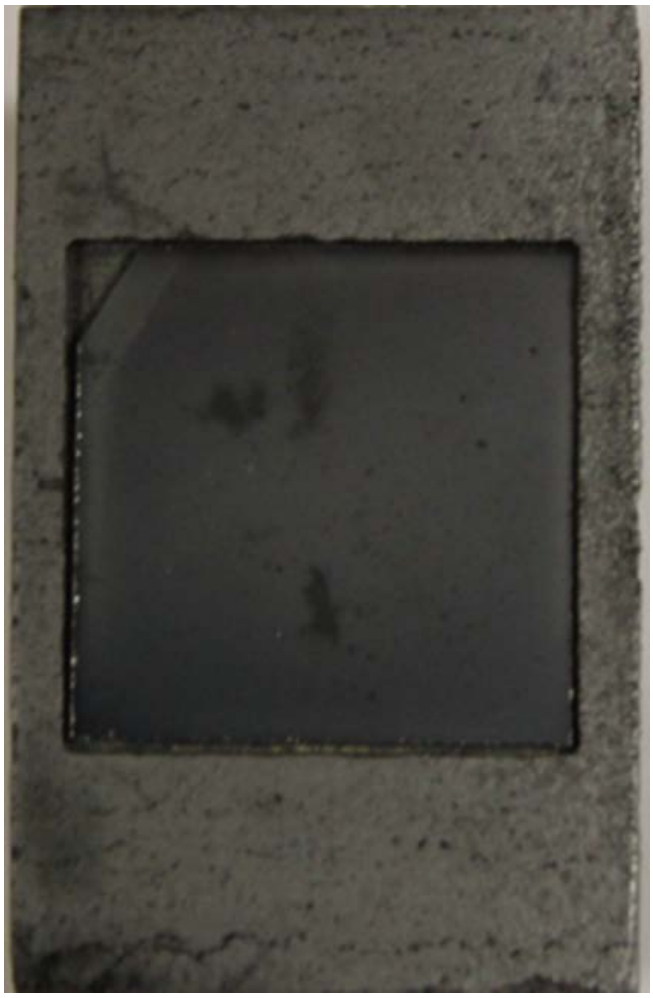

Figure 88. Photograph of sample 45, BP on SiC immediately post deposition. Sample shown in graphite susceptor

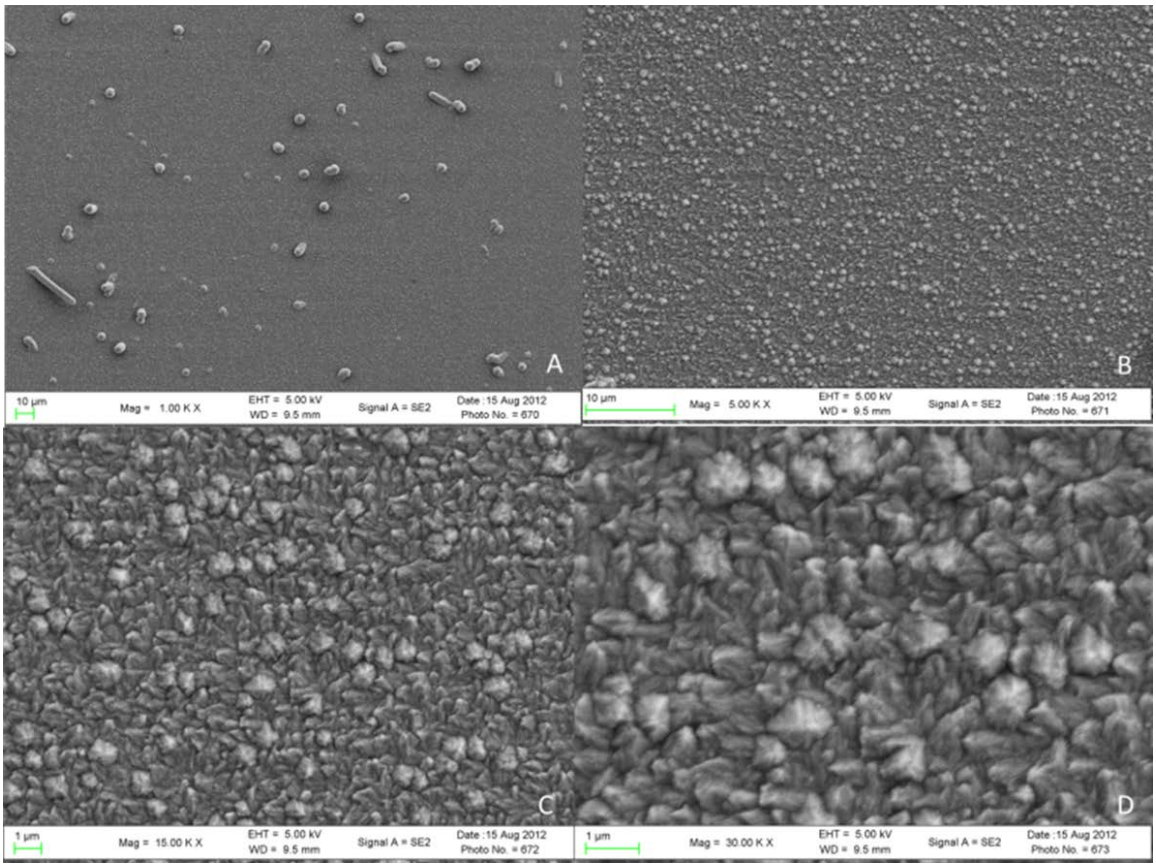

Figure 89. . Series of Surface SEM images of BP on SiC. Showing increases in magnification from 1KX (image A) to 30 KX (image D)

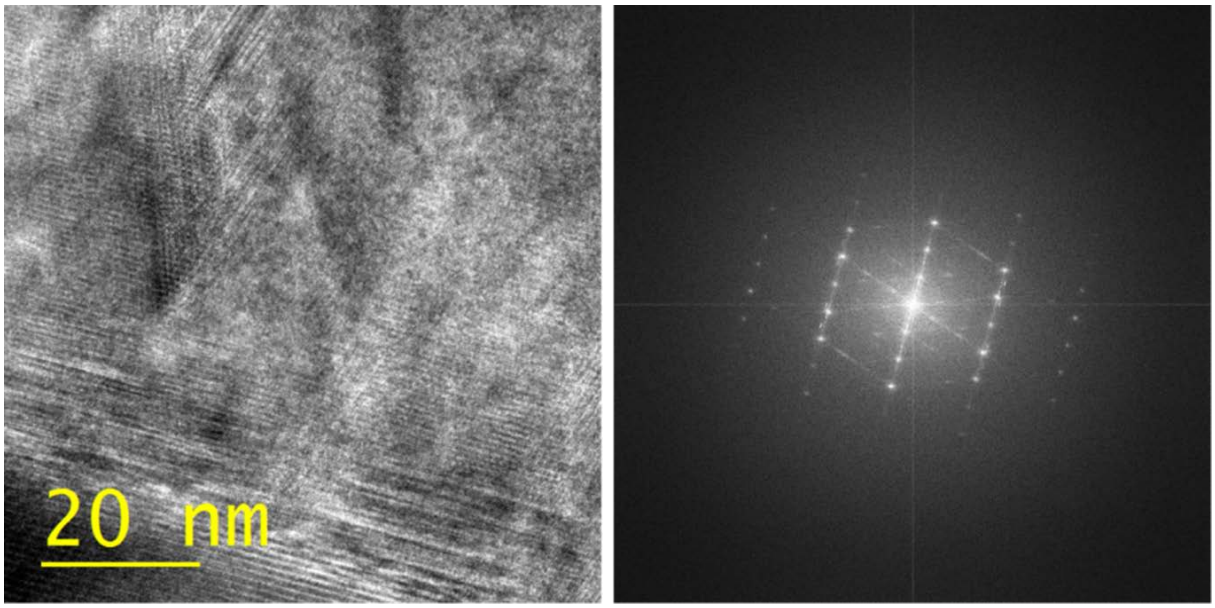

Figure 90. TEM image and FT of the interface of BP-SiC interface of sample 45

Based on the positive results of the interface analysis, additional images were obtained in the middle of the film as well as on the surface. Observations made from the middle of the film show a pure single crystalline morphology. The TEM image as well as the corresponding FT can be seen in Figure 91. Although not shown in the image, there is an approximate 7% distortion along the [100] but less than a 2% lattice distortion along the [110] and the [111] directions. Similar analysis methods on the surface of the film showed pure face centered cubic crystals with no observable no lattice distortions. This is shown in Figure 92. Some artifact can be observed in this subsample. The amorphous film at the very surface is not a result of the deposition, but rather consequences of the FIB and resulting Pt protection layer applied during sample preparation procedures.

The compartmentalized nature of the TEM analysis tends to belie the possible strain relief processes apparent. Up to this point, the concept of strain in the BP film has been passively noted. But sample 45 makes clear that the films morphology is changing as a function of film thickness. At the interface, epitaxial arrangement is observed with an approximate 2-3% lattice distortion along the [110]. The middle of the film shows FCC crystal structure with a slightly exaggerated distortion along the [100]. The surface of the film showed pure FCC with no appreciable distortions in the observed lattice. This variation in film crystal structure suggests that the induced strain from the inherent lattice mismatch is being slowly relieved throughout the thickness of this film. As the BP thickens, the strain is lessened and the [111] preferential growth direction is allowed to dominate. This observation is atypical in semiconductor heteroepitaxy.

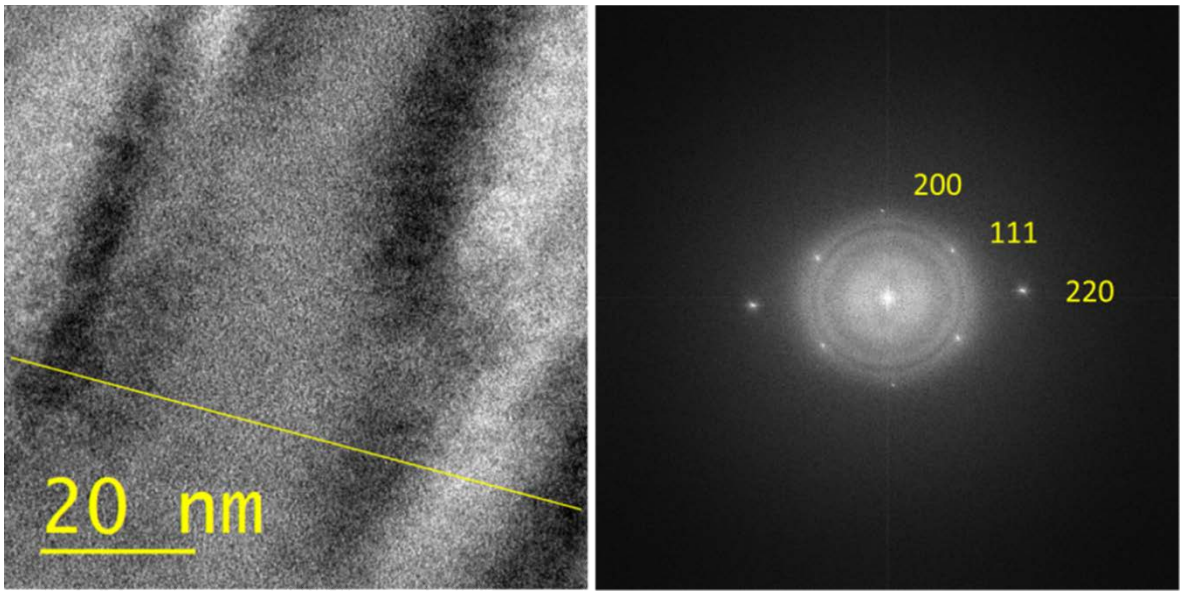

Figure 91. TEM image and corresponding FT from the middle portion of BP thin film sample 45. Showing single crystalline morphology

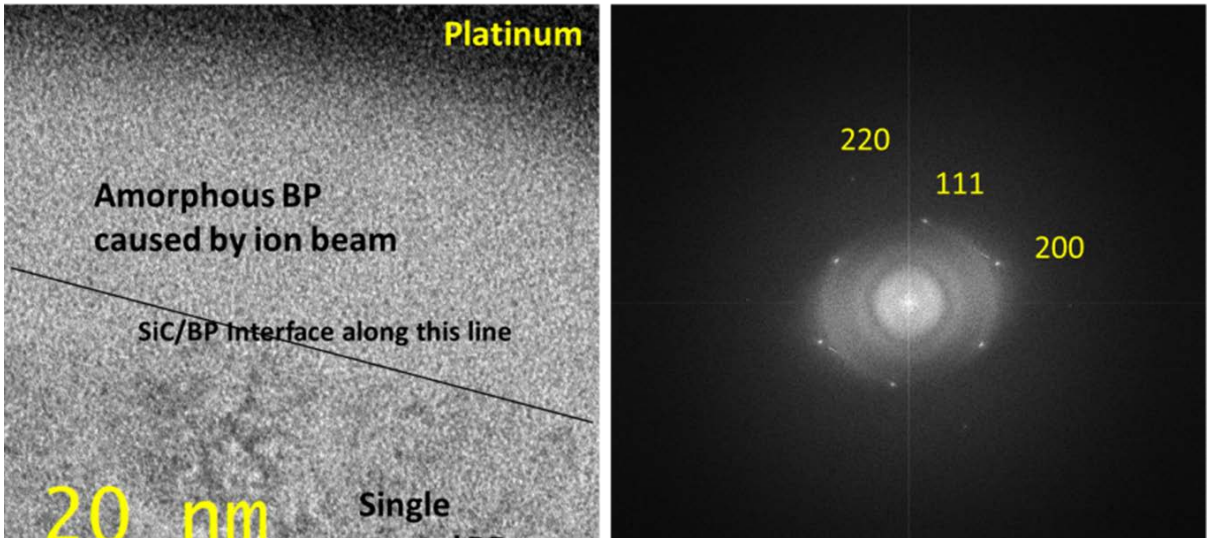

Figure 92. . TEM and corresponding FT of the surface of BP sample 45

The critical layer thickness can be determined to provide the approximate length of the epilayer to relieve the induced strain from the lattice mismatch, In order to approximate the strain, the lattice mismatch strain must first be determined. The lattice mismatch stain (f) is determined by the relationship of the relaxed lattice constants of both the epilayer and substrate according to the equation:

$$f \equiv \frac{a_s - a_e}{a_e}$$

where a_s and a_e are the relaxed lattice constants for the substrate and epitaxial layer respectively. Substituting the values for the BP-SiC system into the above equation, the lattice mismatch strain is between BP and 4H SiC is approximately -3.9%. In order to compensate for the hexagonal structure of the substrate, the α lattice constant of BP was multiplied by the√2/2. Using this information, the critical layer thickness h_c can now be accurately calculated using the equation below[63]:

$$h_c = \frac{a_e\left(1 - \frac{v_{pr}}{4}\right)\left[\ln\left(\frac{\sqrt{2}h_c}{a_e}\right) + 1\right]}{2\sqrt{2}\pi|f|(1 + v_{pr})}$$

where v_{pr} is Poisson's ratio and a_e is the relaxed lattice constant of the epitaxial layer or in this case lattice constant of BP. For the sake of this discussion, a numerical approximation will suffice; therefore In lieu of calculation, the critical layer thickness (h_c) can be approximated according to the equation below and will be used in further discussion:

$$h_c \approx \frac{a}{2f}$$

Where α is the relaxed lattice constant of BP and f is the calculated mismatch strain. Using this approximation, the critical layer thickness of a BP layer on SiC is 0.88 nm. This is the thickness expected to resolve the induced strain. Based on the TEM images shown previously for sample

45, strain relief through misfit dislocations is being observed at orders of magnitude greater thickness. This phenomenon is not completely understood, but the gradual release of induced strain over the total thickness of the film reduces the number of areas with high concentrations of strain induced defects thus giving a higher quality film.

Temperature Study

A series of successive experiments was performed in order to more thoroughly explore the effect of temperature on the quality of film deposition. In the study, all system parameters with the exception of temperature were held constant. Five depositions were performed beginning at 800 °C and increasing in 50 degree increments to a final temperature of 1000 °C. Table 9 shows the total system parameters for samples 80 through 84 comprising the temperature study.

Table 8. Total system parameter settings for experiments comprising the temperature study

Sample #	80	81	82	83	84
Pressure (torr)	630	630	630	630	630
Temp (°C)	850	800	900	950	1000
H_2 (sccm)	2500	2500	2500	2500	2500
PH_3 (sccm)	100	100	100	100	100
B_2H_6 (sccm)	20	20	20	20	20
Time of run (hr)	0.5	0.5	0.5	0.5	0.5
Predicted film thickness (µm)	2.33	2.80	2.33	2.16	0.98
mass change (mg)	1.09	1.31	1.09	1.01	0.46
Substrate material	4H-SiC 4° off axis	4H-SiC 4° off axis	4H-SiC 4° off axis	4H-SiC 4° off axis	4H-SiC 4° off axis
(111),(220) in counts on xrd	14.7:1	6.11:1	18.6:1	42.2:1	4.4:1
(111)/(220)	14.7	6.11	18.6	42.2	4.4
FWHM of 111 peak	0.17909	0.2558	0.17909	0.20467	0.10234
Growth Rate/hr	4.66	5.60	4.66	4.32	1.97
PH_3/B_2H_6	5	5	5	5	5

This table is similar to those previously presented but with one exception, rows 10, 11, and 12 address XRD analysis on this sample set. The details of XRD analyses performed on these samples will be discussed later in this chapter. Resultant data descriptions and discussions of the samples comprising the temperature study will include photographs of samples post deposition, XRD and TEM images, and SAD patterns when applicable. Surface SEM images and cross sectional images will only be included where needed because of the narrow focus of this experimental set and the limited value SEM images can provide in interface characterization.

Although sample 80 is the first sample in the temperature study, it is not the lowest temperature. The system parameters were controlled enough that the individual experiments are not

interdependent so the experiments need not be performed in any particular order. Complete system parameter settings can be seen in table 8. The average film thickness in microns was 2.33 with a corresponding mass change of 1.09 mg. Figure 93 shows photographs of the sample set sample post deposition. The sample appears to have a variety of surface features. Many samples have dark spots in the center of the samples surrounded by circular features. The exact cause of these visual features of the sample is unknown. Possible contributing factors include artifact from the tube during deposition or specific surface features of the individual wafers. Despite the differences in optical appearance, the growth rate is remarkably consistent with the exception of sample 84, which will be discussed later on. Raman spectra were obtained on all samples in the temperature. Figure 94 shows an overlay of the Raman spectra obtained on the samples. The BP peak is the most predominate peak shown at 828 cm^{-1} the small peak appearing at approximately 777 cm^{-1} is from the substrate of 4H SiC. As expected, the Raman spectra remain consistent and confirm these as BP films.

Throughout the course of the experimental set, XRD has been used to further confirm the growth of BP and to probe the orientation of the films. It has been noted that the epitaxial growth of BP on the (0001) surface of 4H- and 6H-SiC should produce BP of <111> orientation. In contrast, nucleation and growth from an amorphous layer, as seen for growths on silicon, yield a preferred orientation of <110>.

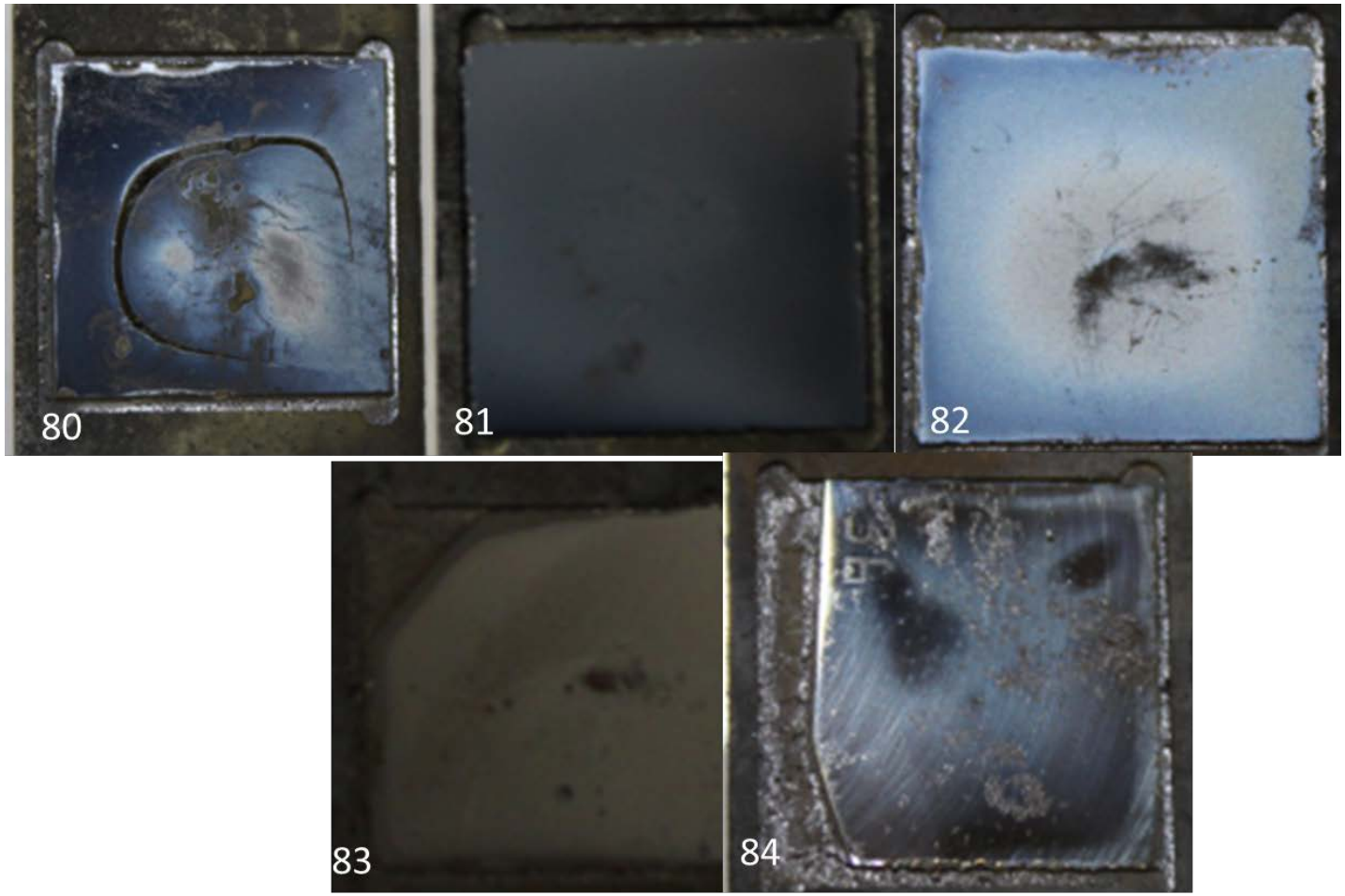

Figure 93. Photographs of Samples 80-84 post deposition

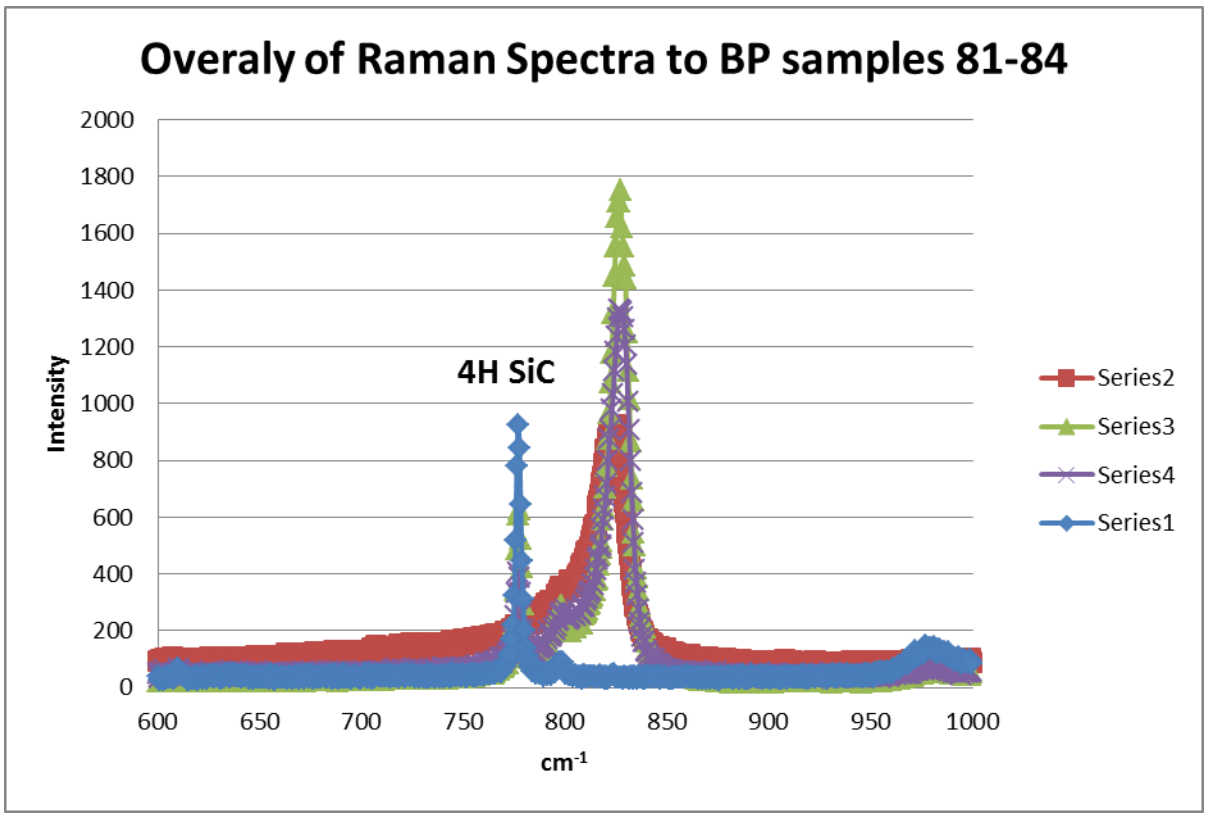

Figure 94. Raman Spectra of Temperature study samples

In most of the XRD patterns, two planes are observed; (111) and (220). Earlier focused studies suggest that changes in the diborane concentration appears to alter the preferred growth direction of the BP film as seen from comparison of data on samples 7, 13 and 21 shown in Figure 95. From the patterns it can be concluded that increased B_2H_6 concentration favors the (220) plane (indicative of growth in the <110> direction), while decreased B_2H_6 concentration favors the (111) plane. Additionally, twinning has the potential of rotating the crystal growth direction relative to the surface normal, and exposing (220) planes for diffraction.

Now that a relationship has been established between the film growth parameters and the XRD patterns, XRD patterns serve as a screening tool for propogation of epitaxially derived crystalline order in the films. BP films that exhibit high counts in the (111) are considered to have more epitaxially derived order than those with high counts in the (220). A simple metric developed to easily screen for this, was determination of the ratio of the (111) peak to the (220) peak of BP. The XRD spectra of the sample set are shown in Figure 94. The spectra are labeled according to corresponding sample and the peaks of interest are labeled according to direction of growth. Sample 80 in the top left has a corresponding ratio of (111) to (220) is 14.7. The XRD spectrum of sample 81 shows a ratio of 6.11:1 (111):(220). In sample 82, the ratio of the (111) to (220) is 18.6:1. A trend is beginning to emerge that indicates the (111):(220) scales with temperature. The data from Figure 83 supports this with a (111):(220) ratio of 42:1. The

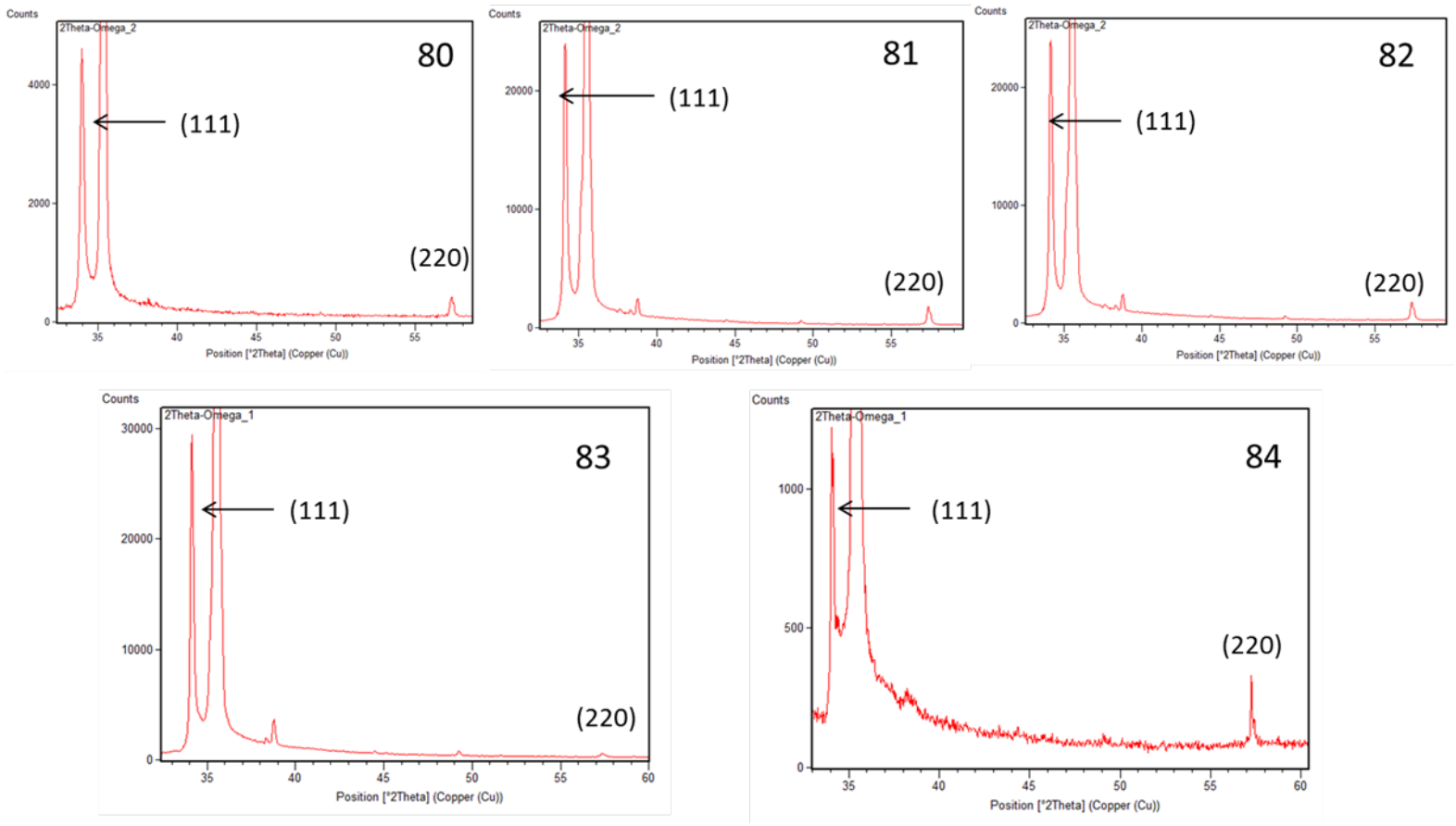

Figure 95. XRD of BP samples 80-84 temperature study Characteristic BP Peaks labled

progress of this trend is short lived because at 1000 °C the XRD ratio returns to near baseline. Sample 84 exhibits the lowest ratio of the sample set at 4.3:1, as well as the lowest mass gain at 0.46 mg. However, a notably higher (220) peak is observed. A graph of (111) :(220) vs. temperature is shown in Figure 96 and depicts a maximum in the ratio for BP deposition around 950 °C. One potential cause for lack of growth includes an inaccurate temperature measurement. Recall that the decomposition temperature of BP is 1030 °C and if the temperature were this high, BP would decompose rather than form a film. An inaccurate temperature measurement is doubtful; temperature readings were verified for accuracy and were well within 30 degrees. A more likely cause for lack of growth is gas depletion. Phosphine and Diborane readily crack at temperatures of 500 °C and at more than twice that temperature, they are very likely to react in the gas phase and be pumped away. The quartz reactor tube is not actively cooled, but relies on high velocity air moving across its exterior for cooling. This is not very efficient at removing heat, so at temperatures of 1000 °C the reactor tube is no longer behaving like a cold wall but is essentially a hot wall system. Diborane has the lower decomposition temperature and therefore should be more susceptible to decomposition away from the substrate surface. This would have the effect of decreasing the diborane concentration available for growth, which would reduce the growth rate and affect the (111)/(220) XRD ratios as well.

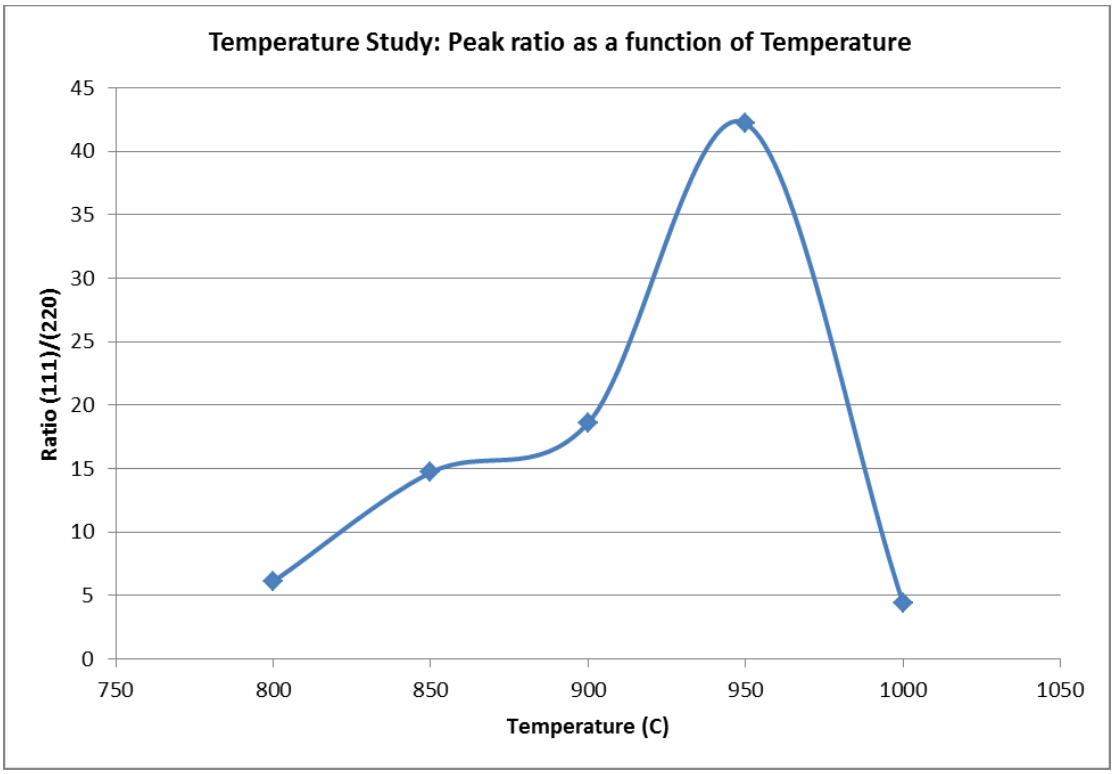

Figure 96. Ratio of BP orientations as a function of temperature

TEM Images of samples 80-84 correlate well with XRD analysis. All samples indicate heterepitaxy along the interface. Samples 82 and 83 indicate the presence of a localized amorphous region at the interface. This is peculiar in that the epitaxial relationship in these samples in unaffected by the amorphous region .The amorphous interface was not previously observed in any of the SiC samples. It is not clear at this time whether samples 82 and 83 are anomalous. Due to the extremely narrow field of view in TEM it is possible that the amorphous region is present in other samples, but was not present in the affected area. A collection of TEM images for samples 80-83 is shown in Figure 97. A SAD pattern was obtained on sample 83 at the interface. The corresponding diffraction conditions align and indicate epitaxy. The SAD is shown in Figure 98. No TEM images were obtained on sample 84 because the SEM showed no observable film, but rather randomly dispersed particles of varying sizes.

Summary

BP deposition on SiC substrates showed a remarkably higher order interface than those observed on Si Substrates. In most cases, BP deposition on SiC resulted in an epitaxial interface confirmed by TEM and SAD. Furthermore, XRD analysis evolved with further understanding of the relationship of the 4° off cut wafers used in the experiments. Compensation for the offcut was made in XRD scans resulting in more representative representation of the BP thin morphology. A temperature study was conducted to determine the ideal temperature for high quality BP deposition. Using the rations of the (111)/(220) peaks of the XRD as a function of temperature showed 950 °C temperature for highest thin film quality.

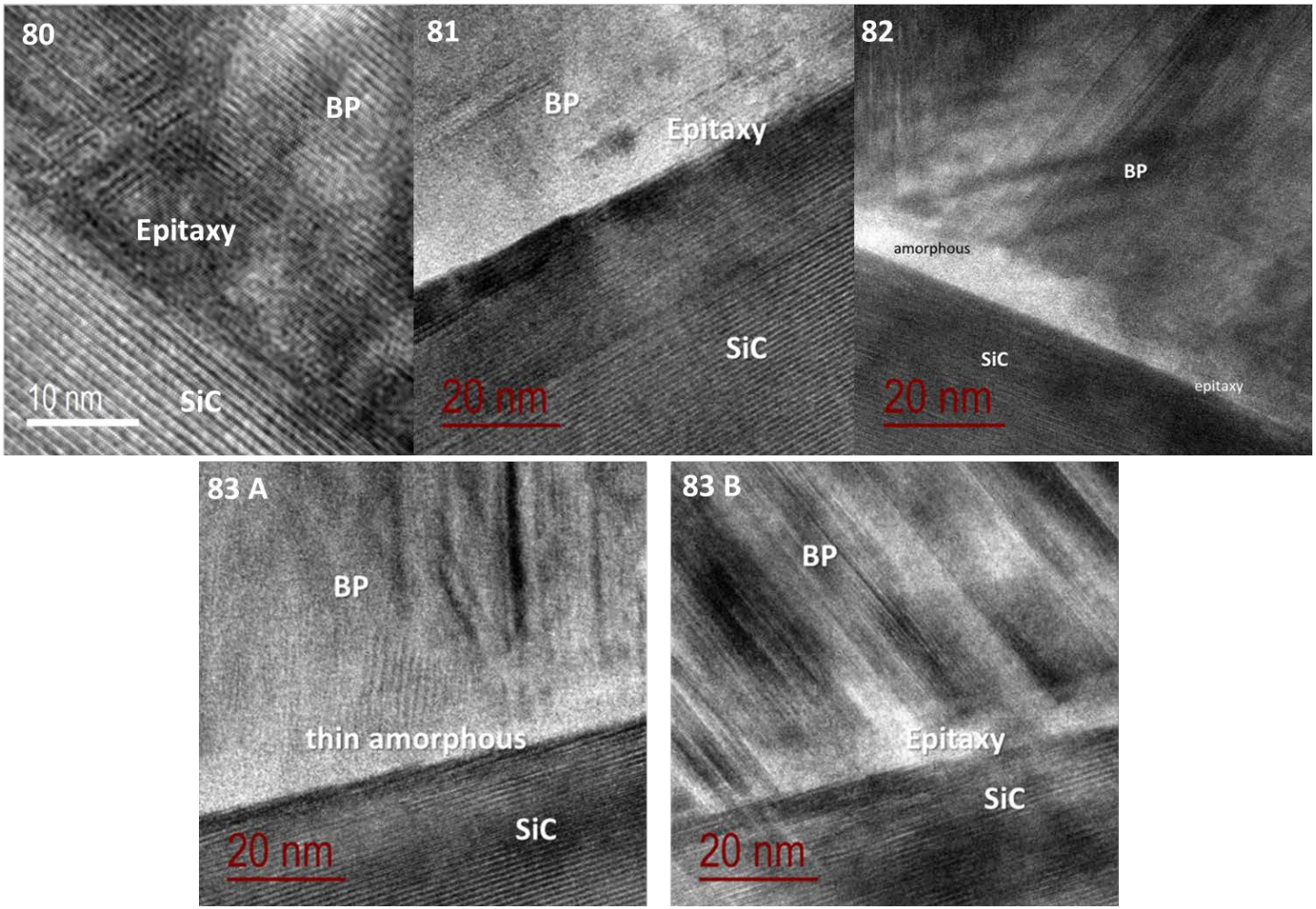

Figure 97. TEM images of samples 80-83. Showing heteroepitaxy

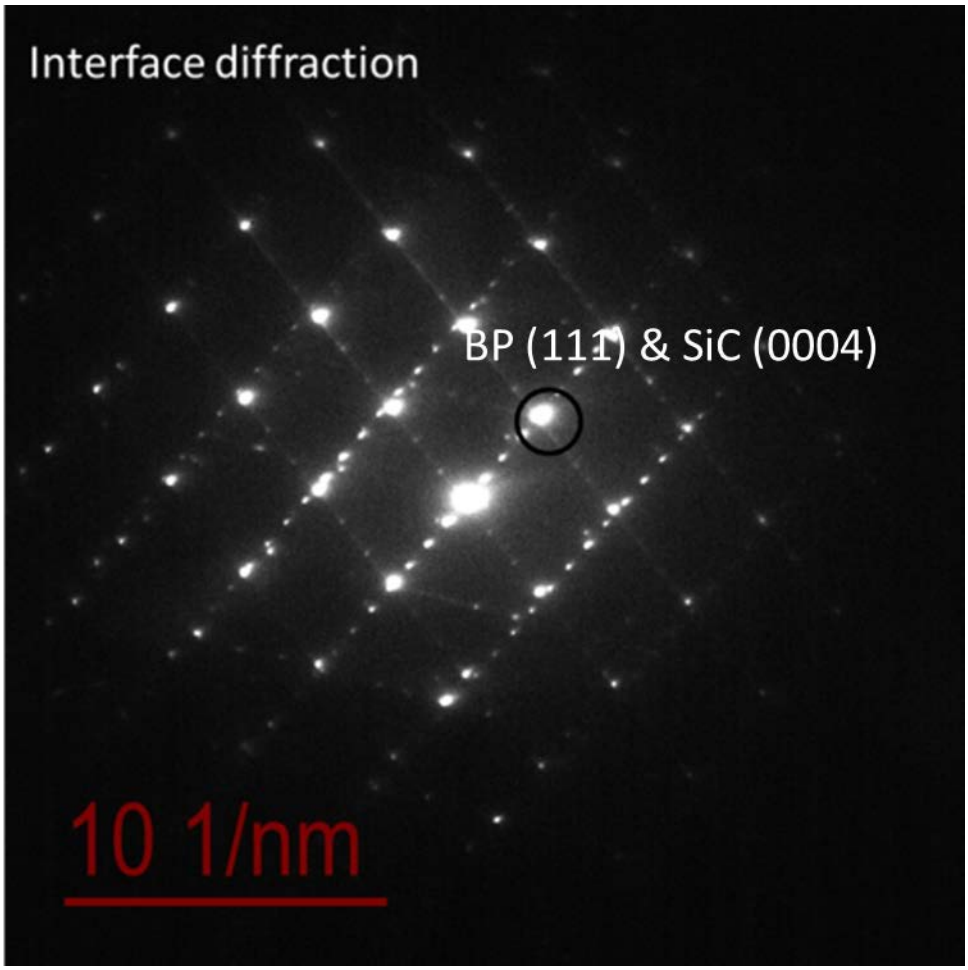

Figure 98. SAD pattern of BP sample 83. Despite amorphous BP at the interface, epitaxial relationship is unaffected

CHAPTER V
DISCUSSION AND FUTURE WORK

The current body of work regarding chemical vapor deposition of BP encompasses both establishing capability to deposit BP thin films and addressing some of the key issues surrounding BP as a viable material for device fabrication. A custom reactor was designed and fabricated for the chemical vapor deposition of semiconductor thin films. By the selection and use of high purity components and gases good thin film quality was achieved. Additionally, significant resources were invested into robust safety systems including the design and implementation of process automation tools and active sensors for the detection of hazardous gases outside of normal containment processes.

Initial experiments were focused on determining and establishing confidence in reactor design and operating procedures. For this reason, experiments were deposited on (001) Si substrates in order to leverage the plethora of literature of BP depositions on Si. Published literature results were compared to performed experiments to gauge agreement and provide reference for modifications to the reactor and operating procedures if necessary. Depositions on Si substrates were invaluable in preparing for future work with SiC substrates, as the Si work allowed the stoichiometric ratio of BP in the as grown films to be determined by EELS. TEM analysis and XRD analysis of BP films on Si substrate identified the preferential growth direction of BP and shaped the design of experiments on SiC.

BP depositions on SiC show that the reduced lattice mismatch between BP and SiC is sufficient to allow heteroepitaxial growth evidenced by TEM analysis of the BP-SiC interface. Upon the repeated demonstration of heteroepitaxial films of BP on SiC, focused studies were performed to

investigate film quality as a function of temperature. The criteria used to determine film quality was a combination of XRD and a high (111) to (220) ratio as well as TEM images and corresponding SAD patterns when applicable. The ideal temperature given a set of prescribed system parameters was found to 950° C. At this temperature a high (111) to (220) was observed via XRD analysis and TEM images showed a predominately heteroepitaxial interface. Additional focused studies we carried out to clarify the specific substrate conditions in order to optimize the quality of the deposited BP films. Two kinds of wafers were used in the surface study, a Si terminated epitaxial ready SiC wafer and a carbon terminated epitaxial –ready SiC wafer. Depositions were carried out on both sides of each wafer, resulting in 4 total samples to complete the data set. Recall from the materials chapter, that on SiC wafers the non-epitaxial ready side of the wafer is terminated opposite from the epitaxial side. Thus, the Si epi ready wafer's opposite side is a carbon terminated non polished surface and the carbon terminated epi-ready wafer has a Si terminated non polished surface. The majority of successful experiments were performed on the non epi-ready side of the Si epi-ready wafers; therefore no additional experiments were performed to examine this configuration. Experiments on the other three wafer configurations did not result in high film quality.

Compositional Analysis

Despite notable success is BP thin film growth on SiC substrates, more work is needed to leverage boron phosphide thin films as future candidates for device fabrication. The current work being described focused solely on morphological characteristics of the BP thin film. Success was defined as the observation of the epitaxial BP and single crystalline films. But the decision to focus on morphology was at the cost of perhaps equally important data, namely chemical composition. This work was not completely devoid of chemical compositional analysis, in that

EELS was useful in the determination of BP stoichiometry and the presented Raman spectra were used in confirmation of the presence of the BP molecule. However, a more in depth examination would be helpful to identify the potential trace contaminates in the as grown films. Techniques such as Auger electron spectroscopy (AES) and secondary ion mass spectrometry (SIMS) provide the resolution and sensitivity necessary to identify PPB level contaminates in the film. AES uses an electron beam to impinge on the surface of the sample. The key difference in Auger and other techniques is the detected species. AES detects the emitted Auger electron and not an X-Ray like the bulk of material characterization techniques. Advantages to AES are significant and include high surface specificity, probing depths between 5 and 100Å. This high lateral spatial resolution compared to EDS which can approach 300Å. Most importantly, the detection level for AES is in the ppm range. Like EDS, AES cannot detect hydrogen or helium. The Auger process works by the production of an inner atomic shell vacancy created by the primary electron beam. This vacancy, typically created in the K shell, is filled by an electron from an outer shell which is accompanied by the release of excess energy by emission of a valence electron. The electron transitions and the binding energy give way to an elemental specific electron energy emission. Application of AES sensitivity factors allows quantitative AES to be performed.

SIMS is a mass spectrometry based technique where an ion (Ar+, Cs+, O-) beam is rastered over the surface of a sample. As a result of the interaction between the ion beam and the sample, secondary ions from the sample surface and near surface region are ejected from the sample matrix. These ejected species are transported to the mass analyzer where their mass to charge ratio is ascertained. SIMS is not limited in the elements it can detect and magnetic sector instruments can resolve individual isotopes from hydrogen to uranium. Detection limits for SIMS

is in the sub ppb range, making it an excellent choice for trace detection and dopant quantification.

The most probable source of contamination in the reactor would be carbon that emanates from the graphite susceptor used to heat the substrate. To minimize this, the graphite susceptor was coated with BP prior to depositions to reduce the likelihood of free carbon; however, frequent experiments with the same susceptor cause visible degradation (Figure 99) which must be lost to the system during deposition experiments. The advantage to understanding the trace contaminates in the film can aid in understanding the electrical properties of the grown films. Trace impurities can serve as charge carriers that can influence the BP film to be p-type or n-type. Knowing the trace impurities together via a comprehensive electrical characterization, obtained by Hall Effects and resistivity can lead to a focused set of growth experiments designed to exacerbate desired electrical characteristic for device fabrication.

Defect Selective Etch

One of the fundamental analysis techniques used in this research effort is TEM. This method has been invaluable in examining the morphology of the BP film. One of the few concerns with this technique is sample size. Because TEM is able to resolve sub nanometer features in material, its sample area is very small. Therefore it is difficult to ascertain bulk defect density. Bulk defect density is important to know from a device fabrication standpoint, in that defects can cause a decrease in electron mobility. A probable solution to quantifying bulk defects is to employ defect selective etching (DSE). This techniques is used to identify defects like edge and screw dislocations and to estimate defect densities in samples. Areas with defects are more reactive with etchants than those without, causing pits to form over defects. The pits created for different

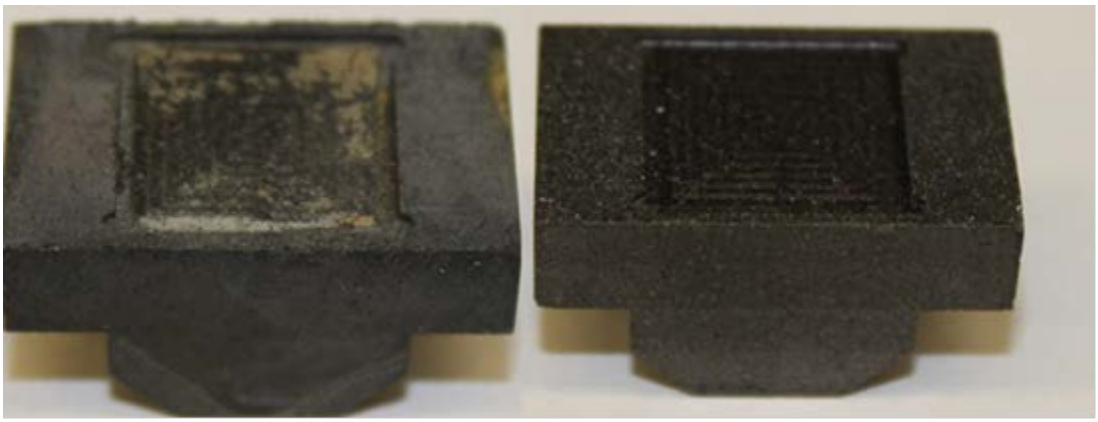

Figure 99. Photographs of used (left) and unused graphite suscepotrs

defects are materials specific and have different shapes. In silicon carbide, large hexagonal pits represent micropipes.[66] and medium sized hexagonal pits represent screw dislocations and small hexagonal pits represent threading edge dislocations. Furthermore, differences in strain energies and surface energies create different etch rates [68-70], thus causing different types of pits to form. At completion of the etch, the defects can be easily observed and counted. A density can then be determined by dividing by the sample area. There are some notable disadvantages to this technique, DSE is a destructive technique and the samples analyzed by this method are no longer suitable for future analysis. Also, in the case of BP, DSE requires the use of molten alkali salts which present unique challenges in preparation and handling. Despites these concerns, DSE can help provide a clearer picture of the bulk defect density and guide future deposition experiments to reduce or eliminate defects from the as grown films.

The degradation of growth at temperatures above 950°C also needs to be explored. Although reactor design, which incorporated a rail system to prevent direct contact the reactor walls was quite effective at producing BP growth over a wide range of conditions, there still is significant gas conduction heating of the reactor walls. Some method of cooling the walls may allow high growth temperatures to be achieved, thus improving film quality.

Conclusion

Boron phosphide is a challenging material to investigate. Its refractory nature and low thermal decomposition temperature combined with the difficult syntheses required to produce high quality material has limited its use as a group III-V semiconductor for device applications. However, the demonstrated success of BP deposition on SiC substrates presented in this work underscore the potential for boron phosphide to be used as a viable semiconductor in extreme environments. Further work is needed to develop the ability to control the desired electrical

characteristics of BP and maintain the high crystalline order required for useful devices. But with an ongoing push to introduce technology in environments once though not possible, continued development of boron phosphide is of significant importance to the field of advanced materials.

LIST OF REFERENCES

1. Jenkins, T. A Brief History of Semiconductors. *J. Physics Education.* **2005**, *40*, 430-439.
2. Hook, J.R. Hall; H.E. *Solid State Physics.* 1st ed.; Wiley: Hoboken, 1991.
3. Lukasiak, L.;Jakubowski, A. History of semiconductors. *J. Telecommunications and Information Technology.* **2010.** *1*,3-9.
4. Orton, J.W. *The story of Semiconductors;* Oxford University Press: USA, 2009.
5. Lojek, B. *History of Semiconductor Engineering;* Springer: Berlin, 2006.
6. Berger, L. *Semiconductor Materials;* CRC: New York 1997.
7. Sealy, B.J. Review of III-V Semiconductor Materials and Devices. *J. Institution of Electronic and Radio Engineers.* **1987.** *57,* S3-S12.
8. Garg, S. PhD. Dissertation, University of Cinicinatti, 1981.
9. Wilmesen, C.W. *Physics and Chemistry of III-V Semiconductor Interfaces;* Plenum: New York, 1985.
10. Hoddeson, L . Braun, E., Teichman, J. Weart, Spencer; *Out of the Crystal Maze. Chapters from the History of Solid State Physics;* Oxford: New York, 1992
11. Adachi, S. *Properties of Semiconductor Alloys;* Wiley: London, 2009.
12. Kelder,E.M.;Vander put, P.J.;Schooman,J. Thermochemical Data of Boron Subphosphide.*Thermochemica Acta* 1997, 306, 105-108
13. Shohno, K.; Ohtake, H. Crystal growth of Boron Monophosphide Using A B2H6-PH3-H2 System. Journal of Crystal Growth 1978, 45(4), 187-191.
14. Schroten, E.; Goossens, A.; Schoonman, J., Photo- and electroreflectance of cubic boron phosphide. Journal of Applied Physics 1998, 83 (3), 1660-1663.
15. Schmitt, J. O.; Edgar, L. J. H.; Liu, L.; Nagarajan, R.; Szyszko, T.; Podsiadlo, S.; Wojciech, G., Close-spaced crystal growth and characterization of BP crystals. In E-MRS 2004 Fall Meeting Symposia C and F, Stutzmann, M., Ed. 2005; Vol. 2, pp 1077-1080.
16. Kasap, S.O. Optoelectronics and Photonics. 2nd ed.; Prentice Hall: Hoboken, 2012.
17. Kumashiro Y., *Electric Refractory Materials*.; Marcel Dekker: New York, 2000.
18. Chu, T. L.; Gill, M.; Chu, S. S., Electrolytic Etching Of Boron Phosphide. *Journal of the Electrochemical Society* 1976, 123 (2), 259-262.
19. Williams, F. V.; Ruehrwein, R. A., The Preparation And Properties Of Boron Phosphides And Arsenides. *Journal of the American Chemical Society* 1960, 82 (6), 1330-1332.
20. Bartnitskaya, T. S.; Muchnik, S. V.; Lynchak, K. A.; Ivanchenko, L. A.; Timofeeva, II; Chernogorenko, V. B., Reactions Of Boron Phosphide With Ammonia And Nitrogen. *Inorganic Materials* 1978, 14 (2), 149-152.
21. Stone, B.; Hill, D., Semiconducting Properties Of Cubic Boron Phosphide. *Physical Review Letters* 1960, 4 (6), 282-284.
22. Fomichev, V. A.; Zhukova, II; Polushin.Ik, Investigation Of Energy Band Structure Of Boron Phosphide By Ultra-Soft X-Ray Spectroscopy. *Journal of Physics and Chemistry* of Solids 1968, 29 (6), 1025-&.
23. Chu, T. L.; Jackson, J. M.; Hyslop, A. E.; Chu, S. C., Crystals And Epitaxial Layers Of Boron Phosphide. *Journal of Applied Physics* 1971, 42 (1), 420-424.

24. Takigawa, M.; Hirayama, M.; Shohno, K., Heteroepitaxial Growth Of Lower Boron Phosphide On Silicon Substrate Using Ph3-B2h6-H2 System. *Japanese Journal of Applied Physics* 1973, 12 (10), 1504-1509.
25. Iniewski, K., Semiconductor radiation detection systems. CRC Press/Taylor & Francis: Boca Raton, FL, 2010; p xii, 388 p.
26. Lutz, G., Semiconductor radiation detectors : device physics. Springer: Berlin ; New York, 1999; p xi, 353 p.
27. H. Moissan, Compt. r m d . , 113, 624 (1891).
28. M. Besson, ibid., 113, 78 (1891).
29. Popper, P.; Ingles, T. A., Boron Phosphide, A Iii-V Compound Of Zinc-Blende Structure. *Nature* 1957, 179 (4569), 1075-1075
30. Wang, C. C.; Cardona, M.; Fischer, A. G., Preparation, Optical Properties, and Band Structure of Boron Monophosphide. Rca Rev 1964, 25 (2), 159-167.
31. Vickery, R. C., Synthesis Of Boron Phosphide And Nitride. Nature 1959, 184 (4682), 268-268.
32. Takigawa, M.; Hirayama, M.; Shohno, K., Heteroepitaxial Growth Of Lower Boron Phosphide On Silicon Substrate Using Ph_3-B_2h_6-H_2 System. *Japanese Journal of Applied Physics* 1973, 12 (10), 1504-1509.
33. Nishinaga, T.; Ogawa, H.; Watanabe,H.; Tetsyuya, A. Vapor Growth Of Boron Monophosphide Using Open And Closed Tube Processes. *J. Crystal Growth*., 13/14, 346-349.
34. Kumashiro, Y.; Okada, Y.; Gonda, S., Crystal-Growth Of Thick Wafers Of Boron Phosphide. Journal of Crystal Growth 1984, 70 (1-2), 507-514.
35. Kumashiro, Y.; Yao, T.; Gonda, S., Crystal-Growth Of Boron Phosphide By High-Pressure Flux Method. *Journal of Crystal Growth* 1984, 70 (1-2), 515-518.
36. Kumashiro, Y.; Okada, Y., Schottky-Barrier Diodes Using Thick, Well-Characterized Boron Phosphide Wafers. *Applied Physics Letters* 1985, 47 (1), 64-66.
37. Kumashiro, Y.; Hirabayashi, M.; Koshiro, T.; Okada, Y., Thermoelectric Properties Of Boron Phosphide. *Journal of the Less-Common Metals* 1988, 143 (1-2), 159-165.
38. Kumashiro, Y.; Mitsuhashi, T.; Okaya, S.; Muta, F.; Koshiro, T.; Takahashi, Y.; Mirabayashi, M., Thermal-Conductivity Of A Boron Phosphide Single-Crystal Wafer Up To High-Temperature. *Journal of Applied Physics* 1989, 65 (5), 2147-2148.
39. Kumashiro, Y., Refractory Semiconductor Of Boron Phosphide. Journal of Materials Research 1990, 5 (12), 2933-2947.
40. Kumashiro, Y.; Hirabayashi, M.; Takagi, S., Boron Phosphide As A Refractory *Semiconductor*. 1990; Vol. 162, p 585-594.
41. Kumashiro, Y.; Yokoyama, T.; Nakamura, J.; Matsuda, K.; Yoshida, H.; Takahashi, J., Thermoelectric Properties Of Boron And Boron Phosphide Film. 1992; Vol. 242, p 629-635.
42. Kumashiro, Y.; Okada, Y.; Okumura, H., Isotope Effects On Boron Phosphide Single-Crystal Wafers. *Journal of Crystal Growth* 1993, 132 (3-4), 611-613.

43. Kumashiro, Y.; Matsumoto, M.; Yoshizawa, H., Heteroepitaxial Growth Of Boron Phosphide Single Crystal On Sapphire Single Crystal. In Proceedings of the 11th International Symposium on Boron, Borides and Related Compounds, Uno, R.; Higashi, I., Eds. 1994; Vol. 10, pp 160-163.
44. Kumashiro, Y.; Yokoyama, T.; Nakamura, J.; Takahashi, J., Semiconducting Properties Of Boron Phosphide Thin Films By Mbd Process. In Proceedings of the 11th International Symposium on Boron, Borides and Related Compounds, Uno, R.; Higashi, I., Eds. 1994; Vol. 10, pp 168-169.
45. Kumashiro, Y.; Yoshizawa, H.; Shirai, K., Preparation of Rhombohedral Boron Phosphide Wafer By Cvd Process. In Proceedings of the 11th International Symposium on Boron, Borides and Related Compounds, Uno, R.; Higashi, I., Eds. 1994; Vol. 10, pp 166-167.
46. Kumashiro, Y.; Yokoyama, T.; Sakamoto, T.; Fujita, T., Preparation and electrical properties of boron and boron phosphide films obtained by gas source molecular beam deposition. *Journal of Solid State Chemistry* 1997, 133 (1), 269-272.
47. Kumashiro, Y.; Yokoyama, T.; Sato, A.; Ando, Y., Thermoelectric properties of boron and boron phosphide CVD wafers. *Journal of Solid State Chemistry* 1997, 133 (1), 314-321.
48. Kumashiro, Y.; Yoshizawa, H.; Yokoyama, T., Epitaxial growth of rhombohedral boron phosphide single crystalline films by chemical vapor deposition. *Journal of Solid State Chemistry* 1997, 133 (1), 104-112.
49. Kumashiro, Y.; Yokoyama, T.; Ando, Y.; IEEE, Thermoelectric properties of boron and boron phosphide CVD wafers. 1998; p 591-594.
50. Kumashiro, K.; Hirata, K.; Sato, K.; Yokoyama, T.; Aisu, T.; Ikeda, T.; Minaguchi, M., Thermoelectric properties of boron and boron phosphide films. *Journal of Solid State Chemistry* 2000, 154 (1), 26-32.
51. Kumashiro, Y.; Sato, K.; Chiba, S.; Yamada, S.; Tanaka, D.; Hyodo, K.; Yokoyama, T.; Hirata, K., Preparation of boron and boron phosphide films by photo- and thermal chemical vapor deposition processes. *Journal of Solid State Chemistry* 2000, 154 (1), 39-44.
52. Kumashiro, Y.; Yokoyama, T.; Sato, K.; Ando, Y.; Nagatani, S.; Kajiyama, K., Electrical and thermal properties of B12P2 wafers. *Journal of Solid State Chemistry* 2000, 154 (1), 33-38.
53. Kumashiro, Y.; Nakamura, K.; Doi, Y.; Hirata, K.; Yokoyama, T.; Sato, K., The preparation of B-Sb thin films by molecular flow region PVD process. *Journal of Crystal Growth* 2002, 237, 1531-1535.
54. Kumashiro, Y.; Enomoto, T.; Sato, K.; Abe, Y.; Hirata, K.; Yokoyama, T., Thermoelectric properties of photo- and thermal CVD boron and boron phosphide films. *Journal of Solid State Chemistry* 2004, 177 (2), 529-532.

55. Kumashiro, Y.; Nakamura, K.; Sato, K.; Ohtsuka, M.; Ohishi, Y.; Nakano, M.; Doi, Y., The properties of B-Sb thin films prepared by molecular flow region PVD process. *Journal of Solid State Chemistry* 2004, 177 (2), 533-536.
56. Kumashiro, Y.; Ozaki, S.; Sato, K.; Kataoka, Y.; Hirata, K.; Yokoyama, T.; Nagatani, S.; Kajiyama, K., The preparation and thermoelectric properties of molten salt electrodeposited boron wafers. *Journal of Solid State Chemistry* 2004, 177 (2), 537-541.
57. Kumashiro, Y.; Nakamura, K.; Enomoto, T.; Tanaka, M., Preparation and thermoelectric properties of BP films on SOI and sapphire substrates. *Journal of Materials Science-Materials in Electronics* 2011, 22 (8), 966-973.
58. Fitzsimmons, M., Pynn,R . Fabrication of boron-phosphide neutron detectors ; LA-UR--97-1228; NTIS: Los Alamos NM, 1997.
59. Benedict, M.; Pigford, T. H.; Levi, H. W., *Nuclear chemical engineering*. 2d ed.; McGraw-Hill: New York, 1981; p xv, 1008 p.
60. Gibson, D. R.; Waddell, E. M.; Wilson, S. A. D.; Lewis, K. L., Ultradurable Phosphide-Based Antireflection Coatings For Sand And Rain Erosion Protection. *Optical Engineering* 1994, 33 (3), 957-966.
61. Boland, J. F.; American Nuclear Society.; U.S. Atomic Energy Commission., Nuclear reactor instrumentation (in-core). Gordon and Breach: New York,, 1970; p xiii, 229 p.
62. Yugo, S.; Kimura, T., Thermoelectric-Power of Boron Phosphide At High-Temperatures. Physica Status Solidi a-Applied Research 1980, 59 (1), 363-370.
63. Ayers, J. E. *Heteroepitaxy of Semiconductors*, CRC Press: Boca Raton, 2007.
64. Freund, L.B.; Suresh,S. *Thin Film Materials: Stress, Defect Formation and Surface Evolution*, Cambridge University Press: New York, 2003.
65. Pierson,H. Handbook of Chemical Vapor Deposition, 2nd ed: Noyes Pub: Norwich, 1999
66. Li, Guoliang. Growth and Properties of Boron Phosphide Films on Silicon Carbide. Ph.D. Dissertation, University of Tennessee, 2013.
67. Locke, C. Stress-Strain Management of Heteroepitaxial Polycrystalline Silicon Carbide Films. Ph.D. Dissertation, University of South Florida, 2011.
68. Sakwe, S.A.;Herro,Z.G.; Wellmann;J. Development of a KOH Etching Furnace with Absolute In-Situ Temperature Measurement Capability. Mater. Science Forum 483-485
69. Sakwe,S.A.; Muller,R.; Wellman P.J. Optimization of KOh Etching Parameters for Quantitative defect recognition in n-and p- type doped SiC. Journal of Crystal Growth 2006, 289 520-526.
70. Zhao, F.; Daniels, K.;Laney, Z.; Sudarshan,T.A Novel Technique For Crystallagraphic Study of SiC Materials. ISRDS, College Park MD; December 9-11, 2009.
71. http://nano-physics.pbworks.com/w/page/12296664/Group%203
72. Wyckoff,W.G. Crystal Structures,Interscience: New York, 1963.
73. http://neon.mems.cmu.edu/skowronski/Silicon%20carbide%20unit%20cell.htm.
74. http://www.baycarbon.com/SiCCoating.htm
75. http://www.horiba.com/fileadmin/uploads/Scientific/Documents/Raman/T64000.pdf

76. http://www.pyrometer.com/MicroTherm.html
77. Geochemical Instrumentation and Analysis. http://serc.carleton.edu/research_education/geochemsheets/techniques/SEM.html (accessed Jan 29, 2013)

APPENDIX

APPENDIX A

Attachment 1. Appendix A.pdf

APPENDIX B

Si and SiC Wafer Cleaning Procedures

Si wafers exposed to ambient atmosphere for greater than 10 hours react with atmospheric oxygen to form surface oxides thicknesses of 1 Å. These SiO_2 compounds prohibit epitaxial growth of films on the wafers and influence electrical properties of the wafers making successful device fabrication unlikely. Prior to chemical vapor deposition of the wafers, it is necessary to remove the native oxides using common wet chemical methods. The most popular method in surface oxide removal is to use hydrogen fluoride (HF). HF solutions are preferred because they preferentially attack the oxide and leave the remaining bare silicon intact. HF is typically diluted with deionized (DI) water in order to slow down the etch rate of SiO_2, thereby ensuring better etch uniformity. Typical dilution ratios range from 1:1 H_2O:HF to 100:1 H_2O:HF. For certain critical etches, the HF may be diluted with ammonium fluoride (NH_4F) to promote more uniform liquid coverage on the Si surface; it is then called a Buffered Oxide Etch (BOE). Since HF removes the SiO_2, it leaves a bare Si surface when the etch is taken to completion. This bare Si surface is hydrophobic and is very susceptible to particle deposition.

The procedure employed in this work used a BOE. Once the wafer is cut to size, it is placed in HPLC grade acetone and sonicated for five minutes. The wafer is then rinsed with DI water and placed back in the sonicator in DI water for an additional five minutes. Upon completion of the DI water sonication, the wafer is placed in a 1:6 solution of HF and NH_4F. The wafer is allowed to soak for 2 minutes and then re-rinsed with fresh DI

water. A visual inspection of the wafer surface is performed. A successful etch is indicated when the DI water beads on the wafer surface. If this is not observed, the process is repeated until water is observed repelling off the wafer surface. The wafer is now ready to be placed in the reactor.

Wafer cleaning methods primarily developed for silicon are not directly applicable to SiC wafers. The surface of the Silicon and SiC wafers differ enough that alternative cleaning methods were explored. The current SiC wafer cleaning procedure very closely followed the previously described method for silicon wafers. The main difference being the elimination of the ammonium fluoride step in the etch procedure. The current method employs a 5 minute sonication in high purity acetone, a rinse with DI water, and a soak in a 50% HF solution for five minutes. Upon completion of the dip in dilute HF, the wafer is re-rinsed with DI water to ensure sheeting is observed. The wafer is then dried in flowing high purity N_2 and then placed in the reactor where an inert atmosphere is placed over the wafer.

After the wet etches are completed and the prepared wafers are placed in the reactor a final dry oxide etch is performed just prior to deposition; as some oxide could re-form on the wafer surface because of trace oxygen in the reactor. In order to remove these potential oxides, the wafers are heated to 1000 °C in a hydrogen atmosphere for 20 minutes. At completion of the hydrogen etch, the wafers are cooled in the reducing atmosphere to the selected deposition temperature where the precursor gases are introduced and BP deposition commences.

APPENDIX C

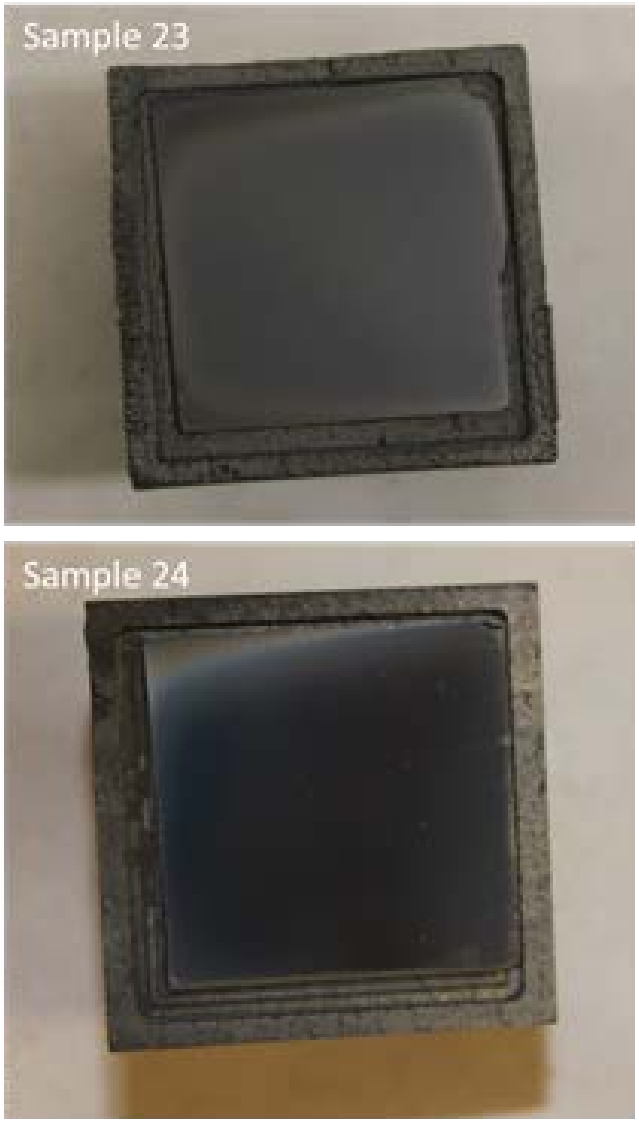

Figure 100. Photographs of sample 23 24 immediately post deposition

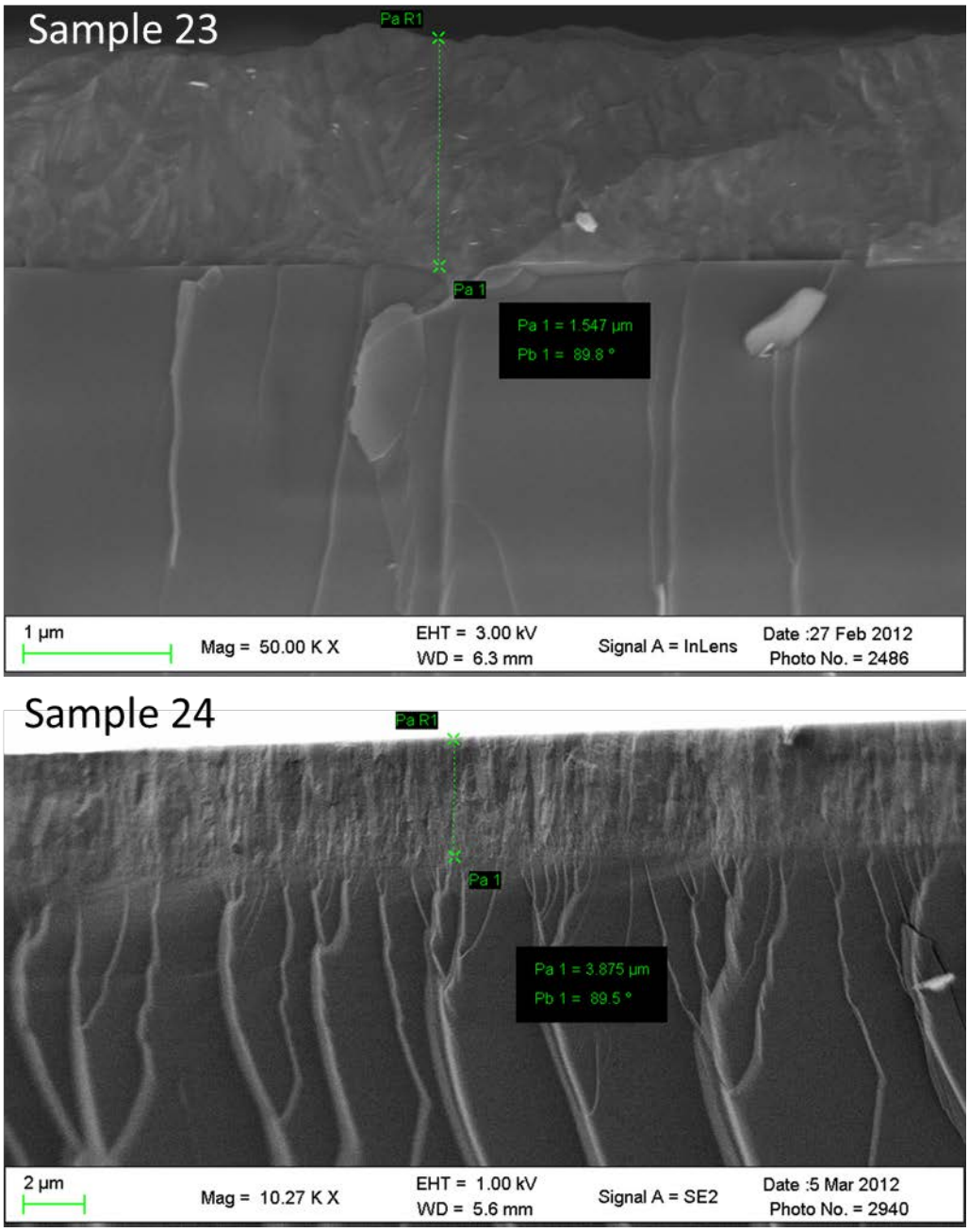

Figure 101. Cross sectional SEM micrographs of samples 23 and 24 at different magnifications

Figure 102. Photograph of sample 25 post deposition. Note the conical appearance to the film

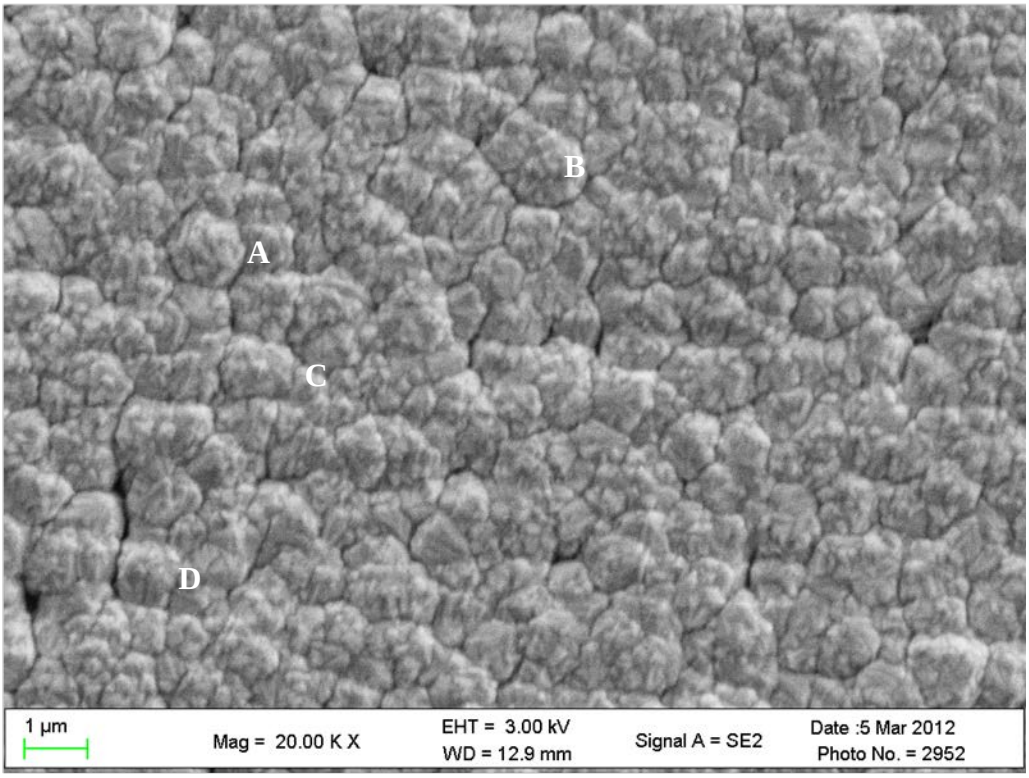

Figure 103. Surface SEM image of sample 25. Showing well-formed particle structures labeled A-D, suggesting Volmer-Weber growth mode.

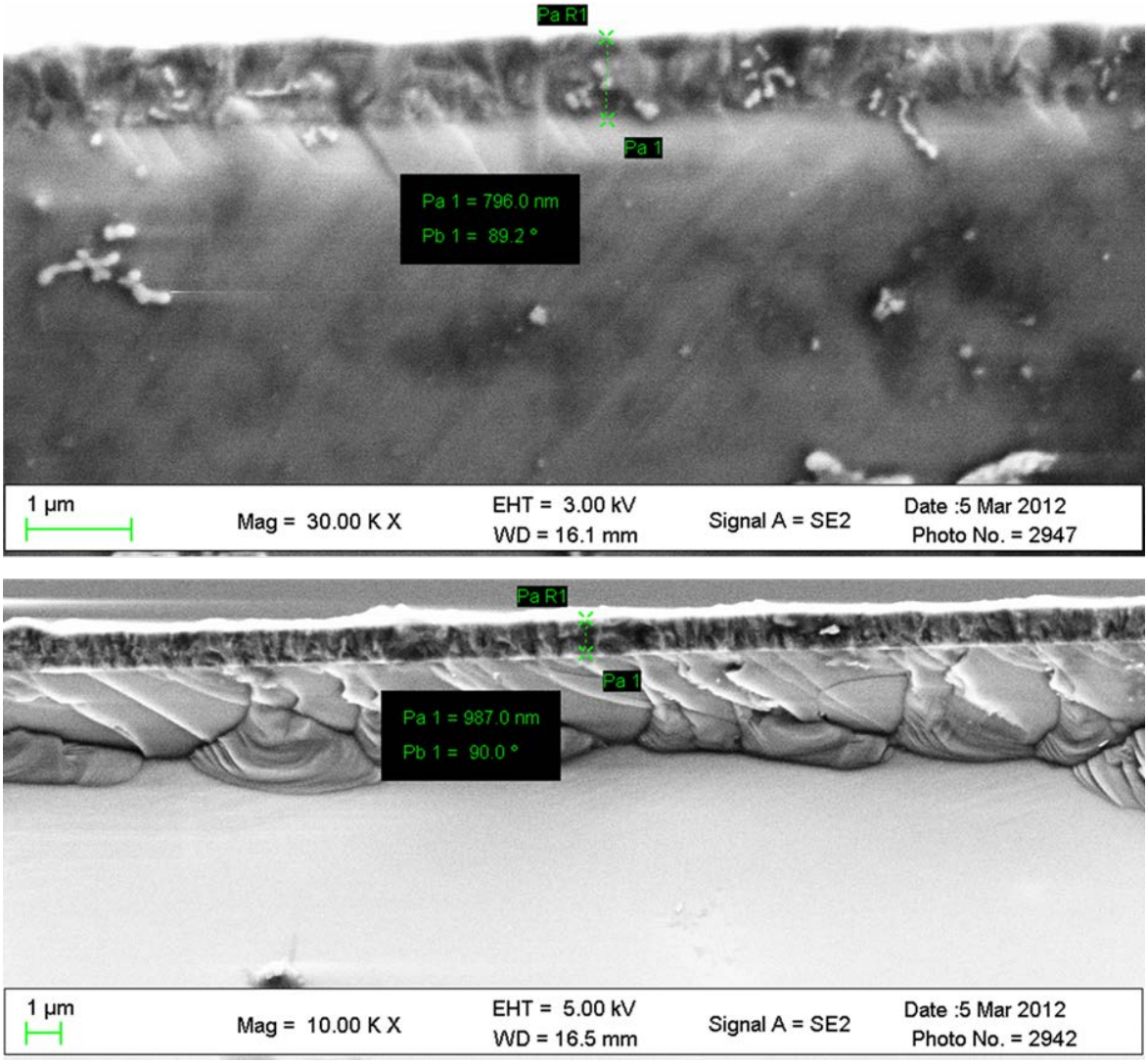

Figure 104. Cross sectional SEM images of sample 25

Figure 105. Photograph of sample 26 post deposition. Film shows even coverage with exception to the top left corner. A thickness gradient is apparent.

.

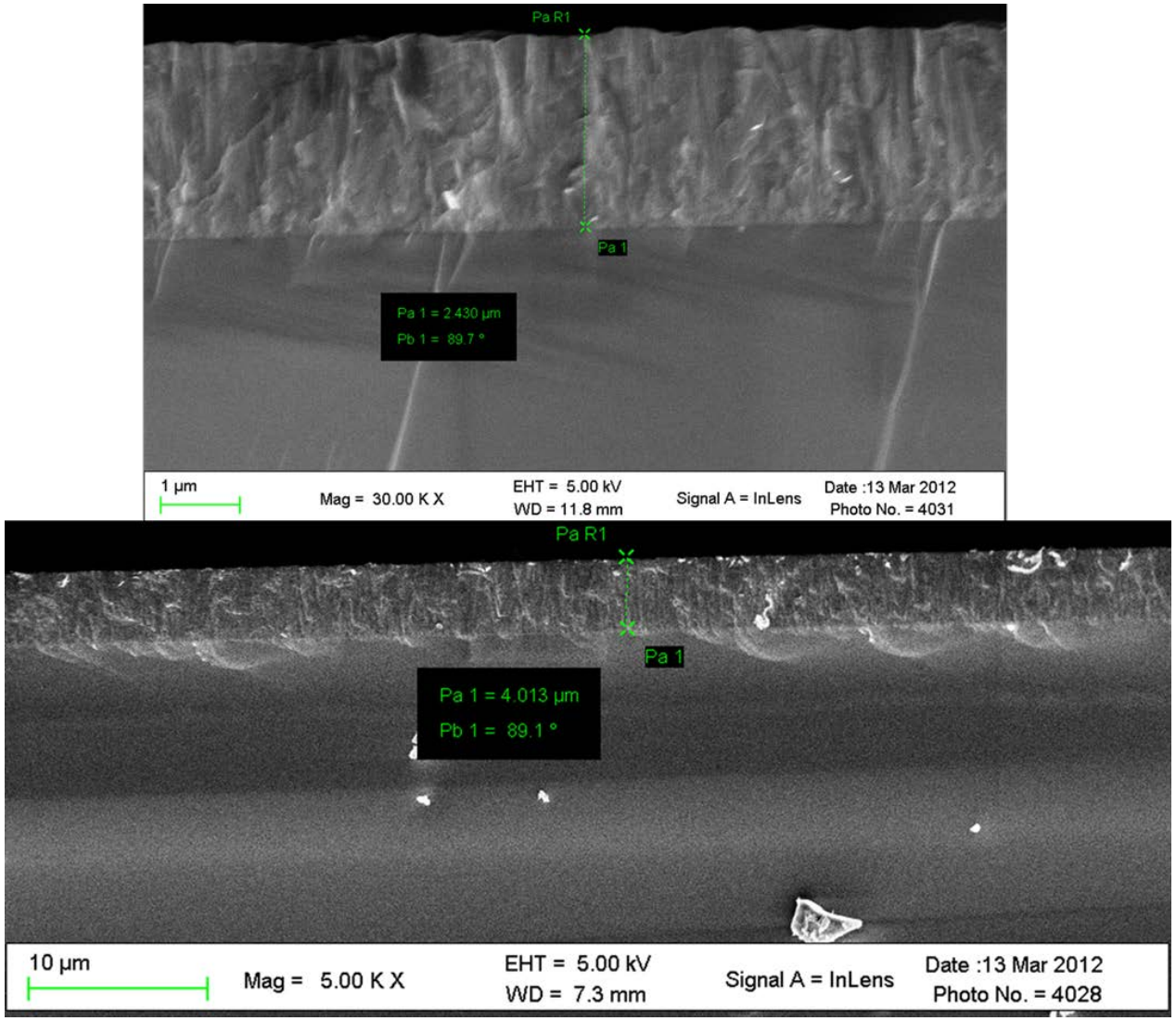

Figure 106. Cross sectional SEM Images of sample 26. Top image shows thin film thickness of 2.43 um. Bottom shows a thickness of 4.01 um

Figure 107. Photograph of Sample 27 post deposition

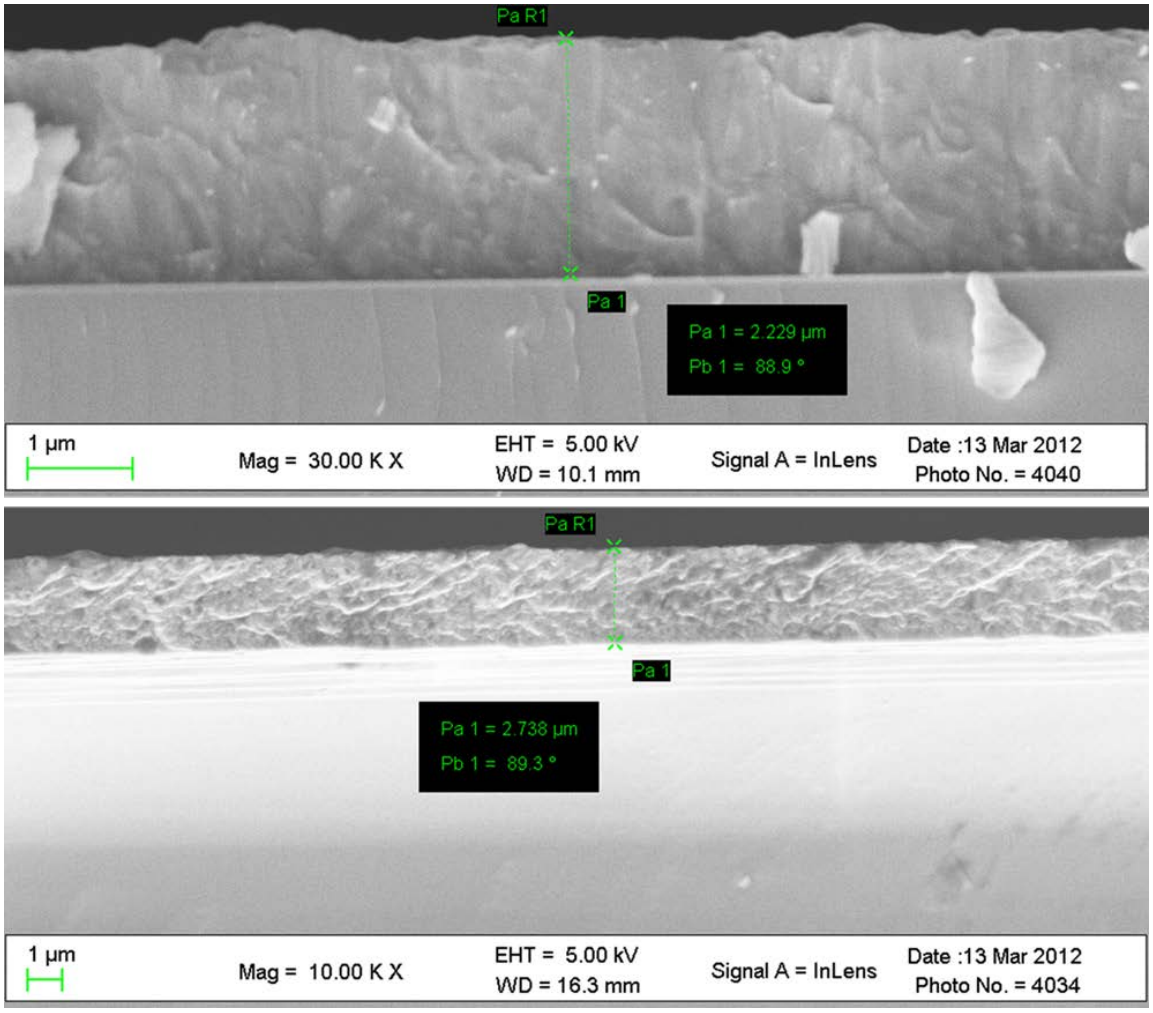

Figure 108. SEM micrographs of sample 27.

VITA

John Daniel Brasfield was born on March 14th 1979 in Kingsport, Tennessee; the second child of Robert and Judy Brasfield. After graduating from Kingsport Christian School in 1997 as Valedictorian, Daniel attended East Tennessee State University in Johnson City, Tennessee where he received a Bachelor of Science with a major of Chemistry in 2001. Upon completion of his degree to 2006 Daniel worked jobs in the nuclear industry focusing on health physics and radiation protection. In the spring 2006 he accepted a position at the Y-12 National Security Complex as a Research and Development Chemist. In the summer of 2008 Daniel entered graduate school at the University of Tennessee- Knoxville and received his Ph.D. in December of 2013.